A Proposal for a High Resolution Focal Plane Detector

Annemarie Keenan

Presented as a Thesis for the Degree of Master of Science

Department of Physics and Astronomy,

University of Glasgow,

February 1995.

ProQuest LLC.
789 East Eisenhower Parkway
P.O. Box 1346
Ann Arbor, MI 48106 – 1346

Abstract

This thesis is an investigation into the most effective way of constructing a high resolution focal plane detector for the Glasgow photon tagging spectrometer installed at Mainz. Chapter 1 summarises the objectives which must be met by such a detector and concludes which detectors should be further pursued. Chapter 1 also outlines and investigates the pertinent spectrometer specifications, with particular emphasis on magnet optics, so that decisions can be made about the required detector dimensions.

Chapter 2 is a feasibility study of a scintillator/ photomultiplier detector array and shows that such a detector array is impractical to implement.

Chapter 3 explains the basis of a silicon strip detector and then looks at the possibility of using a strip detector array. Various types of pre-amp are then outlined for the strip detector and for the charge sensitive pre-amp chosen, further amplification and filtering is investigated using NIM modules, to obtain the optimum timing pulse for a given level of noise. The timing resolution of the strip detector system is then determined for various pulse heights and the results are used to conclude what kind of strip detector would best fulfil the objectives outlined in Chapter 1.

Chapter 4 describes the construction and testing of small, onboard amplification and filter circuits, to replace the amplifier and filter NIM modules used in Chapter 3. The gain of the chosen onboard amplifier filter circuit is also calculated, but the equations deduced are left very general, so that the same formulae can be applied, if the values of the components in the filter circuit are altered. Some general conclusions are then drawn about a strip detector focal-plane detector system.

Declaration

The work presented in this thesis was carried out at Glasgow University between October 1992 and September 1994. I participated fully in the execution of all the work described. This thesis was composed by myself.

Annemarie Keenan

Acknowledgements

I extend special thanks to Dr. J.C. M^{c}George for his invaluable guidance and infinite patience, during the composition of this thesis and to Dr. P.D. Harty for his help and encouragement throughout this project. I am indebted to Dr. I Anthony and Mr. A. Sibbald for the numerous computing problems they have solved for me and to Mr. S. Lumsden, Mr. E. Coyle and all the other technical staff for the help they have given me with various aspects of the detector system construction. I wish to thank Dr. J.R.M. Annand for introducing me to the electronic hardware and overseeing the tests which I carried out. I am also grateful to Prof. R.O. Owens for providing me with the opportunity to undertake this project and Dr. S.J.Hall for his help.

To the above and all other members of the Glasgow University Experimental Nuclear Physics Group, I would like to say a big thank-you for providing both a pleasant working and social environment, especially to Dr. R.A. Crawford, whose kind hospitality saved me from cycling the 11 miles home in the "wee small hours" on a very regular basis (thanks for all your help with the computing as well, Rebecca!).

Finally, I owe a debt of gratitude to Dr. T. Davinson of Edinburgh University, for providing me with the strip detector and various other components which I tested and for all his help and advice.

Contents

List of Figures

List of Tables

Chapter 1

Specification For Focal-Plane System

1.1 Introduction

This thesis describes the design and testing of a high resolution focal-plane detector system for the Glasgow photon tagging spectrometer [3]. The spectrometer is installed at the MAMI-B electron accelerator [1, 2] in the Institut für Kernphysik, Universität Mainz, Germany. The need for such a detector results from the rapid improvement, seen over recent years, in facilities available for intermediate energy photonuclear physics and the consequent need for more sophisticated detectors, capable of probing the photonuclear reactions and the structure of nuclei.

In order to perform intermediate energy, photonuclear experiments, a beam of monochromatic photons in this range is desirable. With the advent of high duty cycle electron beams, a reasonably high photon intensity can be produced with a photon tagging system. The system at Mainz produces photons from the primary electron beam by the bremsstrahlung process in a thin foil radiator. The bremsstralung photons are mostly produced along a direction close to that of the primary electrons and can therefore be collimated to form a photon beam suitable for photoreaction studies. The energy of the degraded electrons, which have radiated a significant part of their energy, is determined by a magnetic spectrometer. FIGURE (1.1) shows the principle of determining the energy of tagged photons from the spectrometer.

If the reaction product, from the photonuclear target placed in the photon beam, is observed in time co-incidence with a signal induced by a degraded electron, in a detector placed in the focal-plane of the spectrometer, then the

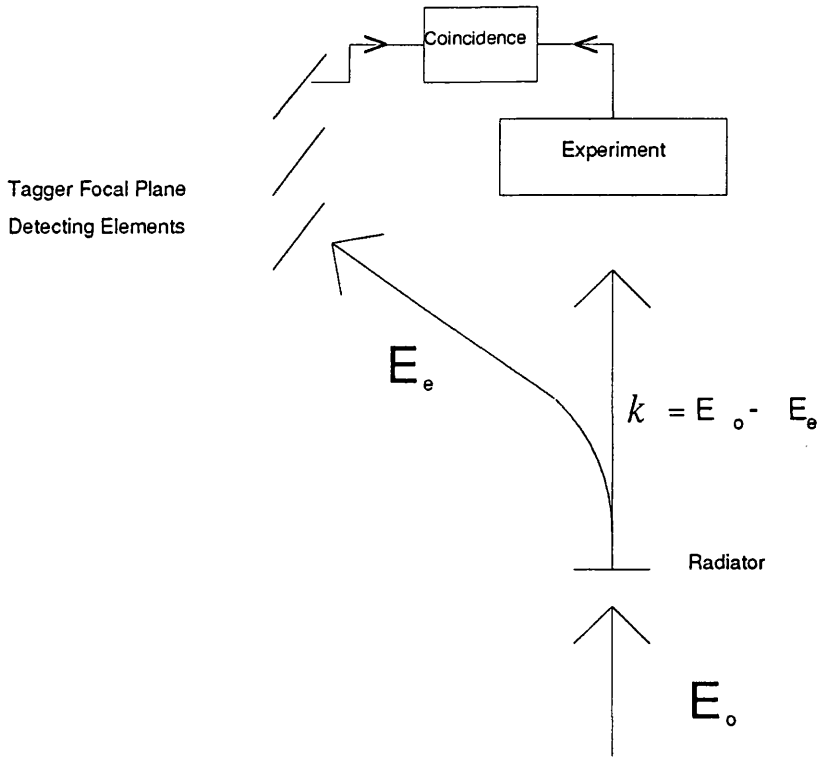

Figure 1.1: *Schematic Photon Tagging Set-up.*

photon energy can be deduced from the formula

$$k = E_o - E_e, \tag{1.1}$$

where E_o is the incident electron beam energy,

E_e is the degraded electron energy,

and k is the energy of the bremsstrahlung photon.

The energy resolution of the tagged photons is determined by both the energy spread of the electron beam and the energy resolution of the spectrometer. For the Mainz system, the energy spread of the main 855 MeV beam is approximately 60 keV. The photon tagging spectrometer is a quadrupole-dipole design (FIGURE 1.4) and has intrinsic resolution of approximately 100 keV over most of the focal-plane. The actual spectrometer resolution is however currently determined by the width of the 353 scintillator detectors placed in the focal-plane and equals $\sim$2 MeV. This present resolution was chosen, because it is good enough for most experiments, while keeping the cost of covering the whole 50-750 MeV useable range of the focal-plane reasonable. More specifically, the choice of 2 MeV resolution followed from the expected use of the tagger. The initial experiments did not demand a resolution capable of distinguishing final nuclear states which, even for the low lying states of light nuclei, is typically around 500 keV. Nuclear structure did however affect the choice of resolution. For the type of experiments that were envisaged, where nucleons are knocked out of the nucleus, the results depend on the shell from which the nucleons are removed. An overall resolution of $\sim$10 MeV is required to resolve these shells and it was this factor that led to the choice of a 2 MeV resolution for the spectrometer. This choice has proved to be good for experiments such as (γ,NN) and (γ,Nπ), for which the present focal-plane detector was mainly designed.

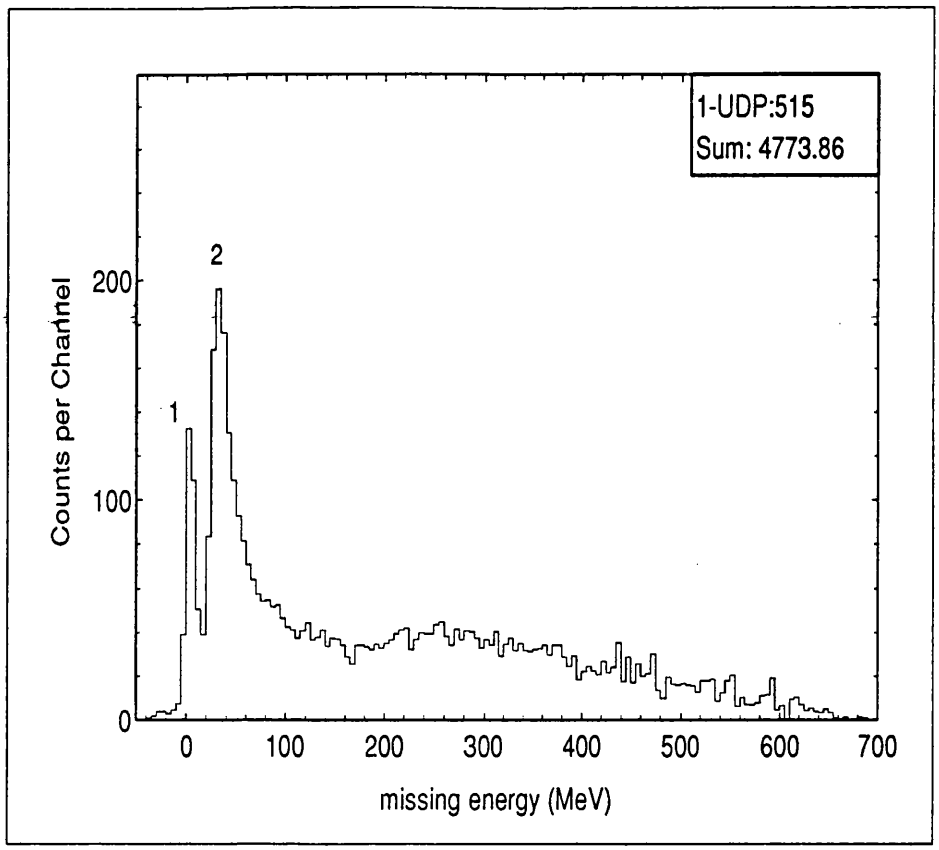

Figure 1.2: *Typical Energy Spectrum:* $^{6}Li(\gamma,pn)$

FIGURE (1.2) shows results from a typical experiment [4]. This is the missing energy spectrum of the ^{6}Li(γ,pn) reaction. The protons were detected in a plastic scintillator hodoscope (PIP) and the neutrons were detected in a time of flight array(TOF). Peak (1) at $\sim$4 MeV is caused by the photon knocking the loosely bound p-shell pn pair out of the Li nucleus. Peak (2) at $\sim$26 MeV is due to a photon breaking up the tightly bound He-like core of the Li nucleus. With over 20 MeV between these peaks, the present focal-plane detector resolution is adequate to distinguish these two features.

However other experiments, for which a focal-plane detector resolution of 2 MeV would be inadequate, had already been envisaged, while the tagger was being constructed. These include:

(1) Photopion production near threshold. For example, the photopion cross-

sections and angular distributions vary very rapidly with photon energy in the region from the π^0 threshold at 145 MeV to the π^+ threshold at 151 MeV. A resolution of ~250 keV, between a photon energy of 130 → 180 MeV would be needed to examine this.

(2) At η production threshold on the proton, at a photon energy of ~707 MeV, the (γ,η) cross section changes very rapidly. The measurement of this threshold can be used to improve on the presently best known value for the η mass, which is 547.45 ± 0.19 MeV. For a meaningful improvement, the photon energy resolution must be ≤ 0.1 MeV over a 50 MeV range around threshold.

(3) An experiment has been proposed to search for dibaryon resonances. These are bound states of 6 quarks, other than N-N and are predicted to exist with widths of less than 1 MeV and masses which can be excited by γ's of a few hundred MeV. Good resolution would be required in order to isolate the resonance from background. For a search, less than 1 MeV resolution would be needed over several 50 → 100 MeV wide regions, with photon energies ranging from 150 → 550 MeV.

With these experiments in mind, a small gap was left between the focal-plane and the present focal-plane detector array, to allow insertion of an auxiliary higher resolution detector at a later date.

The purpose of such a detector is however two-fold. As well as being capable of higher resolution, it is desirable for the detector array to be capable of accepting a larger overall rate of tagged photons. Photonuclear cross sections are small and therefore it is desirable to increase the tagged photon rate by increasing the electron beam current, to get a good statistics in the shortest possible time. However, an increased beam current reduces the real:random

coincidence ratio. Any chosen beam current is therefore a compromise between good statistics in a short time and a good real:random ratio. The real:random ratio can however be restored, if smaller detectors are used such that the count rate in a smaller detector channel, at a higher beam current, equals the count rate observed in one of the existing detectors, at the present beam current. This condition holds provided that each new detector is capable of the same timing resolution and count rate as the existing detectors. Higher resolution in the focal-plane detector array will therefore be investigated, with the hope that it may also provide a higher count-rate capability.

1.2 An Outline of Requirements for a New Focal-Plane Detector

(1) Resolution:

The required resolution is 0.1 $\rightarrow$ 0.4 MeV, in line with the proposed experiments discussed above. It would be difficult to achieve this over the whole of the focal-plane, due to the fact that the detector width required to produce a certain resolution becomes smaller with decreasing electron energy. This will be more fully explained in §1.3. However, it is useful to attain this resolution over a limited energy range, in the areas that would be of interest for particular experiments.

(2) Portability and Cost:

If a high resolution detector is, at any one time, only required over a limited range in the focal-plane, it is not necessary to replace the existing focal-plane detector with a high resolution alternative over the whole of the focal-plane.

Such an undertaking would also prove too costly. As well as the additional cost of the basic detector elements, the amount of electronics associated with an increased number of individual elements would rise proportionately. The present focal-plane detector array should therefore remain intact and high resolution remain a removable option. A mini focal-plane detector is therefore envisaged, which will cover about 50 $\rightarrow$ 100 MeV of the focal-plane at any one time, but which is flexible enough to be inserted at any position in the focal-plane.

(3) Photon Flux:

This gives the count-rate limitation in the focal-plane detector. The limitation of the present system is $\sim 1.5 \times 10^6$ Hz/MeV and was determined mainly from the gain stability of the photomultiplier tubes and the real:random ratio for the tagged photons produced. Other considerations, if higher rates were tolerable, would be pulse pile-up and dead time. Any new detector should at least be capable of an equally large photon flux.

(4) Timing:

Detectors used in coincidence with the tagger have a timing resolution of $\sim$1 ns. Therefore, to avoid a serious increase in the width of the prompt co-incidence peak for these experiments, which would degrade the real:random ratio, the focal-plane detector timing should be $\leq$ 1 ns. This condition may be relaxed, if the higher resolution detector is operated in co-incidence with the current focal-plane detector array, which has subnanosecond timing, so that the higher energy resolution detector is only required to determine the photon energy.

(5) Signal:Noise Ratio:

The accuracy with which the individual detecting elements evaluate the amount of energy actually deposited in them is secondary. However, it is of paramount importance that the signal:noise ratio is large. A good signal:noise ratio is required so that there is a clear distinction between signals and noise. Then, a discriminator level can be set to reject noise, but retain a high counting efficiency for electrons. A good signal:noise ratio is also required for good timing. Otherwise, noise can introduce significant jitter at the discriminator.

(6) Dimensions of The Individual Detector Elements and Associated Electronics:

WIDTH; The resolution of the focal-plane detecting elements is proportional to their width. Each element should therefore be no more than 2 mm wide. This gives resolution of $\sim$ 250 keV. The width of the associated electronics for each detector channel should be kept as close to the detector element width as possible, if the electronics are mounted in the same plane as the detector. It is undesirable to mount the electronics normal to the detector, because of the limited space available for housing a new detector in the focal-plane, as explained below.

The gap where an auxiliary detector and any required electronics can be inserted, lies between the spectrometer magnet and the focal-plane detector array. The defocusing of the electrons, after having passed through the focal-plane, prevents the positioning of the detector behind the existing detector array. This gap is limited to as little as 2.8 cm thick, for a height of 20 cm immediately above and below the bend plane. The positioning of any associated multichannel shaping electronics mounted within this volume (see FIGURE (1.3)), is therefore restricted. Outwith this volume, there is little limitation on

the gap thickness.

THICKNESS; The detector thickness should be large enough to give a good signal:noise ratio, but still small enough to limit the effect of the angular divergence introduced by scattering, which increases with detector thickness. There are two reasons why scattering is undesirable. One is that the dynamic range of the detector pulse height spectrum increases as the scattering increases. Thus, any pulse height related walk in the discriminator would increase accordingly. Secondly, scatter can limit the resolution, by introducing an angular divergence into the electron trajectory, that may cause the electron to be deflected into the detector adjacent to the one it strikes first. Whether the result was a pulse being observed in both detectors, or a signal recorded in the adjacent detector, this can result in a loss of resolution.

HEIGHT; The detector height required to record electrons is at most required to be 60 mm, so that it just overlaps the 50 mm pole gap of the spectrometer. However, in §1.3, the focussing capabilities of the spectrometer magnet will be examined to ascertain the height required to intercept the bremsstrahlung electrons.

There is no practical geometrical limit on the height to which the detector and the associated shaping electronics may extend. However, the length of any board carrying any necessary electronics may have to be minimised to reduce susceptibility to pick-up and reduce the stray capacitance and inductance inherent in all conducting tracks on these boards.

(7) Intrinsic Efficiency:

The total fraction of bremsstralung electrons recorded should ideally be

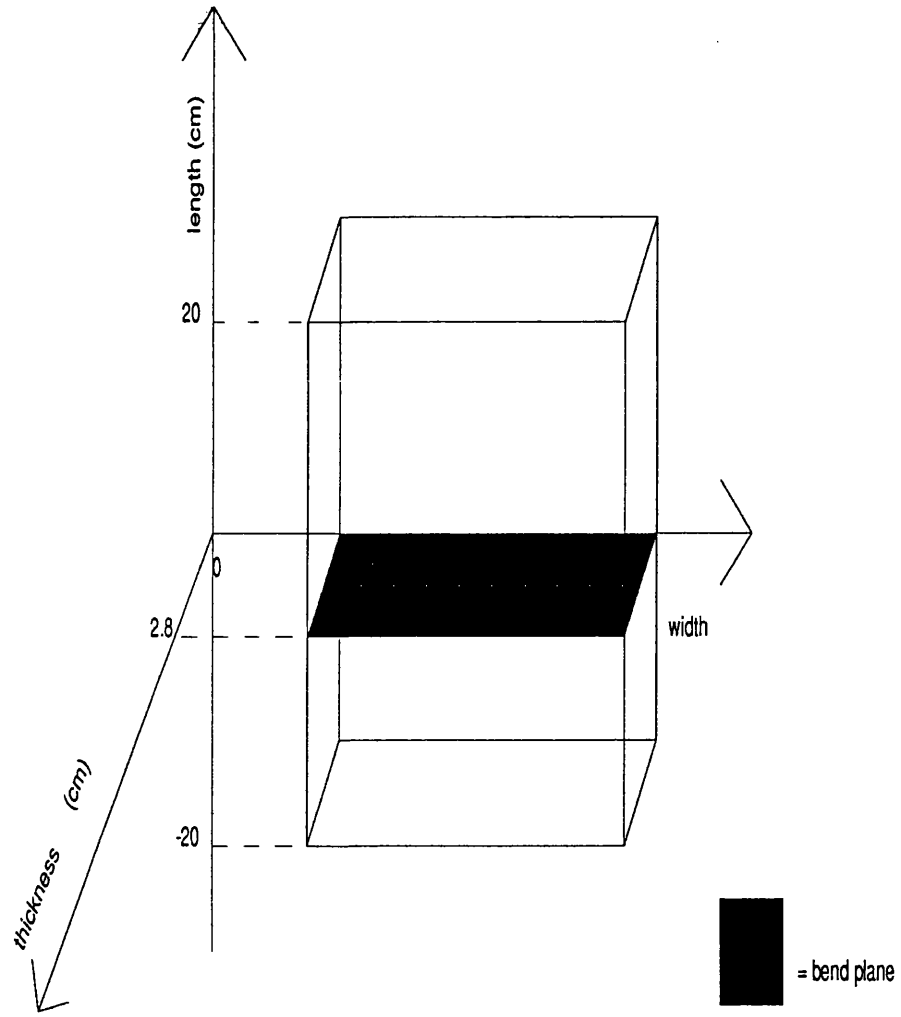

Figure 1.3: *Limitations On The Volume of Space Available To House The Detector. (For clarity, the dimensions have not been drawn to scale.)*

equal to 100%. This ratio is known as the counting efficiency and for the present tagger and focal-plane detector system, is $\geq$ 97%. The major factor in the 3% reduction, are those electrons which do not enter the spectrometer magnet pole gap. In the absence of a quadrupole, as will be shown in GRAPH (1.9B), the axial image height, formed by 97% of the electrons, reaches a maximum of 56 mm, which is virtually equal to the pole-gap. It is from here therefore, that the value for counting efficiency is derived. However, it should be observed that this figure of 97% does not automatically hold for another detector array. Other common causes of reduction in counting efficiency include "dead time", the "dead" area between the individual detectors, a discriminator setting which eats into the authentic output signals and finally, the entrance angle of the incident electrons, which may result in the electrons traversing less than the full detector thickness and consequently, producing a smaller signal, whose amplitude fails to fire the discriminator.

(8) Lifetime:

With a typical usage of 2500 hours/year, the detector should have a practicably long lifetime, for the desired beam current. The present array has an expected lifetime of 2 $\rightarrow$ 5 years, set by the ageing of the photomultiplier tubes. When gain drops due to ageing, the voltage must be increased to compensate for this. The upper limit is reached when the voltage required for the desired gain nears breakdown.

The rest of this chapter discusses the present tagging system, especially the tagging spectrometer and how its properties determine the specification of the new focal-plane detector, in order to meet the above requirements. Conclusions about detector types to be tried will be given at the end of the chapter.

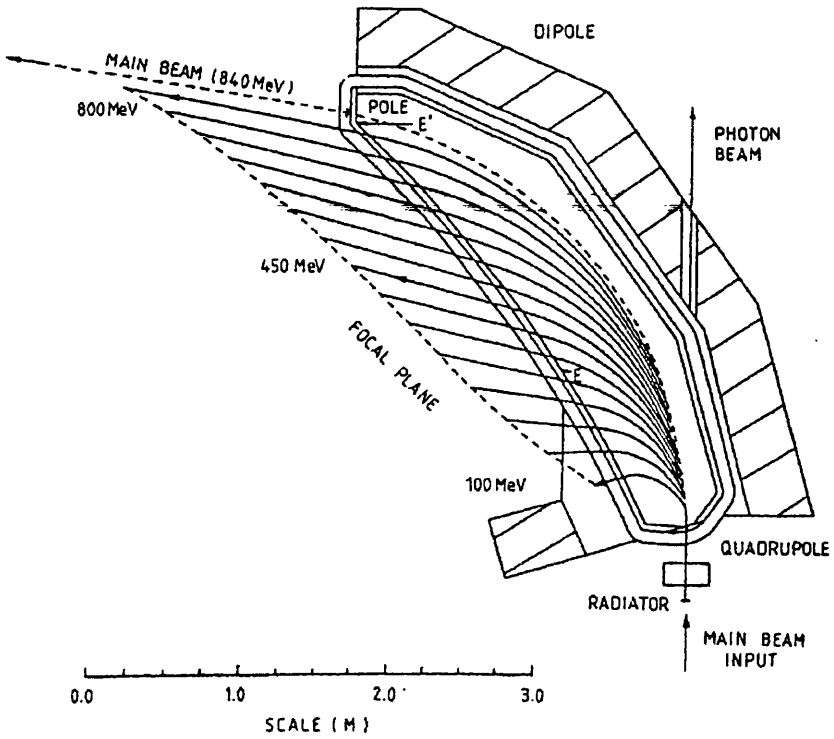

Figure 1.4: *The Glasgow Photon Tagging Spectrometer at Mainz.*

1.3 The Current Spectrometer; Relevant Specifications

A diagram illustrating the Glasgow tagging spectrometer is shown in FIGURE (1.4) and the specifications are summarised in TABLE (1.1).

The spectrometer takes the main beam, after passing through the radiator and bends it 80^0 to a dump. The electrons, which radiate bremsstrahlung photons, are however bent round into the focal plane by the spectrometer magnet and their horizontal displacement along the focal-plane is proportional to their

General :	
momentum acceptance	8:1
solid angle acceptance	~8 msr
angular acceptance	±50 mrad
dispersion	~ 1 cm/%
first order optics in radial plane	point to point
momentum range	50-800 MeV/c
object distance	0.1 m
quadrupole/dipole separation	0.25 m
Quadrupole :	
Max. pole tip field	-0.66 T
Aperture diameter	5.3 cm
Length	0.15 m
Dipole :	
Magnetic field	1.00 Tesla
Entrance and exit face radii	straight - 8.0 m
Gap height	5 cm
Weight	~ 65 tons
Bend radius (main beam)	2.8 m
Bend angle (main beam)	80°
Entrance and exit angle (main beam)	16.7° - 58.8°

Table 1.1: *840 MeV Photon Tagging Spectrometer Parameters*

energy. Thus, the focal-plane detector array can be calibrated to determine the degraded electron energy, from the position of the detector element the electron strikes.

Magnet Configuration

The dipole is responsible for resolving the electrons' energies, dispersing them in the horizontal bend plane and focussing them vertically into a reasonably, flat plane, so determining the focal-plane shape which best accommodates a detector array. The field strength is set at 1.00T. For the maximum MAMIB 855MeV incident electron beam energy, this offers a good compromise between minimising the bend radius, to obtain a short radiator to nuclear target distance (and therefore a small beam spot) and retaining good field homogeneity, which is distorted at high fields. Otherwise, due to these field inhomogeneities, the fo-

cussing capabilities of the magnet would be difficult to predict. The quadrupole focuses vertically, i.e. perpendicular to the bend plane and therefore gives better acceptance of electrons which would otherwise hit the pole faces. Hence, it affects the vertical image size and the detector size needed. The quadrupole also affects the resolution. If it is vertically focussed, then the electrons diverge more than their natural divergence in the horizontal plane. When they reach the dipole field, the extra divergence they have incurred means that they are focussed more sharply by the dipole field, so resolution improves. The quadrupole field strength is variable and ranges from 0 to -24.9 $T.m^{-1}$.

Energy Acceptance: The spectrometer has a wide acceptance of 50 MeV $\rightarrow$ 800 MeV, for electrons bent into the focal-plane.

Magnet Focussing

For simplicity, the spectrometer magnet focussing capabilities were calculated with the first order code TAGQD [5]. Although more accurate second order calculations have previously been carried out for the magnet with the RAYTRACE code, [6, 3], these were only performed at quadrupole strengths of 0 $T.m^{-1}$ and -15 $T.m^{-1}$. The results of the TAGQD calculations at 0 $T.m^{-1}$ and -15 $T.m^{-1}$, however, did not differ significantly from those obtained previously with RAYTRACE. The previous RAYTRACE calculations were done to show the change in the focussing properties of the magnet, when the quadrupole field strength was set at 0 $T.m^{-1}$ and when the quadrupole strength was set to minimise the vertical image size for electrons with an energy of 100 MeV. In the present investigation, however, it is not the focussing at one particular energy that is of consequence, but rather the focussing over a wide range of energies. In this way the minimum detector size, required to cover the vertical

image height of the object, over electron energies ranging from 100 MeV to 800 MeV in the focal-plane, can be evaluated with TAGQD, as well as the effect a particular quadrupole field gradient has on the electron resolution and associated dispersion. The first 100 MeV was omitted, because vertical focussing deteriorates quickly between 100 and 0 MeV. This effect will be demonstrated in FIGURES (1.9) and (1.10). As none of the proposed experiments seek to cover photons above 750 MeV, the required detector height need only be examined for electrons between 100 and 800 MeV.

TAGQD Results

Bend-plane (i.e.horizontal): For monoenergetic electrons, a point object produces a point image. FIGURE (1.5) shows electron energy resolution as a function of electron energy. The solid line shows electron resolution, when there is a zero quadrupole field gradient, while the dashed line shows electron resolution, when the quadrupole field gradient is set at its maximum value of -24.9 Tm^{-1}. (By convention, a negative sign represents an axially focussing quadrupole field.) In both cases, electron resolution in the focal-plane is seen to deteriorate as the degraded electron energy increases. When the quadrupole is off, the resolution reaches a maximum of $\sim$0.15 MeV , while when the quadrupole is on, resolution is observed to rise to only $\sim$0.12 MeV. Calculation at intermediate quadrupole settings showed that the energy resolution improved steadily as quadrupole strength was increased.

To relate the resolution quantatively to detector width, FIGURE (1.6), shows the dispersion of the electron image in the focal-plane. The solid line represents the dispersion in the absence of the quadrupole field and the dashed line shows the dispersion with a quadrupole field of -24.9 Tm^{-1}. The addi-

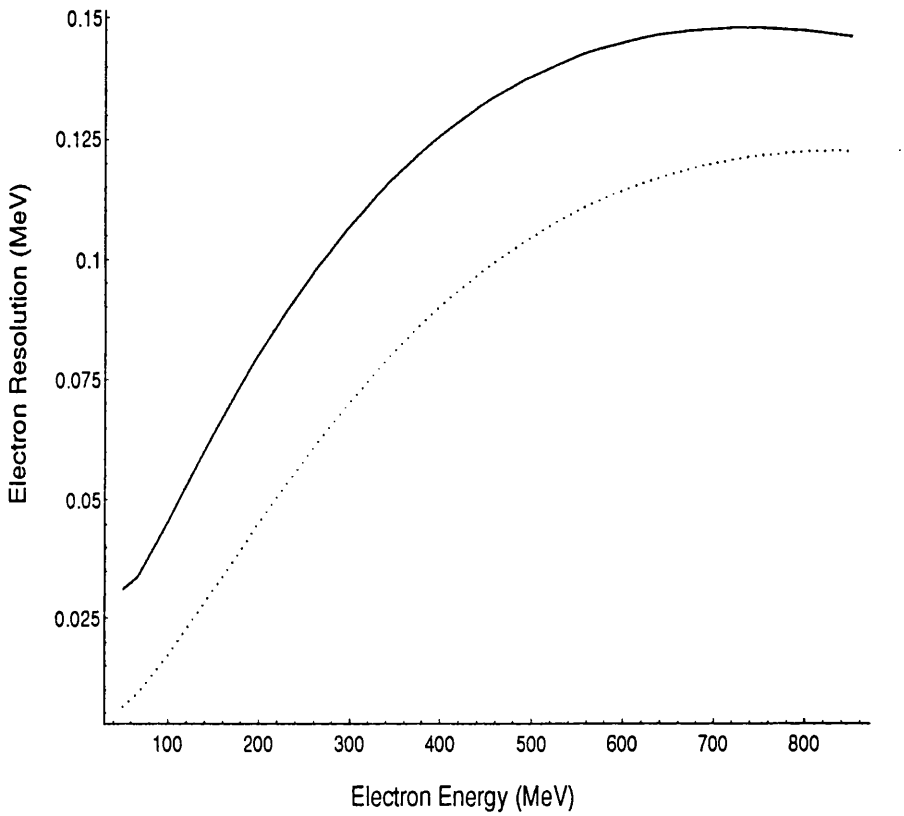

Figure 1.5: *Electron Resolution vs Electron Energy; Variation with Quadrupole Strength.*

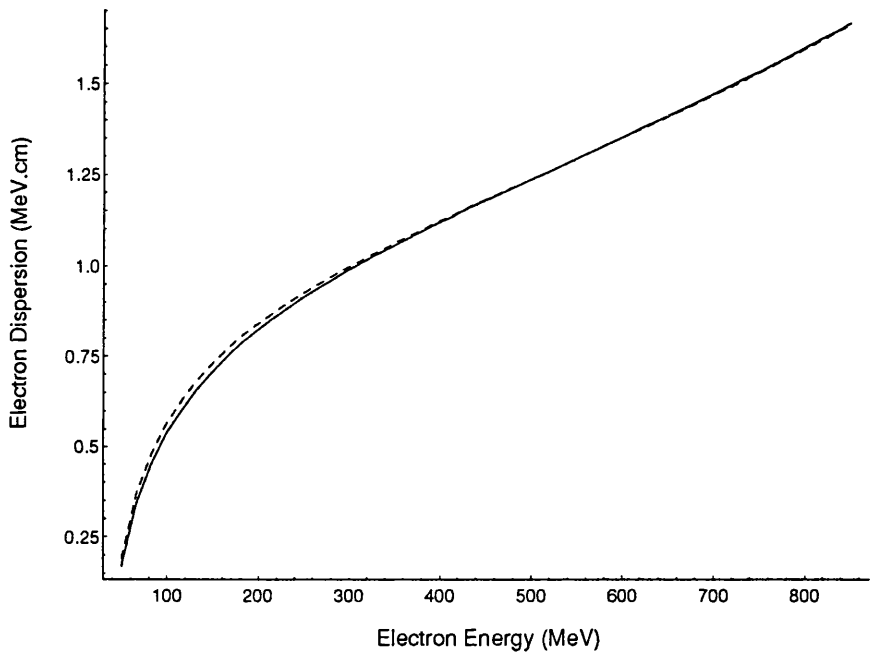

Figure 1.6: *Electron Dispersion vs Electron Energy; Variation with Quadrupole Strength.*

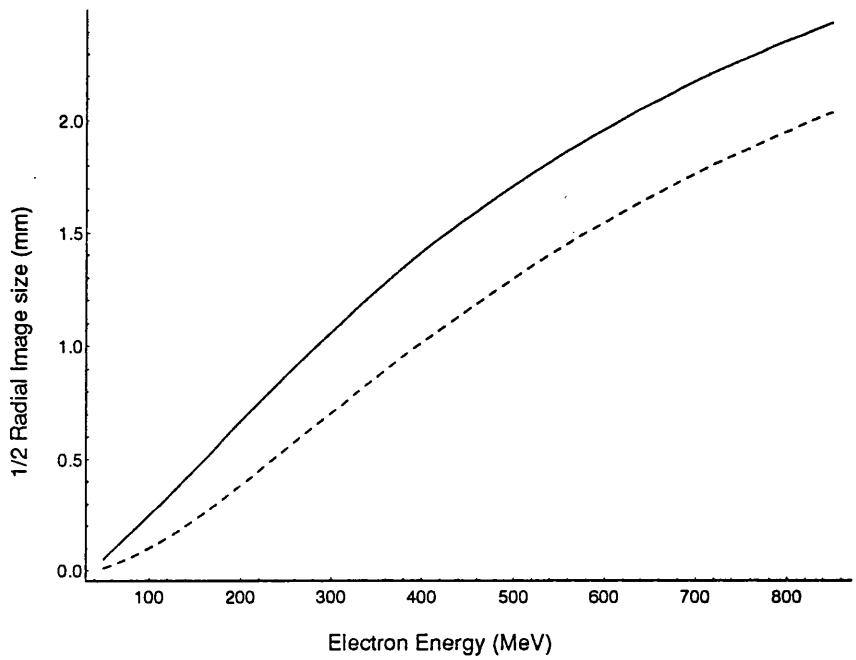

Figure 1.7: *Radial Image Size vs Electron Energy; Variation with Quadrupole Strength.*

tion of a quadrupole is seen to make very little difference to the dispersion. To obtain the intrinsic magnet resolution in terms of the distance along the focal-plane, the electron resolution is multiplied by the dispersion. Thus FIGURE(1.7), illustrates the detector width in millimetres, which would correspond to the intrinsic resolution of the magnet. The solid line shows that without a quadrupole, the detector width required to exploit the intrinsic focussing capabilities of the magnet is 0.25 mm at 100 MeV and increases to 2.4 mm at 850 MeV, while the dashed line indicates that with the quadrupole field strength = -24.9 $T.m^{-1}$, a detector 0.1 mm wide is desirable at 100 MeV. This rises

to 2 mm at 850 MeV. Ideally, a moveable detector should have elements with a width no greater than that required for the intrinsic magnet resolution to be realised at all energies within the 100 $\rightarrow$ 850 MeV range, however, there is no advantage in choosing detectors with a width $\leq$ 0.4 mm, since the photon resolution would then be determined by the 60 keV resolution of the beam. A detector width of 0.4 mm would be very difficult to construct, owing to the high density of electronic circuitry which would be required, in the limited confines of the focal-plane. Although it may be argued that the electronics could be placed at a more remote position, where space is not limited, this would result in attenuation of the detector signal, as well as susceptibility to pick-up in the signal cable. Other problems may include cross-talk and stray capacitance and inductance. However, from the outline of proposed experiments in §1.1, the resolution needed is between 100 and 400 keV, which would be met by a 2 mm detector. FIGURE (1.8) illustrates this point more fully by showing the resolution for a 2 mm detector. This resolution was calculated by dividing detector width by the dispersion calculated with the TAGQD programme.

The solid line shows the resolution obtained with the quadrupole field gradient set at zero and demonstrates that the resolution obtained with a 2 mm detector is about 380 keV at 100 MeV. This resolution improves as the degraded electron energy increases, until at 620 MeV, the horizontal image size, which determines the intrinsic resolution of the magnet, equals the detector width. Above this energy, the resolution is determined by the magnet and not by the detector width and as seen in FIGURE(1.5), equals about 145 kev. The dashed line illustrates the resolution obtained with the quadrupole field set at the maximum value of -24.9 $T.m^{-1}$. Due to the enhanced bend plane focussing, observed with a non-zero quadrupole field gradient, producing a horizontal image in the

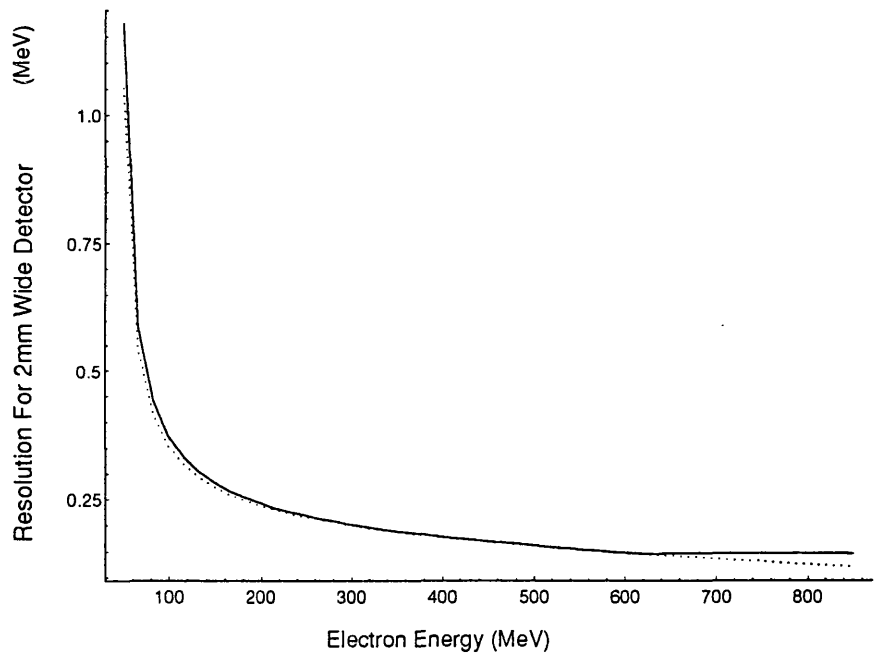

Figure 1.8: *Electron Resolution for a 2 mm Wide Detector vs Electron Energy; Variation with Quadrupole Strength.*

focal-plane, which is always smaller than 2 mm, resolution is determined solely by detector width, over the whole of the focal-plane. This varies from 360 keV, for 100 MeV electrons, to about 125 kev at 800 MeV.

~~Provided that the quadrupole field was set at maximum, there would be a~~ meaningful improvement in resolution, if a 1 mm wide detector was substituted for a 2 mm one at electron energies below 300 MeV. Here dispersion changes very quickly with electron energy and so, the detector width required to exploit the intrinsic magnet focussing quickly decreases. Therefore for the particular case of determining the η mass, which, as stated in §1.2, requires resolution of about 100 keV, in the 100 MeV electron region, a detector of about 1 mm would be required. Above 300 MeV, where the resolution obtained with a 2 mm detector is less than 200 keV, less than a factor of two improvement could be achieved with a detector of 1 mm width.

Non-bend-plane (i.e. vertical): For monoenergetic electrons, a point object produces a parallel image, due to the natural divergence of the degraded electrons exiting the radiator. The maximum, tolerable image height is 50 mm, corresponding to the pole-gap, where the vertical image height is, by definition, an acceptance set on the angle between the incident and degraded electron at the radiator, such that a given percentage of degraded electrons form an image of this height. Currently, in operating the spectrometer, 97% is stipulated. In this investigation however, both the present setting and a smaller acceptance of 85%, will be employed in the calculation of the variation of vertical image height with electron energy, for several quadrupole strengths, again using the "TAGQD" program. Thus, if minimising detector dimensions is deemed beneficial to performance and the acceptance is reduced to 85%, then the advantage

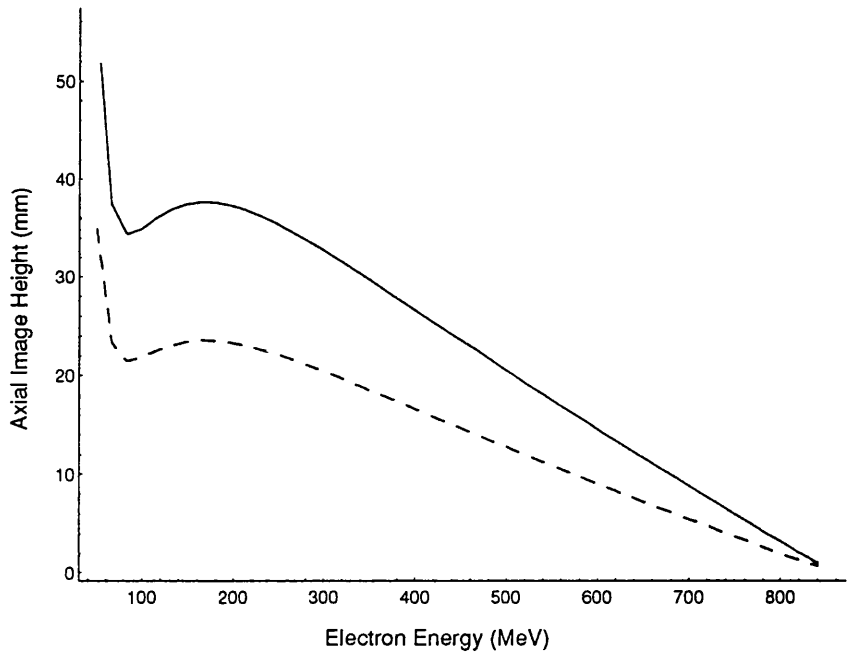

Figure 1.9: *Vertical Image Height vs Electron Energy; No Quadrupole.*

gained from the subsequent reduction in the detector height required to accommodate the image, can be weighed against the reduced counting efficiency. In FIGURE (1.9), the dashed line shows the variation of the vertical image height formed by 85% of electrons, with electron energy, in the absence of any quadrupole field. In the 100→ 850 MeV range, the maximum image height is 24mm. With the acceptance raised to 97% (solid line), but still in the absence of a quadrupole, the vertical image size is seen to rise to 38 mm.

Increasing the strength of the quadrupole to its maximum value of -24.9 Tm^{-1}, the dashed line in FIGURE(1.10) illustrates that the image height, formed by 85% of electrons between 100→ 850 MeV, is reduced to a 12 mm

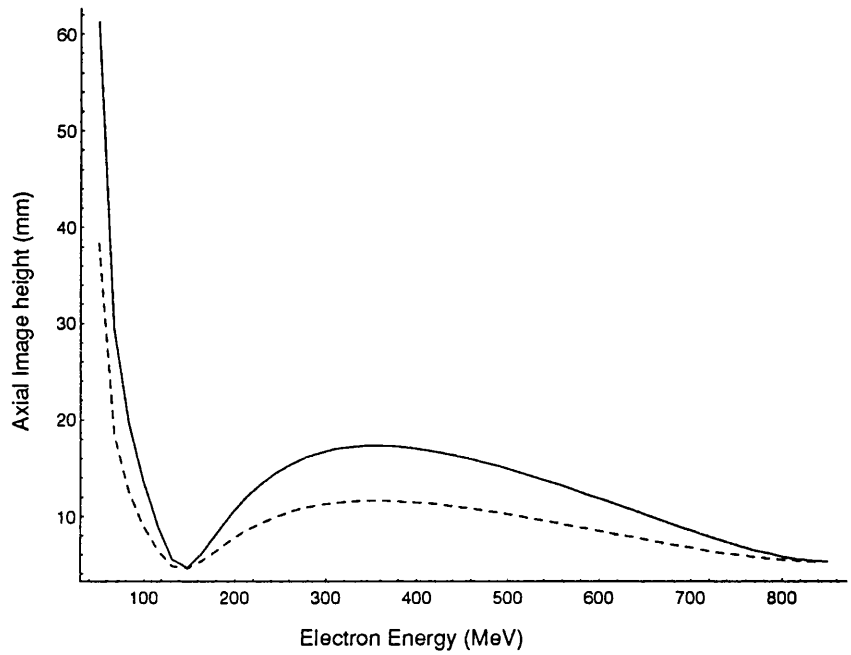

Figure 1.10: *Vertical Image Height vs Electron Energy; Quadrupole At -24.9* Tm^{-1}.

maximum, while that for 97% (solid line), has a maximum image height of 17 mm. Intermediate quadrupole settings were also investigated and, as expected, demonstrated a decreasing vertical image height with increasing quadrupole strength.

1.4 Detectors to be Considered.

There are several detector systems which may be considered as suitable for a focal-plane detector array. These include:

(1) Channel Electron Multiplier Array,

(2) Semiconductor Strip Detector Array,

(3) Multiwire Proportional Counter,

(4) Scintillator/Photomultiplier Array.

However, not all of these can fulfil the full list of requirements specified in §1.2. The channel electron multiplier was rejected, because it is expensive. Also, such devices cannot handle count rates much larger than ~1 kHz, owing to their high resistance (~3 GΩ) [7]. Compared to the current rate of 10^9 Hz, over the whole of the focal-plane, this would clearly represent an unacceptable reduction in the photon flux.

A multiwire proportional counter array was rejected, because the timing resolution is limited to 5 → 10 ns, which would represent a large compromise on the desired timing resolution of 1 ns [7]. This problem could be alleviated by operating it in co-incidence with the present focal-plane detector array, but this is not the only problem; radiation damage would cause chamber deterioration within ~2 weeks of operation at the current rate. This is due to the accumulation of impurities on the surface of the detector wires.

A scintillator/photomultiplier configuration has proved highly satisfactory in the present focal-plane detector array, but it has not yet been determined, whether such a detector can operate so effectively using a scintillator with a 2 mm width, as required for the desired 100 → 400 keV resolution.

A silicon microstrip detector could easily give the required energy resolution, but good timing is much more difficult to attain in these detectors. There does of course remain the possibility of operating in co-incidence with the present focal-plane, but all possible ways to improve the silicon strip detector timing

will first be investigated.

Options (2) and (4) will therefore both be examined and the associated signal-processing electronics will then be designed for the silicon microstrip detector, which will be shown to best fulfil all the requirements.

Chapter 2

A Scintillation Detector

2.1 Feasibility of Employing a Scintillation Fibre

As stated in §1.2, the desired focal-plane detector resolution of 100 → 400 keV requires a detector width of 2 mm. The thickness of the scintillators making up the present focal-plane detector is 2 mm. This thickness was chosen as a compromise between obtaining a good signal:noise ratio, which increases with detector thickness, and reducing background and the angular divergence of the electrons through the material, which both increase with detector thickness. For a 2mm piece of scintillator, the angular divergence, which is caused by scattering, [7], equals $\sim 1^o$. It is therefore undesirable to alter the scintillator thickness for the new detector. The height of the present focal-plane scintillators is 60 mm. This guarantees total coverage of the pole gap, so that the counting efficiency of the focal-plane detectors is essentially independent of the quadrupole field gradient. Although height could be reduced by a factor of four, if the quadrupole were operational, as shown in §1.3, there is no advantage in this, unless the attenuation length for light passing along the fibre was very short. From the scintillator specifications that will be outlined below, this is not the case. Thus, the required scintillator dimensions are (2 mm x 2 mm x 60 mm). The ratio of the 4 mm ^{2} area to the 60 mm length means that there is a high probability of the photons reaching the outer surface of the scintillator, while travelling down it. This probability would not be significantly reduced, unless the scintillator height was comparable to the thickness and/or width.

FIGURE (2.1) illustrates this point. Specifically, for θ and ϕ shown, the number of reflections, n, undergone by photons induced by an electron striking

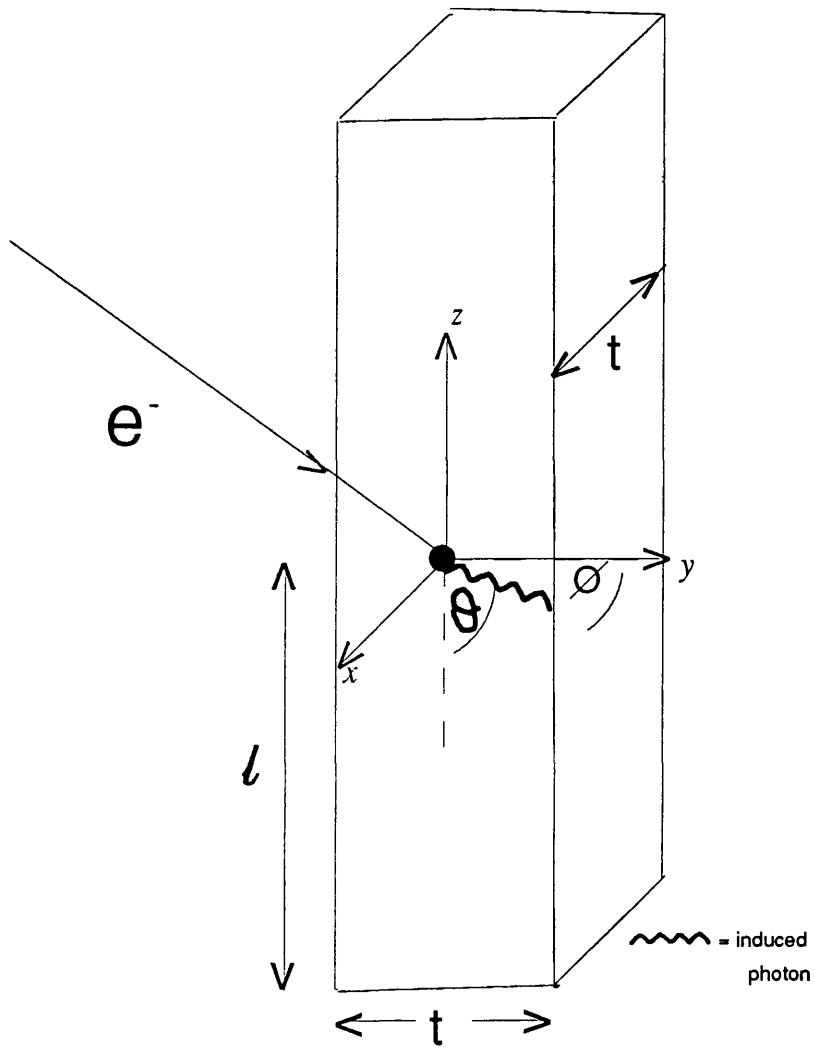

Figure 2.1: *Sample Photon Induced in the Fibre*

the scintillator at some distance, l, from where the light is collected, is given by

$$n = \begin{cases} \frac{l tan\theta cos\phi}{t} & : l tan\theta \leq \frac{t}{sin\phi} \\ \frac{l tan\theta sin\phi}{t} & : l tan\theta \leq \frac{t}{cos\phi} \\ \frac{l tan\theta}{t}(cos\phi + sin\phi) & : otherwise. \end{cases} \tag{2.1}$$

where θ is the angle between the photon and the z-axis and ϕ is the azimuthal angle (FIGURE (2.1)). Here, it has been assumed that l is large enough to assume that the photons are reflected at least once before reaching the photo-cathode, and that all photons collected are directed towards where the light is collected,

Although the critical angle of $\sim 48^{o}$, given by the ratio of the refractive indices at the scintillator/air interface, puts an upper limit on the θ which must be considered, it it can easily be shown from these equations that a large percentage of photons, induced by an electron incident 30 mm from where the light is collected, will undergo at least 10 reflections before collection. Unless very highly polished scintillator is used, a large proportion of photons produced in the scintillator would be lost at the surface, due to surface defects. Since scintillators of this size are often difficult to work with, a scintillator fibre will be used instead of conventional scintillator. The advantage of a fibre is that the signal suffers very little attenuation due to surface defects. This is because of the cladding moulded around the scintillator core. A normal piece of scintillator does not have this protection. The fibre B.C.F.12, from BICRON, was chosen due to its high light output response of 58% anthracene. This compares with 67% anthracene for the "pilot U " scintillator presently incorporated in the focal plane. However all fibres have a low 'trapping efficiency'. This means that the limiting incident angle of the induced photons on the fibre surface, for

which total internal reflection can occur, is small. For a B.C.F.12 square fibre, [8], the trapping efficiency is 3.4%, corresponding to a critical angle of 21° to the fibre surface. The critical angle here depends on the ratio of the refractive indices of the scintillator core to the cladding. This figure for trapping efficiency is a factor of ~12 smaller than that of a scintillator/air interface. The signal attenuation due to surface defects in conventional scintillator must be weighed against a much lower trapping efficiency, but the use of a fibre was considered to be worth investigating.

A second advantage of a scintillator fibre is that it is not as rigid as conventional scintillator and can be bent to some degree. This means more flexibility when considering how to mount it to a photomultiplier.

It is proposed that the fibres be coupled directly to multianode photomultiplier tubes (MAPMT's). A 2 x 2 mm^2 individual element pitch in MAPMT's is readily available. Therefore, the fibres could be coupled directly to elements that are small enough to be housed in the focal-plane, making the detector array compact and easy to manoeuvre (see FIGURE (2.2)). Larger photomultiplier tubes could be used, providing that the fibres were made long enough to enable these phototmultipliers to be housed out of the confines of the focal-plane gap. Longer fibres would also be required to limit any stress incurred while bending them to fit into such a large array of photomultipliers, as in FIGURE (2.3). This configuration would, however, be extremely delicate and difficult to manoeuvre up and down the focal-plane.

For a fibre/photomultiplier configuration, the number of photons reaching the photomultiplier per electron, can be estimated as follows:

All electrons with energies above about 900 keV can be considered minimum-

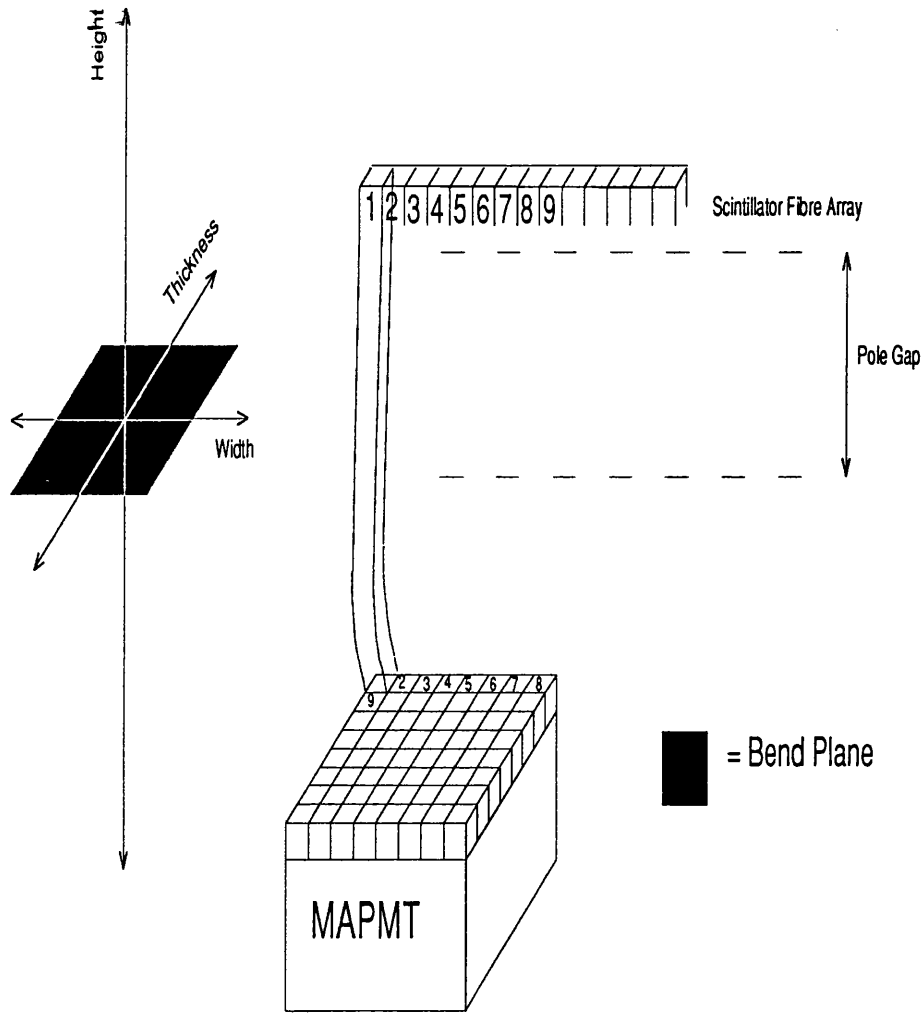

Figure 2.2: *Proposed Design for a Fibre/MAPMT Detector Array*

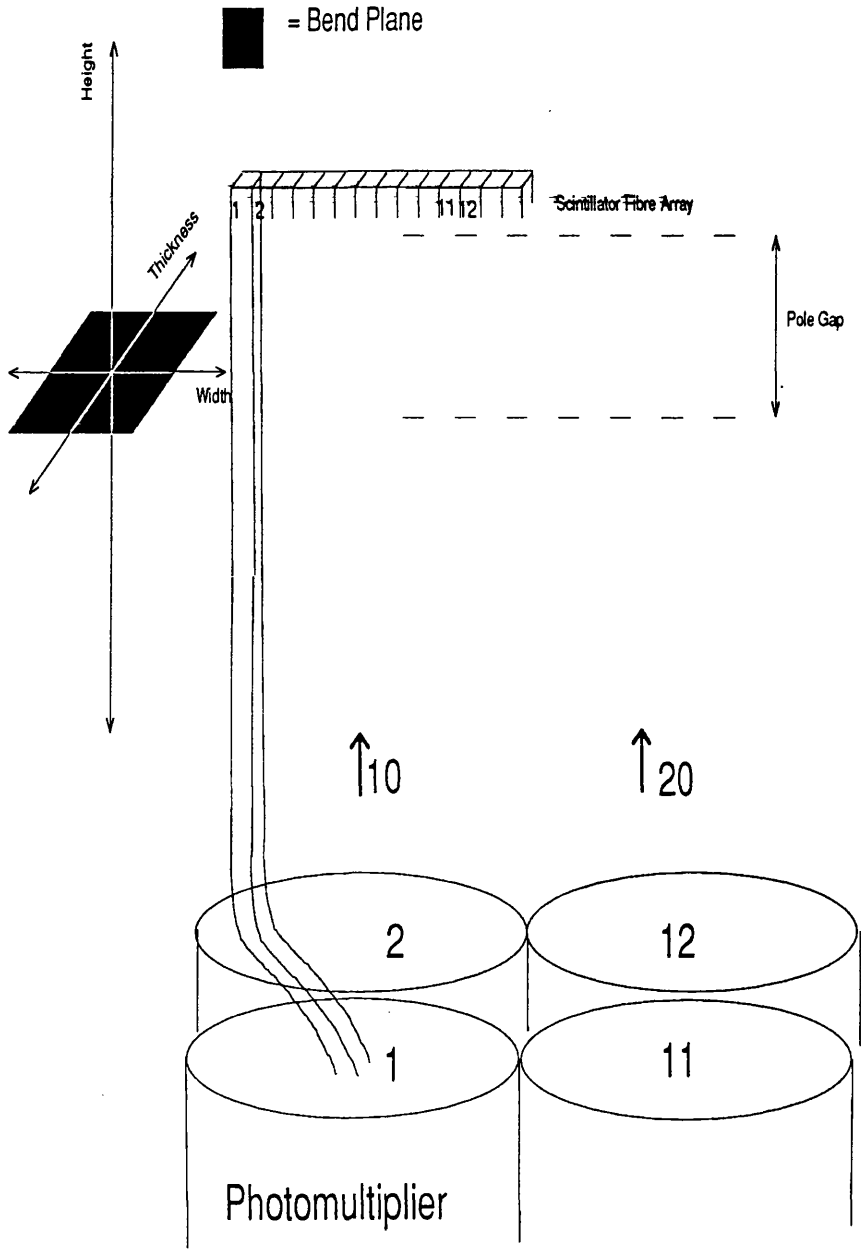

Figure 2.3: *Proposed Design for a Fibre/Photomultiplier Detector Array*

ionising in 2 mm of scintillator. This has been deduced from FIGURE (2.4), which shows the differential collisional energy loss of electrons in scintillator, plotted against electron energy. Since the differential energy loss of minimum-ionising electrons increases very slowly with energy, the graph was not extended above 2 MeV, to values in the 100 MeV $\rightarrow$ 800 Mev tagger range. However, the differential energy loss of a 100 MeV minimum-ionising electron is 204 eV.μm^{-1} and it is this value that will be used in the calculation.

The light output response is 58% anthracene, where the average energy deposited in anthracene, to produce one photon, is 60 eV for impinging electrons. Therefore, for the said trapping efficiency in a 2mm thick fibre, the number of trapped photons equals;

$$\frac{58 \times 204 \times 2000 \times 3.4}{100 \times 60 \times 100} = 134 \qquad (2.2)$$

The quantum efficiency of the photocathode is of the order of 10%-20% , so the number of photoelectrons entering the multiplier is around fifteen. The current focal-plane scintillator/photomultiplier configuration, with a higher effective trapping efficiency, typically produces about eighty photoelectrons per event and gives a signal:noise ratio which is adequate to distinguish the real events [9]. Whether, for a fibre, the reduction in the number of photoelectrons can be tolerated, must be determined experimentally.

This question was investigated using a ^{207}Bi source to provide the electrons. The decay scheme is illustrated in FIGURE(2.5). The relative probabilities of each of the possible gamma decays are listed in TABLE (2.1). Also listed is the probability of producing conversion electrons and the K/L shell ratios for each transition.

The range of electrons in scintillator is plotted in FIGURE (2.6). It can

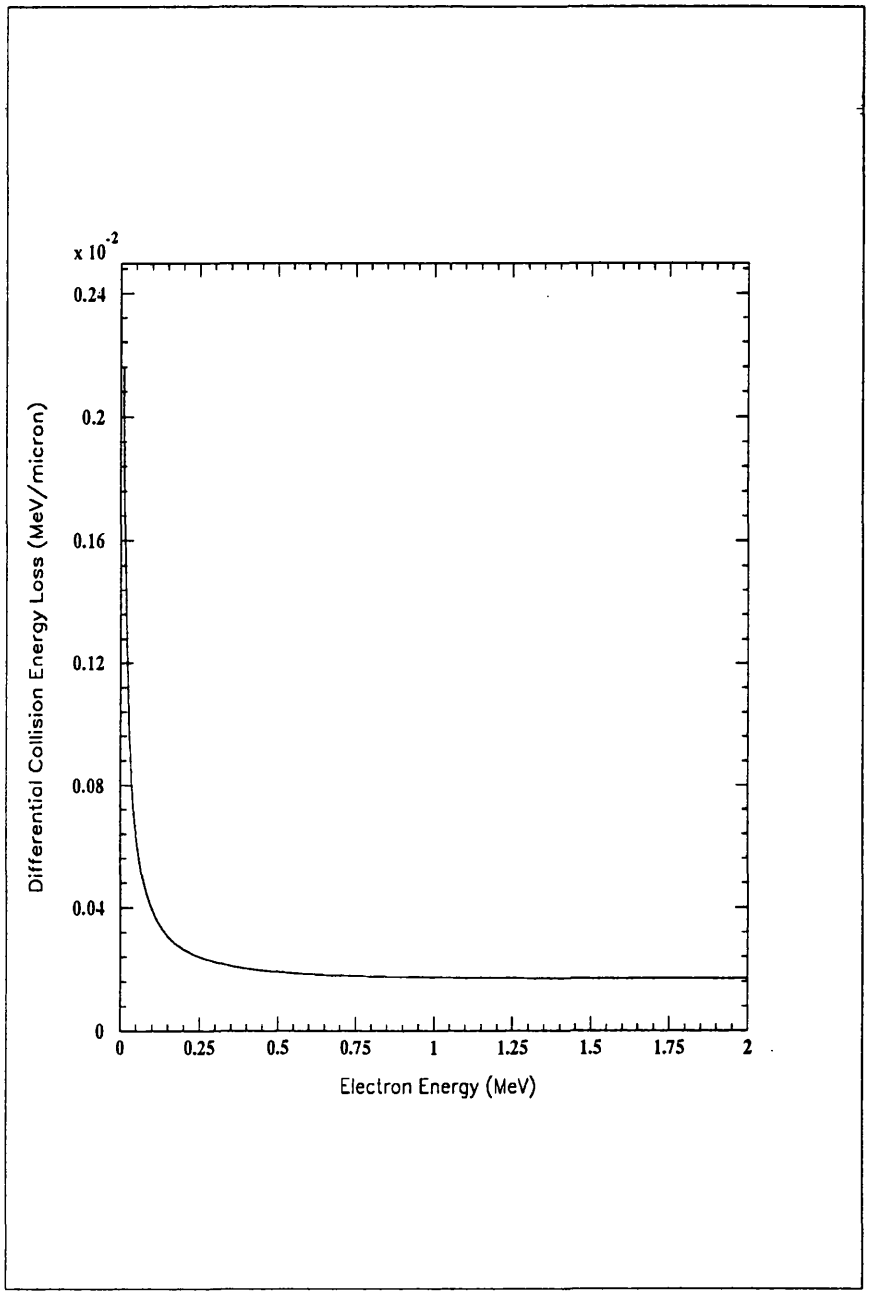

Figure 2.4: *The Differential Energy Loss of Electrons in Scintillator.*

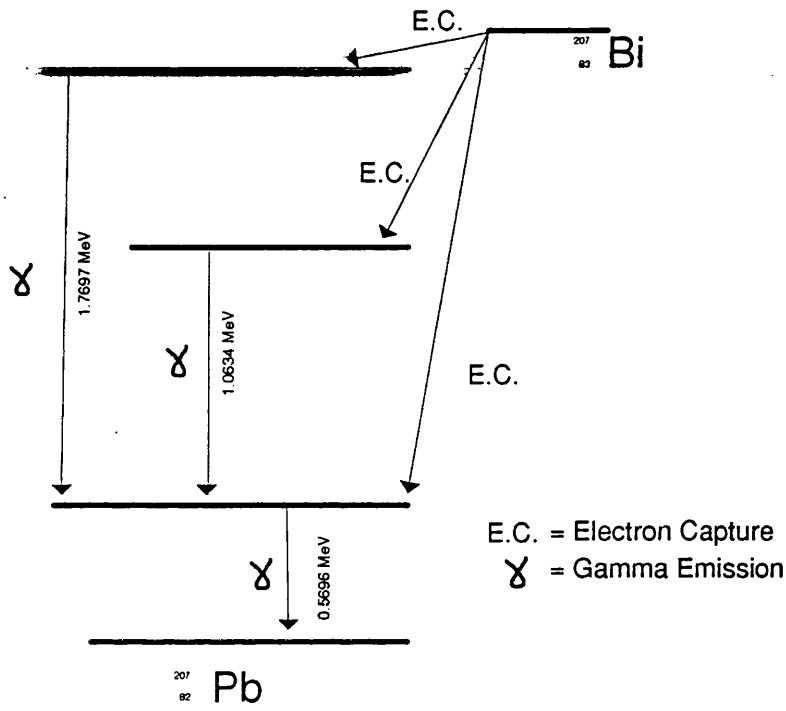

Figure 2.5: *The Bismuth 207 Decay Scheme*

Transition (MeV)	Relative γ Intensity	Internal Conversion: e/γ Ratio	K/L Shell Ratio
0.5696	100.00	0.0160	4.0
1.0634	75.50	0.0985	3.7
1.7697	6.95	0.0034	4.6

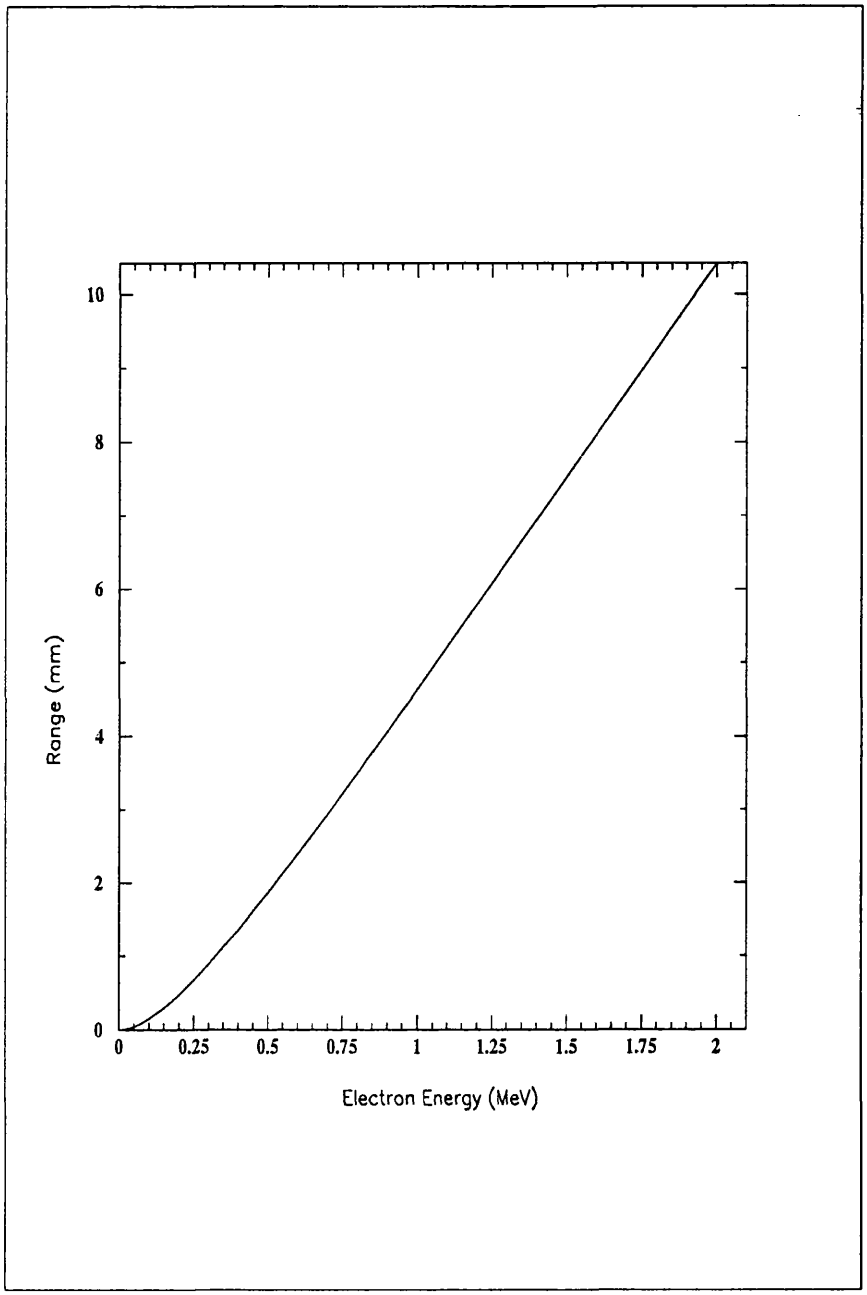

Figure 2.6: *The Range of Electrons in Scintillator.*

be seen from FIGURE (2.6) that the K-(481.7 keV) and the L-(554.0 keV) conversion electrons of the 569.6 γ transition, have mean ranges of 1.7 mm and 2.1 mm respectively. The 481.7 keV conversion electrons will therefore be fully absorbed in 2 mm of scintillator. The 554.0 keV conversion electrons will deposit most of their energy for the 'straight through' case , but with a deviation of 17° to the normal, they would be fully absorbed. The 1.063 MeV conversion electrons have a mean range of around 48 mm. From FIGURE (2.4), these electrons are minimum-ionising in 2 mm of scintillator and correspondingly lose about 350 keV on average. Electrons would have to be deviated 65° to the normal to be fully absorbed. A 100 MeV electron loses about 409 keV, so the 1.063 MeV conversion electrons offer a good simulation of the higher energy electrons which strike the tagger.

The "B.C.F.12" scintillator fibre used in the test has the following specifications;

DIMENSIONS: 2 mm^2 x 13 cm long.
ATTENUATION LENGTH: 220 cm.
WAVELENGTH OF EMISSION MAXIMUM: 435 nm.

The $2mm^2$ fibre surface was in direct contact with the window of a "Thorn EMI 9813KB" phototube 50 mm in diameter. A good optical contact was ensured between the fibre and the phototube window with silicon grease. The fibre was clamped in place by enclosing it in a 20 mm thick brass cuff taped to the phototube window. Light collection was optimised in the fibre with one loose layer of aluminium foil forming an air gap, to increase the probability of internal reflection at the cladding/air interface. The assembly was then made

light-tight with two layers of masking tape. The combined thickness of foil and tape caused negligible electron energy loss.

The electronic set-up, based on NIM and CAMAC units, is outlined in FIGURE (2.7). The output of the photomultiplier was fed into a fast amplifier. The output from the amplifier was split with one part being delayed and attenuated, before being used to record the pulse height spectrum from the fibre in an ADC (Analogue to Digital Convertor), while the other part was used to trigger a constant fraction discriminator. The discriminator output was used to start the Lecroy 222 Gate Generator, the output from which was used to gate the ADC and to interrupt a VME computer. The computer then read out the ADC using the ACQU system developed by J.R.M. Annand,[10] and transferred the data to a VAX computer for display. The gate generator was operated in 'latch mode', to block further discriminator pulses from triggering the gate generator while data was being recorded. It was reset by a pulse issued by the last instruction of the computer read-out sequence (output from ACK2 in FIGURE (2.7)).

A 2 mm thick x 20 mm^2 slab of NE102A scintillator with similar light output to the scintillator fibre, was then substituted for the fibre and the experiment repeated. With the same 2 mm thickness the incident electrons traversed a path-length equal to that in the fibre. However by choosing such a large surface area relative to its depth and coupling it flat, directly onto the phototube surface, again using silicon grease, a significantly larger "trapping efficiency" could be assumed, against which to scale the fibre performance.

Rough collimation was employed in both tests to ensure that the range of incident electron angles at the scintillator, was almost independent of the area

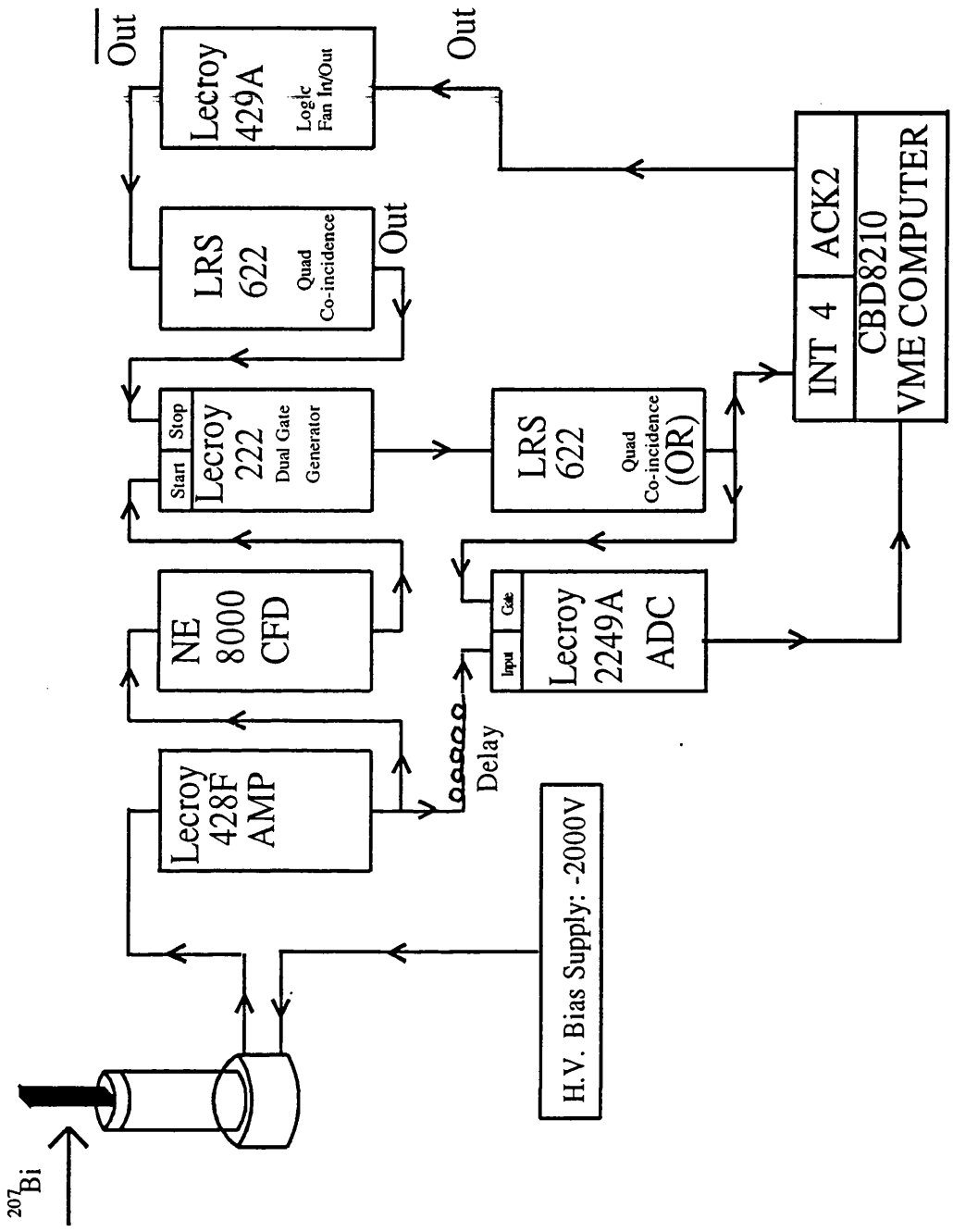

Figure 2.7: *Circuit Diagram for Scintillation Fibre Test.*

of the scintillator surfaces. The collimator was 25 mm long and 10 mm in diameter. The source was placed against the end of the collimator, so that the source → scintillator distance was 25 mm. This meant that electrons from the source, which was centered on the collimator axis, were limited to incident angles of $< 11^{o}$, corresponding to a maximum increase in pathlength of 10%. It can therefore be assumed that the only significant factor in the number of photoelectrons incident on the cathode is the "trapping efficiency". By limiting the incident trajectory of the electrons in this way, the probability of the scintillator fully absorbing a 1.063 MeV conversion electron is much reduced. In this case, scatter within the scintillator is the main factor in the appearance of the full energy peak for 1063 keV conversion electrons in the spectra recorded both by the scintillator fibre and the NE102A.

FIGURE (2.8) illustrates the pulse height spectrum recorded by the scintillator slab. The 1063 keV conversion electrons' full energy peak is clearly defined at channel 212, but the k and l shells are not resolved. The peak consists mainly of k shell electrons and is therefore expected to peak at 975 keV. The 570 keV conversion electrons appear as a shoulder at about channel 112, but ride on the energy distribution from the 1063 keV conversion electrons. Again, this peak is due mainly to k shell electrons and is therefore expected to peak at 482 keV. The energy distribution curve from the 1.063 MeV conversion electrons peaks at about channel 97. This peak corresponds to the average amount of energy deposited by a collimated minimum-ionising particle in the slab and should therefore be just above 350 keV, calculated for an electron going straight through the detector. In FIGURE(2.9), the ADC channel number is plotted against the energy of these three peaks, to energy calibrate the pulse height spectrum. The linearity of the graph indicates that the deductions made

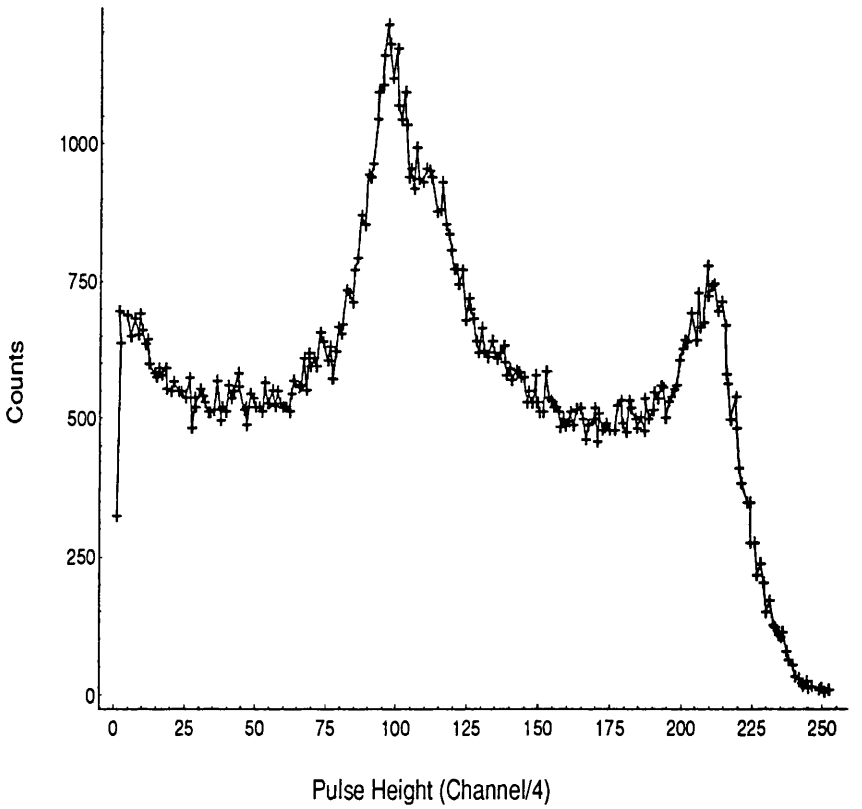

Figure 2.8: ^{207}Bi *Pulse Height Spectrum in the Slab.*

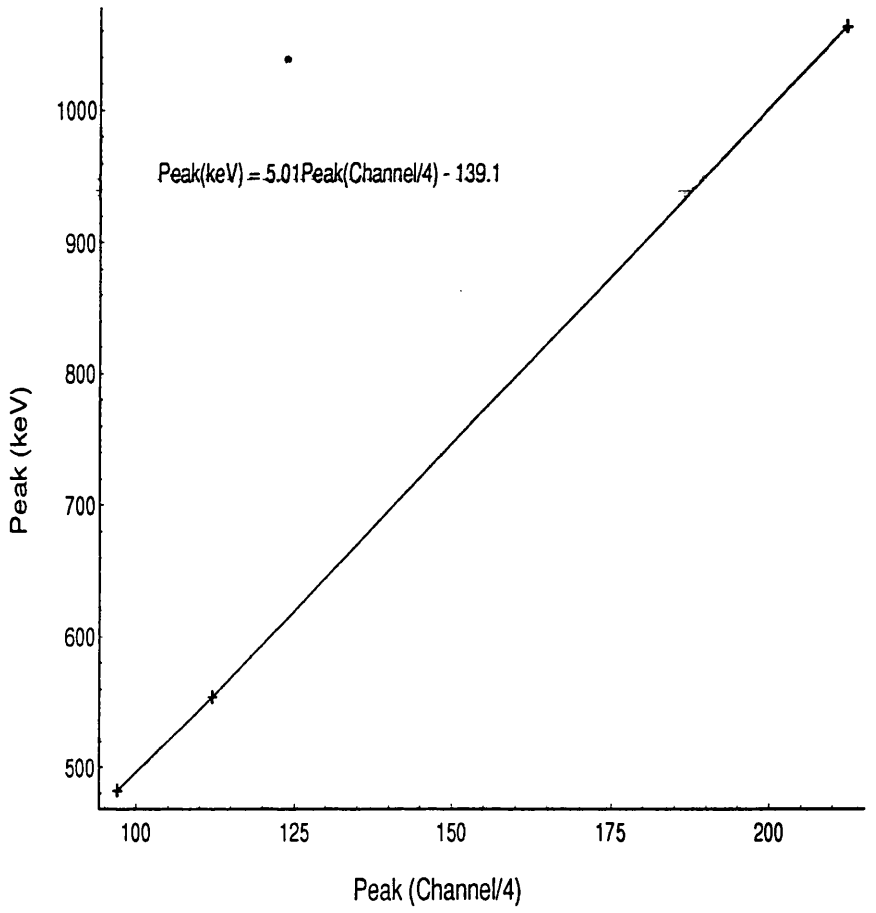

Figure 2.9: *Energy Calibration of Scintillator Pulse Height Spectrum.*

about the energies of the peaks in the pulse height spectrum are indeed valid.

FIGURE (2.10) shows the pulse height spectrum from the fibre, for a collimated source incident normal to the fibre surface. In comparison to the spectrum obtained from the slab, resolution is observed to be severly degraded. The only hint of a peak that can be distinguished is full energy peak of the 1.063 MeV conversion electrons around channel 40, but it is not clearly resolved. The noise is seen to rise sharply at low pulse heights, until it is cut off by the

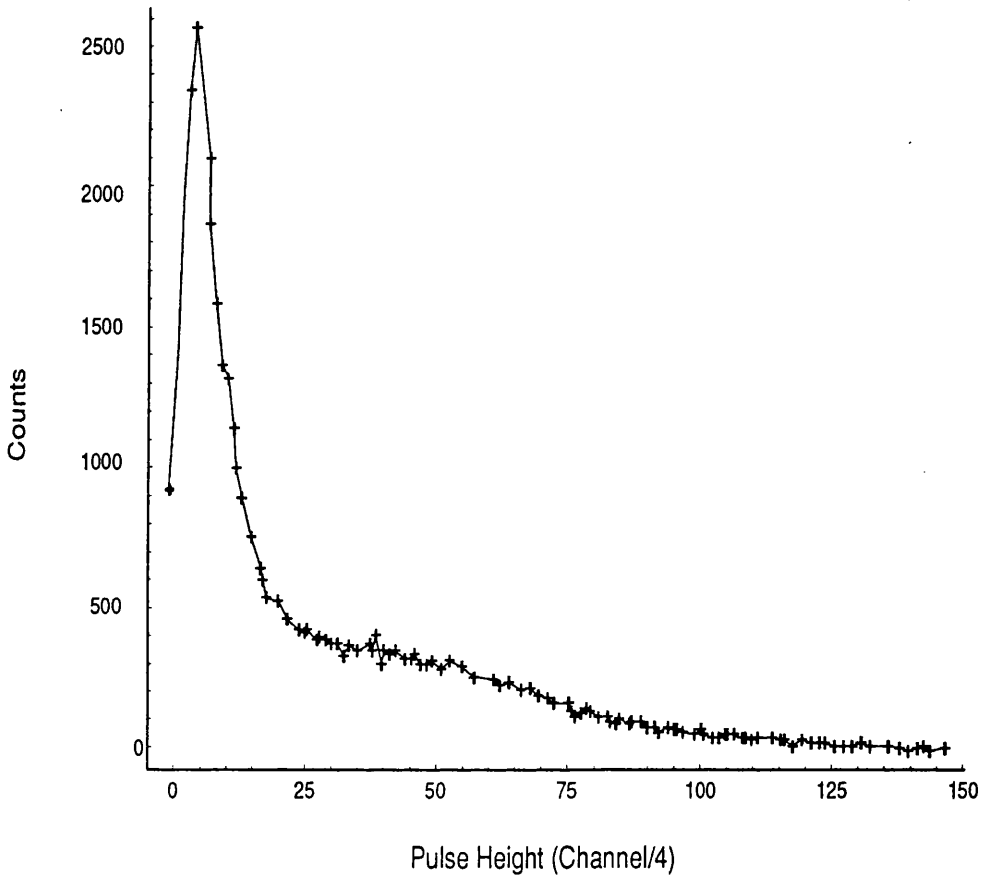

Figure 2.10: ^{207}*Bi Pulse Height Spectrum in the Fibre; Collimated*

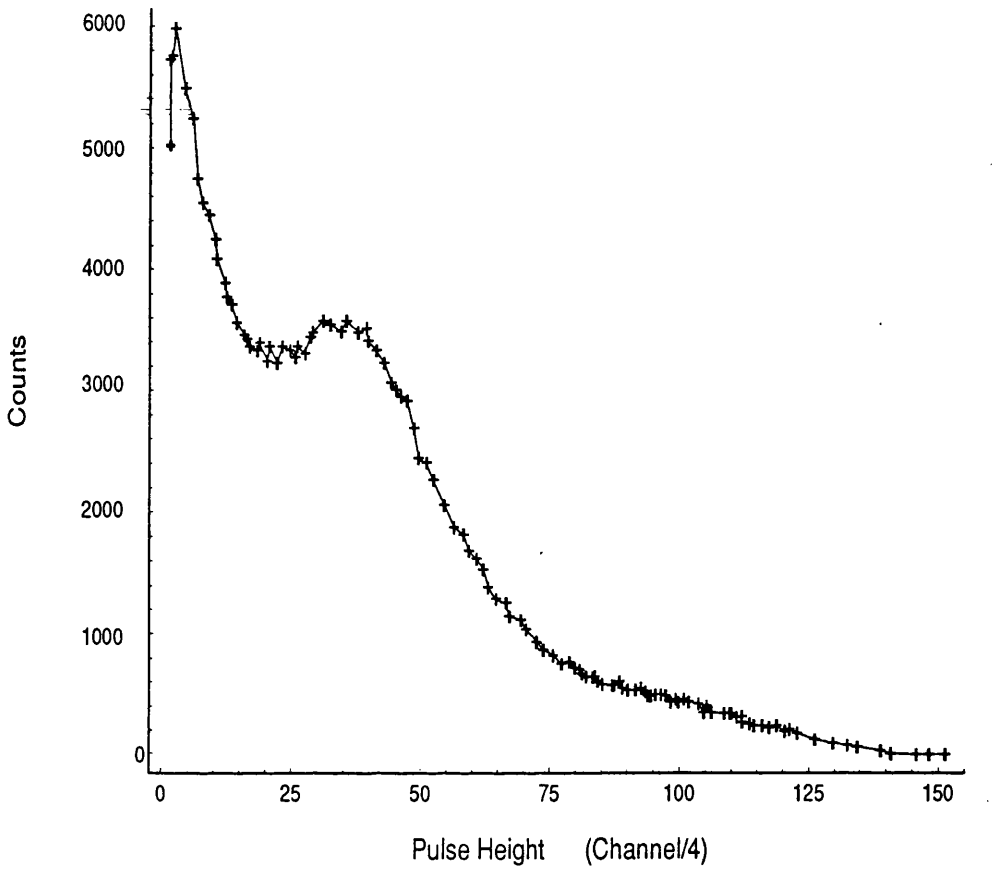

Figure 2.11: ^{207}*Bi Energy vs Count Rate Spectrum in the Fibre; Uncollimated*

discriminator at channel 10.

For comparison, FIGURE (2.11) illustrates the case of an uncollimated source, placed 5 mm from the fibre surface. In both the collimated and uncollimated cases, the source was positioned 30 mm from the end of the fibre, to avoid anomalies due to attenuation. Due to the large range of incident electron angles on the fibre, the average path-length through the detector is larger than in the "straight through" case. There is therefore a correspondingly higher prob-

ability of the 1.063 MeV conversion electrons being fully absorbed and the peak is enhanced, relative to the noise. The peak can be clearly distinguished about channel thirty-five. This represents a factor of ~6 reduction in the trapping efficiency compared to that obtained from the scintillator slab and therefore a factor of six less photons reaching the photomultiplier. The slab would be expected to show the full energy 1 MeV peak at a channel ~15 times higher than that of the fibre, if surface defects were removed and the scintillator was as good quality, but this was not the case here.

Given that a minimum ionising electron of energy greater than 100 MeV deposits approximately 408 keV in the fibre, it is essential to be able to discern the 570 keV conversion electrons from the noise in the fibre tests. The only obvious way to do this would be to increase the fibre thickness. However, as previously stated, a significant increase in thickness gives rise to an increased background and more scattering into neighbouring detectors.

2.2 Multicathode Photomultipliers

Multicathode Photomultipliers (MAPMT's) have a limited lifetime of typically 100 Coulombs before the gain drops to 50% of its initial value. This figure can be used to determine the maximum mean anode current that should be output from the detector, if the detector is to last for ~5 years. The maximum mean anode current can then be used to estimate the maximum number of photons that can be induced in the scintillator, by the degraded electrons from the radiator, over a period of 5 years. The data used in this calculation, which is considered to be typical of MAPMT'S, was extracted from the specifications given for a "MULLARD XP4702" [11];

MAXIMUM RADIANT SENSITIVITY: 400±30 nm.

CATHODE RADIANT SENSITIVITY AT 400nm: 40 mA/W (=11% quantum efficiency).

TYPICAL GAIN AT 1250V: 1.0 X 10^6 .

OUTPUT PULSE RISETIME AT 1250V: 4.8 ns.

OUTPUT DARK CURRENT PER OUTPUT ELEMENT: 1 nA.

MAXIMUM OUTPUT CURRENT PER ELEMENT: 5 μA.

MAXIMUM TOTAL OUTPUT CURRENT: 50 μA.

PHOTOCATHODE PIXEL PITCH: 2.5 mm X 2.5 mm.

The maximum recommended gain is $\sim$ 6 x 10^6, but this calculation is done assuming that the gain is set at a value of 1.0 x 10^6, which from the specifications has a fast enough rising edge for 1 ns timing. This way, there is scope for the voltage to be increased, to compensate for the drop in gain with use. Such compensation can continue until the voltage reaches its maximum, permissable value, but only gives a gain of 1 x 10 ^{6}. The anode current will be calculated such that this happens after $\sim$5 years. Therefore 5 years represents the end of the photomutiplier lifetime, if this gain has to be maintained.

The centre to centre scintillator spacing in the current detector array is 13 mm. Neglecting the fact that one of the objectives is to increase the maximum, tolerable beam intensity, the current limit on the rate is 3x10^6 Hz/channel. The corresponding rate for a 2 mm wide fibre, therefore equals 0.46 MHz/channel.

For a MAPMT to reach the end of its useful life after 5 years, the gain will decrease by a factor of 2 in $\sim$2 years The mean anode current allowed per channel, assuming all sixty-four channels are operational, is therefore 0.085 μA.

For a gain of 1 x 10^6, the mean, maximum number of photoelectrons produced in the cathode per electron in the fibre, that will result in the above mean anode current, can be calculated from the MAPMT specifications;

$$n = \frac{I}{qe \times BI \times G} \tag{2.3}$$

where n = the No. of photoelectrons produced in the cathode,

I = the mean anode current/channel = 0.085 μA,

qe = the charge of one electron; = 1.602 x 10^{-19} C,

BI = the channel count rate = 0.46 MHz,

and G = the MAPMT gain = 10^6.

n therefore equals ~1.

For a quantum efficiency of ~15 %, ~10 photons must be incident on the photocathode. In §2.2, with 15 photoelectrons/ event, resolution was demonstrated to be inadequate. Indeed, about 80, as produced in the present focal-plane scintillators, would be desirable. It is clearly not possible to operate the MAPMT/scintillator configuration at such a small anode current without constraining the gain to a factor of about 80 less than 1 x 10^6, to avoid burn-out in 5 years. The specifications indicate gain to be linear down to at least 800 V, with a typical gain of 10^4, so such a reduction is permitted, without loss of linearity. Sacrificing gain is accompanied, however, by an increase in transit time spread, which implies bad timing. It is unlikely that 1 ns timing could be obtained from a phototube whose rising edge was significantly larger than the 4.8 ns obtained at a gain of 1 x 10^6, particularly if the signal:noise ratio is poor. Things would become even worse, if an increase in the tagged photon rate were attempted, as outlined in the objectives in §1.1.

Thus, due to the difficulties which would have to be overcome to obtain a good enough signal:noise ratio in scintillator of the required dimensions, together with the problems of reading out the scintillators into a suitable phototube, the scintillator/photomultiplier option was not pursued further.

Chapter 3

A Silicon Microstrip Detector

3.1 A Silicon Microstrip Detector

A junction detector is essentially a solid state ionisation chamber. Radiation incident on the detector induces pairs of charge carriers in the non-conducting, active detector area. An electric field is provided across the active detector area, which sweeps the opposite polarity charge carriers towards oppositely charged electrodes. The motion of these charge carriers induces a signal pulse at the electrodes, characteristic of the energy and type of radiation incident. Often junction detectors are position sensitive and are read out by a charge division method. This kind of readout requires a very homogeneous resistive layer and a thick detector to give a very high signal:noise ratio. An alternative is to segment one or both electrodes and thus produce a discrete array of readout elements. This is called a microstrip detector. Although the individual readout of the elements requires more electronics, the constraints on signal:noise and homogeneity can be relaxed. This is the better option for a focal-plane detector array, since the charge collection time increases with thickness, which generally implies poorer timing. Silicon is generally used as the base material for these detectors, because it can operate at room temperature.

A silicon microstrip detector was therefore investigated as an alternative to the scintillator/photomultiplier configuration, because of the following properties:

(1) Stopping power is increased due to the higher density of the crystalline, silicon structure.

(2) When a silicon detector is irradiated, the signal pulse produced is induced by the motion of the electron-hole pairs that are created. The average

energy required to create such a pair in silicon is 3.62 eV at 300 K. This is a factor of one hundred lower than that needed to produce a photon in a plastic scintillator and the number of ionisations produced per event is therefore correspondingly increased. In general, the resultant resolution is given statistically for minimum-ionising particles, where each ionisation can be considered approximately independent, as

$$\frac{1}{\sqrt{N}} \tag{3.1}$$

where N is the number of ionisations. This means that for the same effective thickness, silicon produces a factor of ten better resolution than scintillator. This factor further increases for thicker detectors, where electrons are no longer minimum-ionising and the individual ionisations cannot therefore be considered independent, since the total energy deposited is constrained to its physical limit. The above expression for resolution is multiplied by a theoretical weighting factor known as the Fano factor to take account of this. This equals 0.05 for silicon and 1 for scintillator, improving the resolution by another factor of twenty. One disadvantage of a silicon detector however, is poorer timing resolution, due to the relatively low velocity of the electrons and holes in silicon

.

3.2 Principles of a Microstrip Detector.

A microstrip detector works on the following principle: First consider an isolated p-n junction: When an n-type semiconductor comes into contact with a p-type region, a concentration gradient exists across them. However, in the absence of any applied bias, such as electric field, the charge carriers should be evenly distributed throughout the two regions. This means that there will

be a net flow of charge carriers, until their random motion redistributes homogeneously them throughout the junction. Holes from the p-type side diffuse over to the n-type side, while electrons from this side diffuse over to the p-type side. Having diffused into the other region, these particles will then combine with the region's opposite-polarity "majority carriers". This causes a build-up of immobile space-charge, extending out from either side of the junction into what were previously neutral areas, so that a gradually increasing potential difference begins to form across the junction, which inhibits the diffusion current FIGURE (3.1) illustrates the build-up of this immobile space-charge, together with the electric field and charge density distribution in the junction.

Electrical neutrality must be preserved within the junction, so equal quantities of charge are formed on either side of it; an electron leaving the n-type and so negating the p-type side leaves behind a hole and vice-versa for a hole exiting the p-type side. However, the charge density, ρ, will vary with the ratio of impurity concentrations in each region, as dictated by how probable it is for a diffusing charge carrier entering the other region to combine with its opposite polarity, majority counterpart within a certain length. The area in which the bulk of immobile space charge is concentrated is known as the "depletion zone", so called because it remains essentially depleted of all mobile charge carriers.

If this were the only process to be considered, diffusion would continue, while its rate would keep reducing, until, as stated, the charge carriers were evenly distributed and for identical quantities of p and n-type dopant, all holes and electrons had combined to form immobile space-charge throughout the junction. However, there are also thermally-generated "minority carriers" produced in each region. These are swept into the opposite one by the increasingly

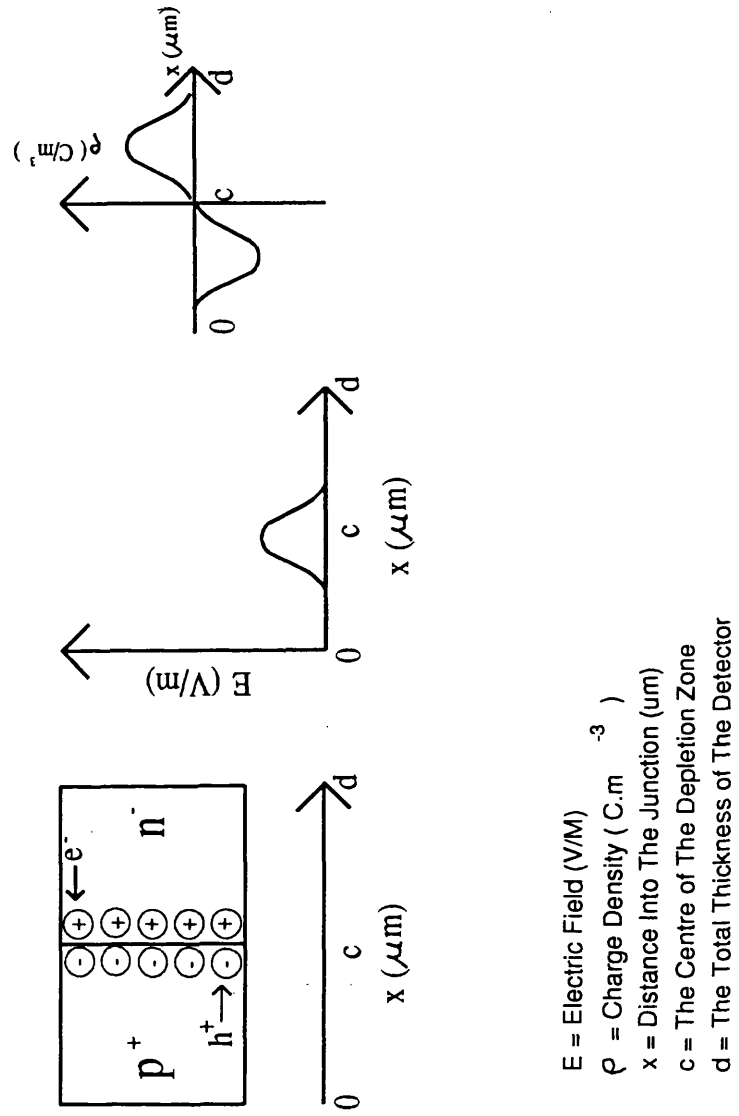

Figure 3.1: *Charge Distribution In a p-n Junction*

favourable potential difference, so forming a thermally-generated current, referred to as the "leakage current", flowing in the opposite direction to the diffusion current. Since thermal generation, being the source of this current, is a relatively improbable event at normal temperatures, this current is independent of potential difference within the working region of the diode and remains constant for a constant temperature. Equilibrium is therefore reached when the diffusion current has decreased to such an extent that the opposing currents are equal. The size of the depletion zone is therefore only a fraction of the total device thickness and is temperature dependent.

The diffusion current and therefore also the equilibrium size of the depletion zone, can be altered by biasing the charge carrier distribution by applying a potential difference. If the potential is applied across the junction such that the more negative value is connected to the p-type side, then the diffusion current is decreased. This is known as "reverse biasing the junction".

Here, the battery, having a larger potential difference than the contact potential of an isolated junction, charges it up like any parallel plate capacitor. In this case, the non-conducting dielectric is the depletion zone and the boundaries between the depletion zone and the conventional p/n-type semiconductor are the capacitor plates. FIGURE (3.2) shows the increased region of space-charge formed, together with the corresponding change in the electric field and charge density distributions.

Unlike conventional capacitors, the thickness of the dielectric medium changes as the potential increases. In this case, the electrons fed into the junction by the battery at the p-type side combine with the majority carrier holes nearest the depletion zone, so forming more of the immobile space charge that con-

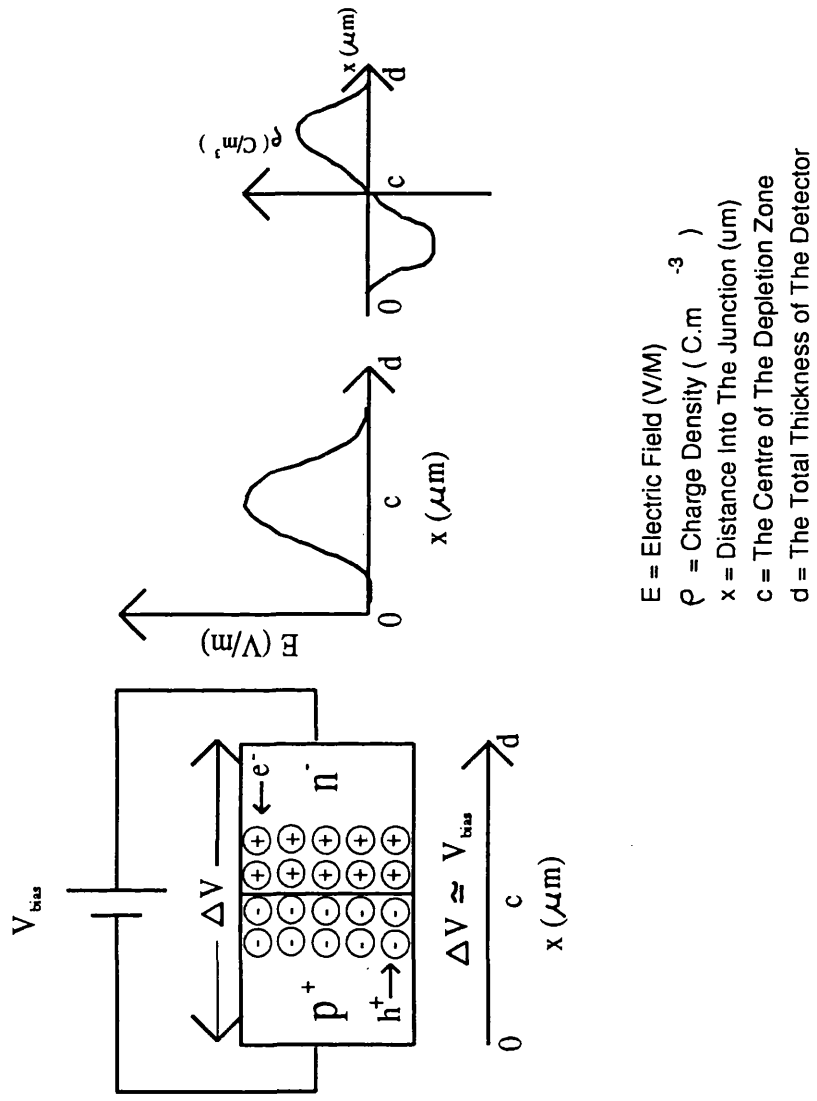

Figure 3.2: *Charge Distribution Across a Biased p-n Junction.*

stitutes the depletion zone. Similarly, the charge induced on the n-type side, by this build-up on the p-type side, forces an equivalent amount of majority electrons out of the junction and the remaining space-charge again constitutes a corresponding increase in depletion zone thickness. Equilibrium is reached when the potential across the depletion zone equals that of the battery. At this point, the only current that is flowing is the thermal current and a very small diffusion current and the equilibrium is maintained by the battery. For the particular case of a potential large enough to force the depletion zone to extend across the entire junction, there is no diffusion current since there are no mobile charge carriers left in the junction. At this point the junction is "fully depleted".

Radiation passing through the depleted detector generates charge at the electrodes as described in §3.1. FIGURE(3.3) illustrates the charge pulse induced on the p^- electrode by an electron-hole pair conceived at some arbitrary position within the depletion zone. The shape of this charge pulse will vary with the initial position of the electron-hole pair, since their drift velocity will be determined by how strong the electric field is at that point. In turn, this velocity determines the rate of change of the charge induced at the depletion zone edges and therefore the gradient of the leading edge. A further complication is that at normal temperatures, electrons have a larger mobility than holes, so there is no symmetry of motion about the centre of the depletion zone. The resultant output pulse is a superposition of the charge induced by the migration of each individual electron-hole pair created. The total charge induced at either one of the zone edges however, is constant and independent of initial position, providing that all charge is collected. In any real situation though, the charge leaks off the detector electrodes, at a rate determined by the resistance

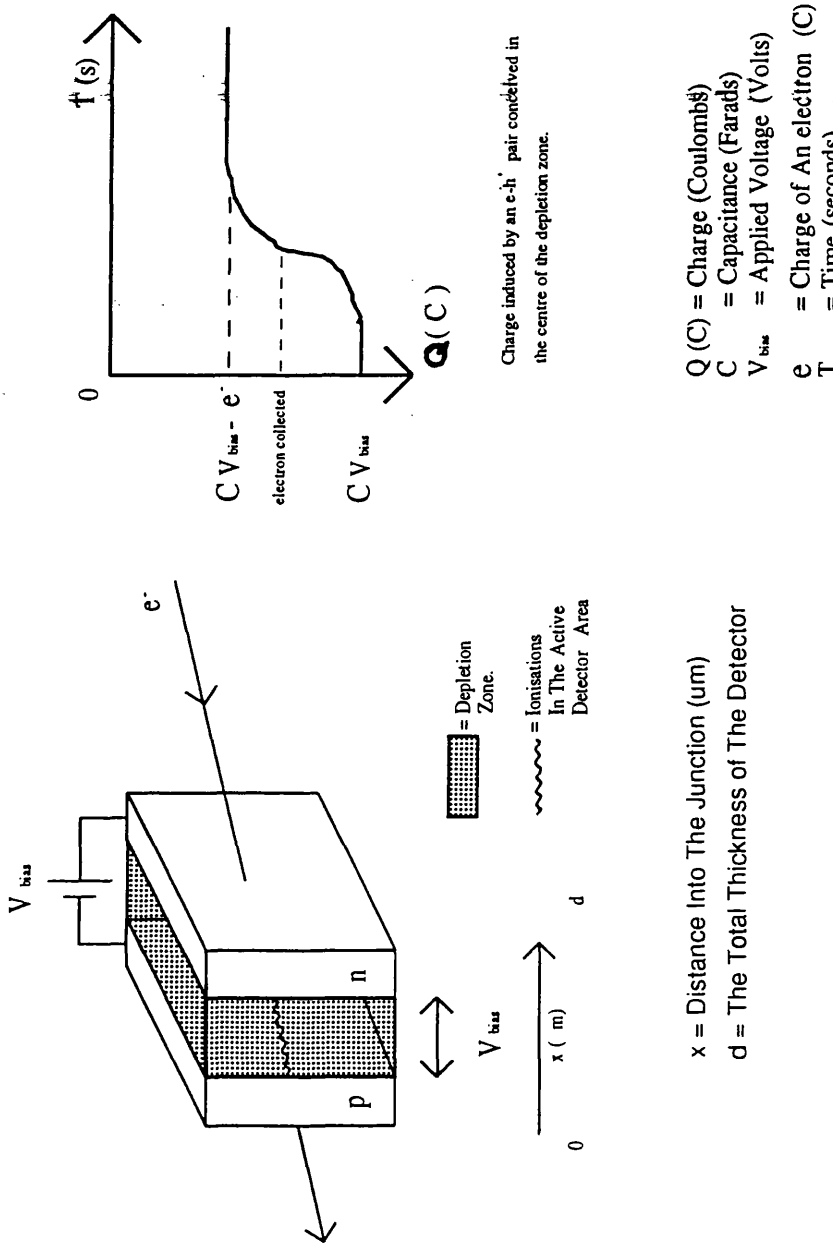

Figure 3.3: *Pulse Induced by Migration of an e-h Pair*

of the external circuit. For this reason, any practical junction detector has a large resistor inserted between the bias supply and the detector itself, so that capacitive leakage is minimised within the charging time of the detector.

3.3 A Practical Strip Detector

For any practical application there are various considerations in optimising the operation of a strip detector. They can be summarised as follows:

(1) An energy gap small enough to yield a large number of electron-hole pairs from the impinging radiation is needed to produce a large number of e^--h^+ pairs. The practical limit is that set by the corresponding increase in leakage current as the gap is reduced.

(2) High resistivity is required. The electric field gradient across the depletion zone is dependent on the space charge concentration within it and so, on the resistivity. To obtain good timing, a larger potential difference than that required to reach full depletion, is applied. There is a physical limit on the degree of over-biasing which may be applied, however. The larger the electric field, the faster the charge carriers accelerate. To retain equilibrium, the lattice must absorb the extra kinetic energy that the charge carriers gain from the field. There is however, a finite limit on the rate at which such absorbtion can take place. Above this, a non-equilibrium situation develops where the carriers cease to exhibit the thermal velocity characteristic of the lattice temperature, but rather adopt a Boltzmann distributed velocity distribution, in accordance with the absorption probability distribution of the carrier energy by the lattice. At this point, the charge carriers are known as "hot". Due to the increased friction term associated with the lattice at this point, carrier mobility decreases

and the rate of change of drift velocity with electric field departs from the linear relationship observed at equilibrium At a temperature of 300 K and for electric fields between 10^5 10^6 V.m−1 mobility varies approximately with the square root of the electric field.

A second consideration when raising the applied voltage, is the increase in the thermal noise contribution. Thermal noise is a measure of the fluctuations in the voltage signal induced in the detector, due to the intermittent bunching of charge carriers, purely because of the variance of their velocity distribution. For hot carriers, this effect will therefore be particularly evident. This is detrimental to the signal:noise ratio.

Cooling the detector can hinder the rate at which mobility falls and thermal noise rises with electric field, by increasing the rate at which the lattice can radiate the excess energy into the surroundings. However, above electric field values of the order of 10^6 V.m^{-1}, mobility varies inversely with field and drift velocity reaches its maximum value. Carrier velocity is said to be "saturated" at this point. The exact magnitude of the electric field, when saturation occurs, is temperature dependent and the hole saturation velocity is more sensitive to temperature effects than that of an electron. The reason saturation occurs is that at this point, the charge carriers have gained enough energy to excite the optical modes of the lattice. Excess carrier kinetic energy can be efficiently mopped up, with the higher energy carriers simply causing a higher energy excitation. Finally, at $\sim 10^8$ V.m^{-1}, junction breakdown is reached.

It is therefore desirable to minimise the field gradient so that performance at the high field end is not compromised too much, before the field at the low field end has been adequately boosted. In practice however, it should be noted

that breakdown occurs at much lower fields than 10^8 V.m^{-1}. In high resistivity materials, this is due to breakdown at the resistive contacts, [12], while in lower resistivity detectors, where the field built up across the semiconductor-metal interface isn't as abrupt, the high field densities which can build up at the detector surface determine the upper limit. Thus lower resistivity detectors with overbias capability generally provide the fastest overall charge collection and therefore the best timing.

(3)A high purity material and therefore high resistivity, is required to stem the effects of recombination and trapping, which occur at impurity centres and lattice defects. Recombination refers to charge capture before complete collection occurs and so, reduces the charge collection efficiency. In trapping, charge capture also occurs, but only for a finite period. The trapped carriers may either be released to contribute further up the leading edge, or on the falling edge of the induced pulse. Pulse height can therefore be reduced, but the overall charge collection efficiency remains unchanged. In any real situation however, the distinction between the two is less apparent since relaxation mechanisms, which bring the system back to thermal equilibrium, become significant after some finite time. The net effect is a distortion of the leading edge of the current pulse and a reduction of the signal:noise ratio.

(4) Large electron and hole mobilities are needed to give efficient charge collection and fast risetime. It is also the case in a realistic strip detector, that vastly different impurity concentrations are used to fabricate the junction. Conventionally, p-type dopant is injected into high resistivity n-type material. The depletion zone therefore lies mainly in the n-type region and carrier transport properties are essentially determined by the n-type region. The electric field

for such a junction, can be approximated to that shown in FIGURE(3.4). For the case of the applied bias being more than that required for full depletion, a constant electric field, analogous to that seen across a conventional parallel plate capacitor, is superimposed on the approximately linearly increasing field observed in the depletion zone.

A detector with different dopant concentrations forming the junction can prove advantageous when the junction is less than fully depleted. With a negligibly small thickness, the p-type region will always provide a thin window for the impinging radiation, irrespective of bias voltage. Thus, the depletion zone thickness can be altered with an insignificant change in the scattering contribution from the window.

3.4 Detector Specifications

The detector chosen for tests was a "Silicon Planar Totally Depleted Ion Implanted Detector; P on N High Resistivity Silicon", supplied by MICRON SEMICONDUCTOR. It has the following specifications;

TOTAL DETECTOR AREA : 50mm X 50 mm.

NUMBER OF STRIP CHANNELS : 25.

AREA OF A SINGLE STRIP : 50 mm long X 2 mm wide.

BIAS REQUIRED FOR FULL DEPLETION : -90V.

MAXIMUM OVERBIASING CAPABILITIES : 50% over full depletion.

CONNECTIONS: 34-way pin connector, incorporating seven common A.C. grounds and two isolated D.C. grounds.

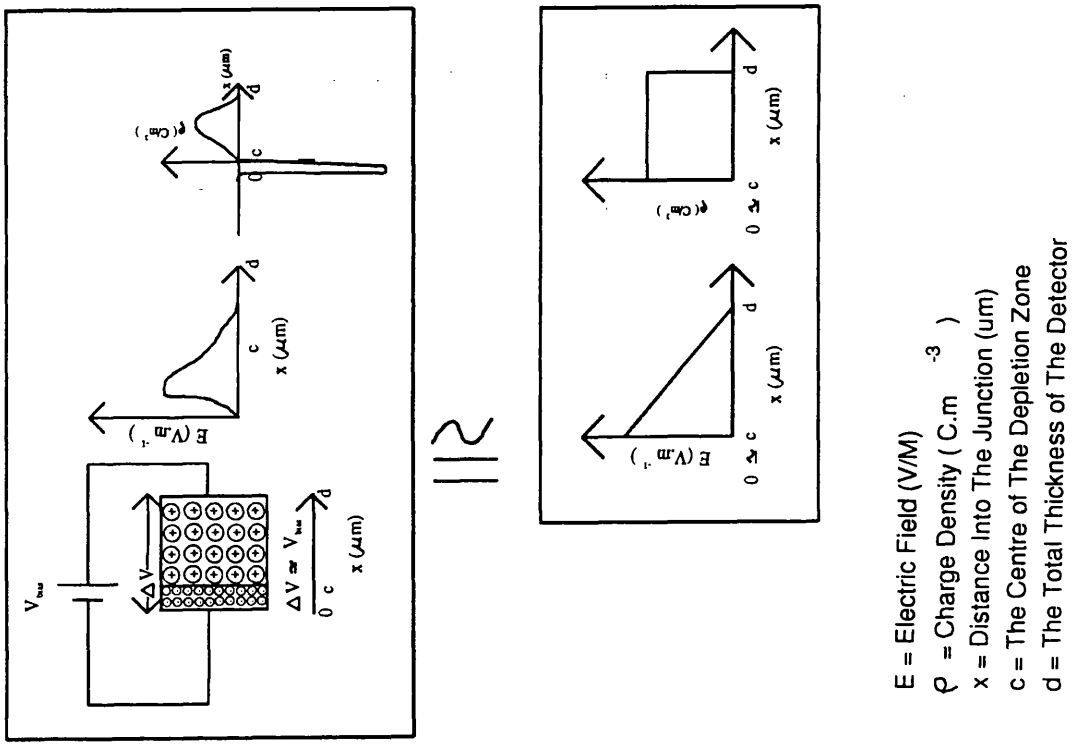

Figure 3.4: *Electric Field Across A p-n Junction ;* $\rho_n << \rho_p$

INTRINSIC RISETIME OF DETECTOR: 50 ns.

The associated resistivity of the n-type material and the detector capacitance can be calculated from the above information. Assuming a step function can approximate the charge distribution, as detailed in §3.2, and that the contribution of the p-type region is of negligible thickness, the resistivity can be shown to be given from the following formula [13];

$$\rho_n \simeq \frac{d^2}{2\epsilon\mu_n \mid V_{fd} \mid} \tag{3.2}$$

where ρ_n is the resistivity of the p-type region (Ω.m) ,

d is the detector thickness (= 500μm),

V_{fd} is the minimum bias for which the junction is fully depleted (= -90V),

ϵ is the permittivity of the dielectric.This is essentially that of intrinsic silicon (= $11.9\epsilon_0$,= 1.05 x 10^{-10} $C^2.N^{-1}.m^{-2}$).

and μ_n is the electron mobility at 300K (= 0.135 $m^2.V^{-1}.s^{-1}$).

This gives a value of 97.6 Ω.m for the resistivity.

The detector capacitance is given simply by the conventional formula for a parallel plate capacitor;

$$C = \frac{\epsilon A}{d} \tag{3.3}$$

where C is the capacitance (pF),

A is the strip area (= 10^{-4} m^2)

and d and ϵ are as before.

The resulting capacitance is 21.1pF.

This however is not the only capacitance of consequence. Stray capacitance

from cabling and other electronics and edge effects from the detector itself produces a much larger total effective capacitance of around 60pF.

Each detector strip has a typical leakage current of $\sim$ 200 nA, if operated around room temperature. The detector was however radiation damaged and the leakage current is a factor of $\sim$10 smaller for a virgin device. Using a radiation damaged detector is an accurate representation of the conditions under which the detector must operate, since crystalline materials are highly sensitive to radiation damage and it would be useful to extend the detector life as much as possible, before breakdown ultimately occurs. Therefore the signal:noise ratio obtained in any strip detector design must still provide a clear separation between signals and noise, when the detector leakage current is increased.

Other important factors pertaining to silicon itself are;

DENSITY OF SILICON:	2.33 g.cm^{-3} at 300K.
COLLISION STOPPING POWER FOR A MINIMUM IONISING PARTICLE OF GREATER THAN 100 MeV:	about 2 MeV.cm^2. g^{-1}, increasing very slowly with energy.

Detailed in FIGURE(3.5), is a graph of differential energy loss, dE/dx, for electrons in silicon plotted against the electron energy, while FIGURE(3.6) details electron energy versus range in silicon.

3.5 Pre-Amp Specifications

Unlike a scintillator/photomutiplier configuration, a strip detector has no intrinsic gain. Gain and shaping are therefore facilitated by an amplification system. The first stage of this is the pre-amp, which ordinarily provides the correct load

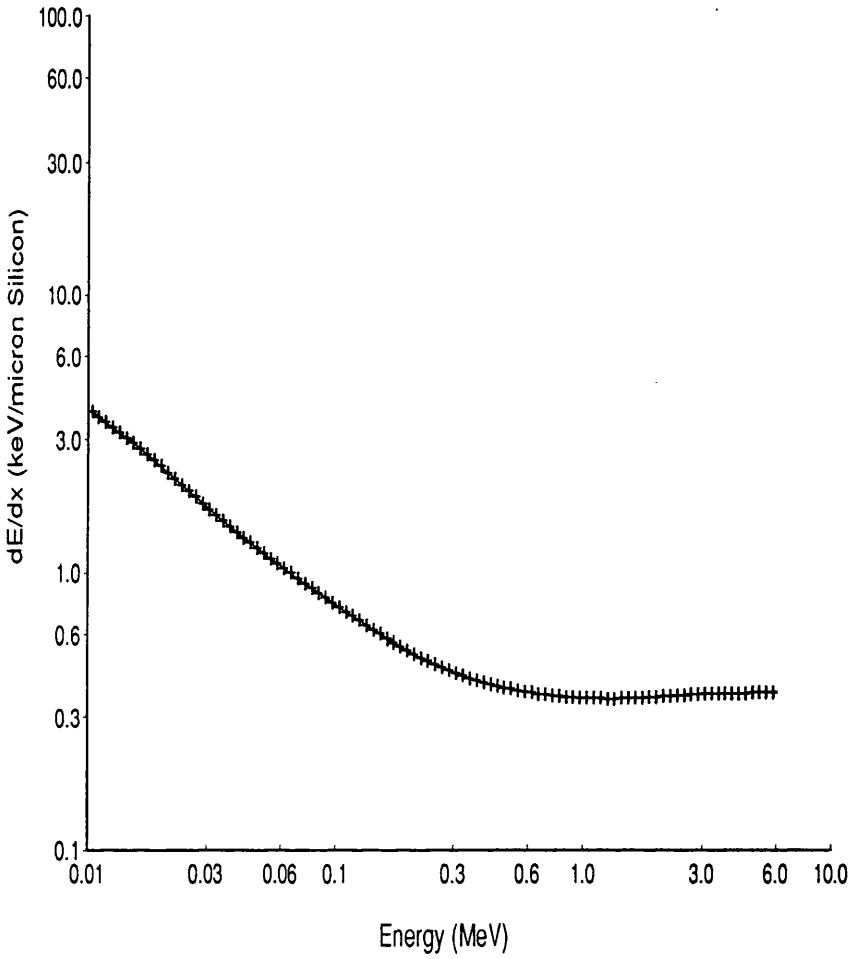

Figure 3.5: *Differential Energy Loss vs Electron Energy.*

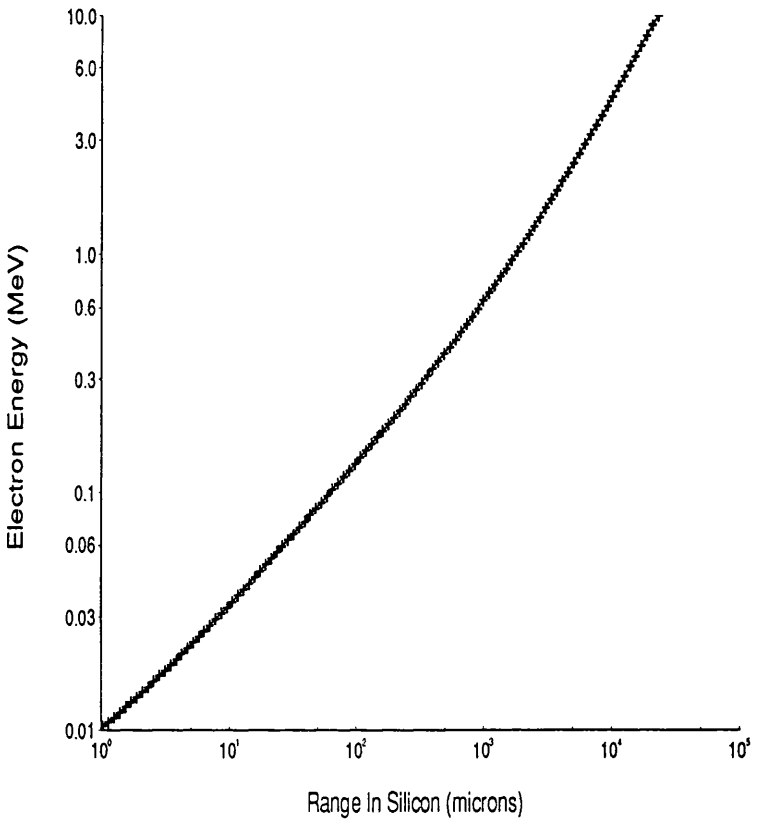

Figure 3.6: *Electron Energy vs Range in Silicon*

resistance for the detector and primary shaping and gain, to best enhance the signal:noise ratio. The one employed here has been developed at the Rutherford Appleton Laboratory (RAL) specifically for this type of detector [14]. It is a charge sensitive pre-amp. A current sensitive pre-amp, which at first sight appears to be the best kind of pre-amp for fast timing, was rejected due to the high leakage current and high capacitance of the detector. The large leakage current results in a signal:noise ratio which cannot provide a clear separation between signals and noise in current mode. The high detector capacitance, together with the detector and cable resistances and the input resistance of the pre-amp forms an RC time constant which determines the rate at which the charge leaks off the detector. For a pre-amp to be current sensitive, this must be small compared to the risetime of the charge pulse, so that the charge does not have time to accumulate on the detector electrodes. With a total effective detector capacitance of 60 pF and a risetime of 50 ns, the maximum acceptable resistance is a few Ω's. However, for the high frequency components of the current pulse, an input resistance of a few Ω's is difficult to attain. A current sensitive configuration is therefore, difficult to implement.

A charge sensitive configuration integrates the charge carried on the incoming pulse on a feedback capacitor. It is used in preference to a voltage sensitive pre-amp because the output voltage of a charge sensitive pre-amp is dependent on the value of the feedback capacitor, not on detector capacitance and is given by

$$V_o = \frac{Q}{C_f}, \tag{3.4}$$

where V_o is the output voltage,

Q is the charge built up on the detector

and C_f is the feedback capacitance.

A voltage sensitive pre-amp, because it is dependent on detector capacitance, is subject to variations in output voltage. Even in a fully depleted detector, where the depletion zone thickness is not temperature dependent to first order, temperature dependent fluctuations in depletion zone thickness and therefore capacitance are caused by changes to the detector surface states. A voltage sensitive pre-amp is however advantageous, when the intrinsic risetime of any charge sensitive pre-amp is greater than that of the detector pulse and therefore degrades the rising edge of the pulse, which is undesirable in fast timing applications. For the pre-amp used here it can be shown, [15], that the intrinsic pre-amp risetime is given by the following equation;

$$\tau' = \frac{\tau}{1 + A_o(\frac{C_f}{C_D + C_f})} \tag{3.5}$$

where τ' is the $0 \rightarrow 37\%$ risetime,

C_f is the feedback capacitance = 2.2 pF,

Ao is the amplifier open loop gain = 2500,

$\tau = 0.5\ \mu$s is the RC time constant of the amplifier.

and C_D is the sum of detector and detector to pre-amp connections capacitances $\sim$ 60 pF.

The intrinsic risetime of the charge sensitive pre-amp is therefore $\sim$ 12 ns, $10\% \rightarrow 90\%$. This risetime is significantly less than the intrinsic detector output pulse risetime. In this case, a voltage sensitive pre-amp would therefore offer no advantage. Indeed, since from EQUATION(3.4), output voltage in the charge sensitive pre-amp is inversely proportional to the capacitance of the feedback loop, a factor of two increase in gain could be achieved by halving the

value of the feedback capacitor without degrading the risetime. This can be achieved since the resultant factor of two increase in the amplifier risetime to 24 ns, by EQUATION (3.5), is still less than the detector output pulse risetime. There is no advantage in reducing the feedback capacitance to less than 1 pF, because stray capacitances would then contribute significantly to the value of the feedback capacitance and since stray capacitances are not necessarily constant, the gain of the circuit would vary.

A further advantage of increasing the amplification is that noise increases as the square root of the amplifier bandwidth. Clearly, the smaller the intrinsic pre-amp risetime, the larger the bandwidth must be, so it would be desirable to limit the bandwidth to no greater than the width required to reproduce the intrinsic detector output pulse risetime. For a factor of 2 increase in the intrinsic pre-amp risetime, the expected improvement in the signal:noise ratio, when other noise sources are considered, will be less than 1.4. This is not large enough to justify the difficulty of altering the surface mounted RAL 108 board for the tests, but should be kept in mind, if the questions of gain and signal:noise become paramount.

The charge sensitive pre-amp circuit is mounted on a thick film hybrid board designated "RAL108B", which has been designed to provide high density circuitry in accordance with the silicon strip detector dimensions. It has the following specifications;

SENSITIVITY: 20 mV/MeV.
NOISE: 3 keV FWHM (330 electrons rms) at 0 pF.
NOISE SLOPE: 90 eV/pF.
INPUT CAPACITANCE: 0 $\rightarrow$ 300 pF.

DYNAMIC RANGE 0 $\rightarrow$ 200 MeV ($\pm$4 V).

INTEGRAL NON-LINEARITY: 1%

OUTPUT IMPEDANCE: 100 Ω (AC coupled).

INPUT PULSE POLARITY: Positive.

FEEDBACK IMPEDANCE: R_f=23 MΩ.

The "motherboard" onto which 25 "RAL108B" hybrids are mounted, to make a 25 channel pre-amp board, houses the peripheral electronics required for each hybrid. It incorporates a D.C. coupled bias supply for the strip detector, A.C. coupled test input and an A.C. coupled pre-amplifier signal input and output. Detector to pre-amplifier connection is through a 34-way ribbon cable of minimal length to minimise capacitance. The "RAL 108B" hybrid and motherboard is illustrated in FIGURE (3.7) for one channel. The output signal 100% $\rightarrow$ 63% decay time is determined by R_fC_f and equals about 50 μs.

3.6 Walk Independent Timing Resolution of the Detector and Amplifying System.

The detector and pre-amp do not constitute the whole of the timing circuit. Further shaping and amplification must be provided to best suit the application. The type of shaping constants applied are dependent on whether good timing or good energy resolution is the primary aim, since the two are generally mutually exclusive. If energy resolution is the prime consideration, then a large integration time is used to integrate over most of the pre-amp output pulse, so that the integrated pulse has a better signal:noise ratio and therefore better resolution. The optimum integration time is determined by the pre-amp output

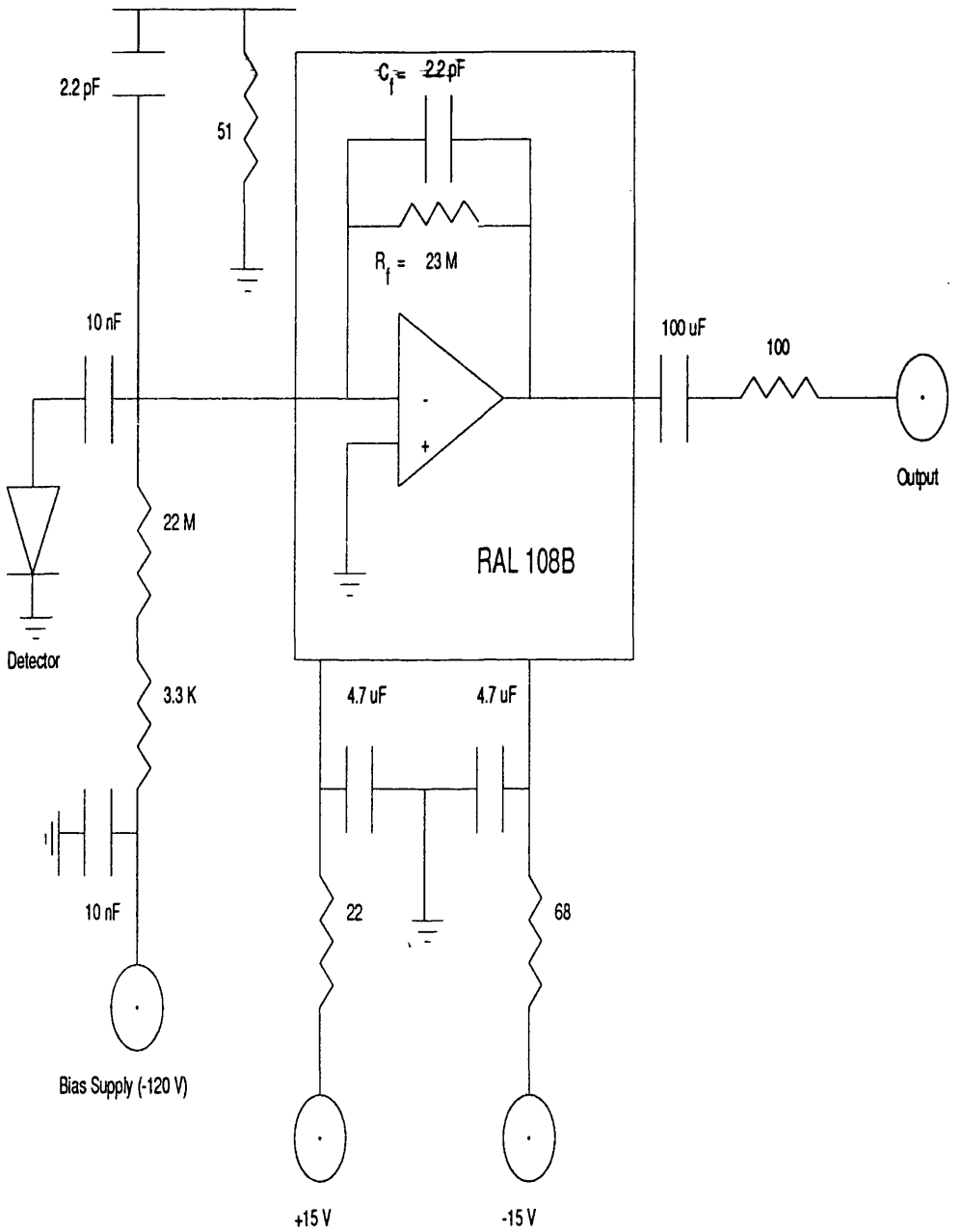

Figure 3.7: *The RAL108B Hybrid and Motherboard; One Channel.*

signal decay time and the signal:noise ratio. Normally it is much larger than the risetime of the pre-amp output pulse, so that this kind of amplification is undesirable for fast timing applications.

For good timing, a small amount of integration is desirable, to smooth over the high frequency noise components on the rising edge of the pre-amp output pulse, so that jitter, in the discriminator that the output pulse is fed into, is minimised. The upper limit however is determined by the risetime of the pulse, which must be maintained since the magnitude of the jitter varies inversely with the gradient of the rising edge of the pulse. This compromise results in a reduced signal:noise ratio, when compared with the longer integration times discussed above, but a minimal loss of timing resolution due to jitter. Differentiation is also applied at this stage to clip the exponential tail pulse of the pre-amp output pulse. This reduces low frequency noise and in cases where the rate is large, reduces pulse pile-up.

In the following tests, the signal:noise ratio and timing resolution of the strip detector and its amplifying system are investigated, to ascertain whether this strip detector is a suitable choice for a focal-plane detector. The best amplifier shaping constants for the strip detector are therefore first determined for optimum timing and signal:noise ratio.

The source used in the tests is ^{207}Bi. The decay scheme is detailed in FIGURE (2.5). BaF_2 scintillator, coupled to a photomutiplier, was chosen for a stop detector in the timing tests. Being an efficient γ detector, the two step emission process of the source and the probability of internal conversion at either of these stages can be exploited to give electron γ coincidences for a range of pulse heights recorded in the strip detector. In this way, the timing resolution of the

detector for minimum-ionising 100 MeV electrons can be compared with the timing resolution obtained for electrons which deposit larger amounts of energy in the strip detector and the effect of the signal:noise ratio on timing resolution can be estimated for the strip detector and amplifying system. This is useful for determining how good the strip detector and amplifying system timing resolution is, with minimum-ionising electrons, in a typical noise environment, relative to how good the timing resolution could be, if a better signal:noise ratio could be attained. The optimum timing resolution for the strip detector system will also therefore be extrapolated from the results.

3.6.1 Procedure

The source is uncollimated and positioned 8 mm from the detector. The detector and pre-amp were connected together with a 100 mm long ribbon cable. This was all mounted in an 1mm-thick-Al box with dimensions 27 mm x 420 mm x 210 mm, with a 0.1 mm thick x 50mm x 50 mm thin window in the lid, directly above the strip detector. This box was used to keep the strip detector light tight and to reduce radiative pick-up in the circuitry. To accomplish this effectively, the box dimensions were kept small. NIM output cabling was used rather than the more conventional twisted pair cabling. It was observed to be less susceptible to radiative pick-up.

The pre-amp output was fed into a FAN IN, FAN OUT. Although the 100 Ω pre-amp output, connected to a 50 Ω cable and a 50 Ω input at the FAN IN, FAN OUT, constitutes an impedance mismatch, any reflections consequently introduced were observed to be insignificant.

Two signals were output from the FAN IN, FAN OUT. One was used to

record a pulse height spectrum of the source in the strip detector; the other to trigger a logic pulse in a discriminator for a coincidence test. The electronic setups for recording these spectra were based on NIM and CAMAC units. The CAMAC units interface with a VME computer. The data were read out by the computer using the ACQU system, [10] and transferred to a VAX for display. In this way, multiparameter graphs can be formed from the data collected. The set-up is shown in FIGURE (3.8). The reasons for this particular layout are as follows;

(1) To study the pulse height spectrum, the pre-amp output was fed into a CAMAC peak-sensing ADC (Analogue to Digital Convertor) via a shaping amplifier. The shaping constant giving the best energy resolution was experimentally found to be 0.5 μs.

(2) To study the timing, the strip detector signals were fed into an LED (Leading Edge Discriminator), via a fast timing filter amplifier (TFA). The TFA integration time (= 10 ns) was adjusted to remove high frequency noise, without affecting the risetime of the leading edge. The differentiation time (= 200 ns) was chosen to be the minimum value consistent with a low loss of gain. The LED output pulse was then used to trigger a gate which was used as an interrupt, to initialize data recording in the computer. The gate was self-latched and then reset by the computer after the readout of each event was completed. The gate output was shaped and fanned out to provide triggers for the necessary CAMAC/NIM units. One output was used as a start signal for a CAMAC TDC (Time to Digital Convertor.). To avoid walk due to the various pulse heights from the BaF_2, the stop signal for the TDC was provided by a CFD (Constant Fraction Discriminator), triggered by the fast component of the output pulse

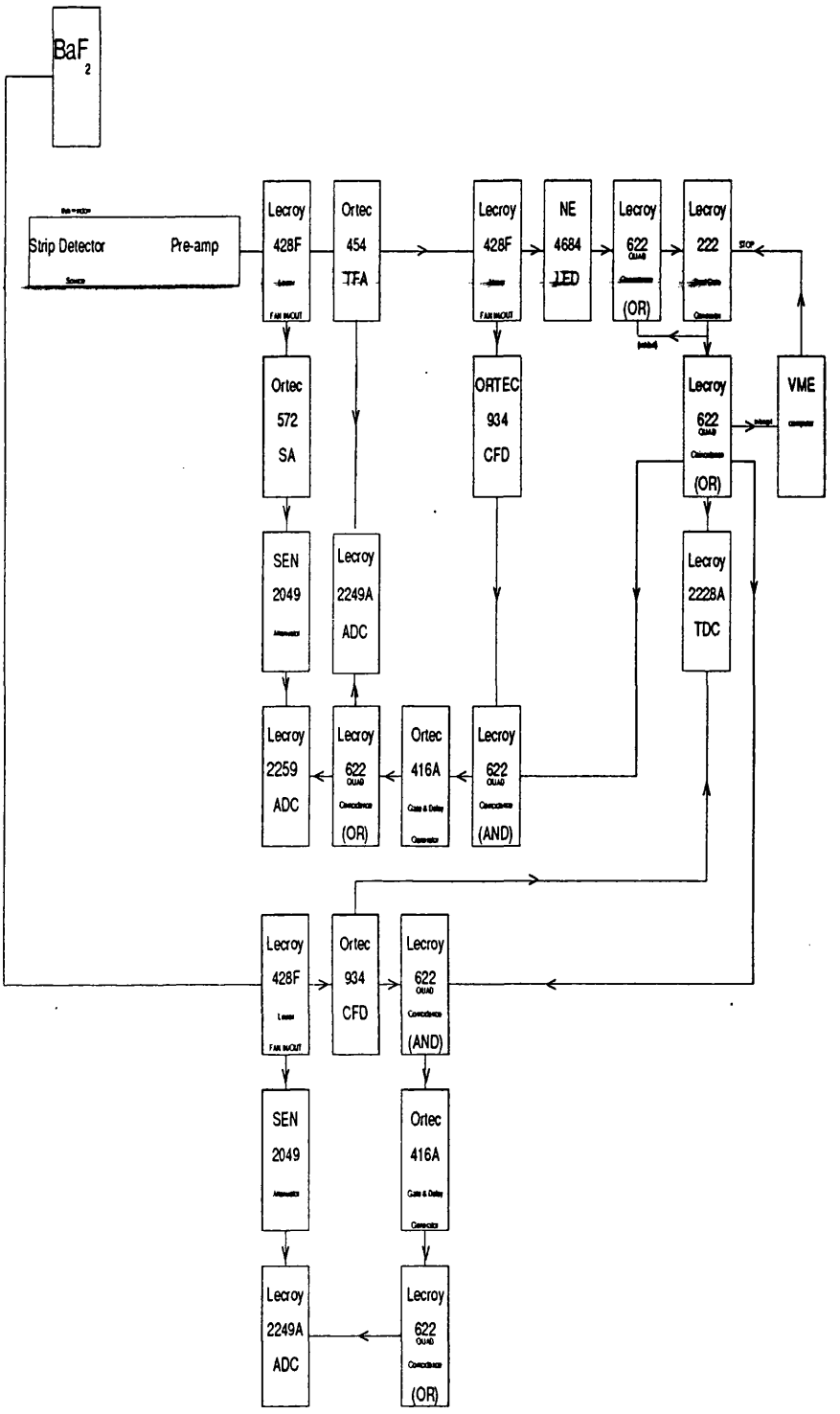

Figure 3.8: *Circuit Diagram for the Test Described in §3.6.1.*

of the BaF_2 scintillator. The BaF_2 was placed directly above the thin window in the box and was thick enough to fully absorb most of of the 570 keV γ's and also some of the 1.063 MeV γ's. Triggering of the CFD on the jagged edges of the signal was alleviated by setting the CFD output pulse width to 1 μs. The scintillator/photomultiplier and discriminator combined were expected to provide subnanosecond timing and therefore contribute a negligible amount to the width of the co-incidence time spectrum. However, this statement will be verified experimentally. The BaF_2 pulse height spectrum was also recorded by feeding the output from the photomutiplier directly into a charge sensitive ADC. The ADC gate pulse was 1 μs and was provided from a coincidence of the scintillator CFD and the trigger given by the strip detector. The scintillator CFD pulse was timed to follow the strip detector trigger. In this way, timing of the BaF_2 pulse was fixed relative to the ADC gate and did not depend on the strip detector LED output, which is prone to sizeable walk. The same principle was applied to provide a steady gate pulse for a charge sensitive ADC which recorded the strip detector TFA output; the strip detector TFA output was fed into a CFD with a lower threshold than the LED. The ADC gate was supplied from a coincidence between the strip detector CFD and the trigger given by the strip detector LED, where the CFD pulse followed the trigger. The same gate pulse was used for the peak sensing ADC.

Corrections for walk in the strip detector LED were applied off-line using the formula, [16];

$$t_c = t - r\sqrt{(1 - \frac{a_o}{a})}, \tag{3.6}$$

where t_c is the walk-corrected trigger time,

t is the time recorded in the TDC,

r is the risetime of the signal,

a_o is the discriminator threshold,

and a is the amplitude of the pulse in the strip detector.

This formula gives a reasonable first order walk correction, although, it is better to vary the product $r.\sqrt{a_o}$ as an empirical parameter with values in the region of the true risetime and threshold, until the best result is obtained, [17].

It was found that the signal from the strip detector exhibited significant noise. The main causes of this noise were earth loops, impedance mismatches and radiative pick-up. Before proceeding therefore, methods of reducing noise were investigated. Most improvement resulted from;

(1) Fastening a large copper braid between the voltage supply for the pre-amp, the voltage supply for the photomutiplier, the oscilloscope and the NIM and CAMAC crates.

(2) Ensuring that each input and output was correctly terminated with 50 Ω, to match the NIM cabling used in all connections between the units.

(3) Use of a filter on the mains power supply lines.

(4) A layer of Al radiative shielding and a toroid on the pre-amp D.C. power supply.

(5) Keeping cables short.

Reduction of such noise is very time consuming and since every noise environment is different, the particular methods employed in one environment cannot be guaranteed to work as effectively in another. The present set-up was tested for noise in several environments. The methods employed here for noise

reduction were sufficient to remove the major contributions to noise, independent of environment. There still remained however, several minor contributions to noise. No further attempt was made to obtain further noise reduction in order to give a realistic picture of the signal:noise ratio that can be attained with a reasonable effort. It may be that considerable work will be needed to reduce the noise in the environment near the tagging spectrometer in Mainz.

3.6.2 Results

The internal conversion electrons of the 570 keV de-excitation have, as seen in FIGURE (3.6), a mean range in silicon of 660 μm for the k-conversion electrons and 760 μm for the l-conversion. These electrons have a differential energy loss higher than that of a minimum-ionising particle. Further, the average pathlength is greater than detector thickness due to non-normal incidence from the uncollimated source and scattering. Using the Gaussian approximation for multiple Coulomb scattering for relativistic electrons, [18];

$$\theta \simeq \frac{13.6 \times t}{E \times \beta} \tag{3.7}$$

where θ is the RMS scattering angle in radians,

t is the thickness in radiation lengths,

E is the energy of the electron in MeV

and β is the ratio of the particle velocity to the speed of light;

a 481.7 keV electron has a mean scattering angle of 13° in the detector. For a 481.7 keV electron to be stopped in the detector, the required deviation of an electron from the 'straight through' trajectory is 41° to the normal of the detector surface. This means that about half of the electrons incident on the detector surface at an angle greater than 28° to the normal are stopped, if

scattering adds to the total deviation in the electron trajectory away from the normal.

The conversion electrons of the 1063 keV transition are less easily categorised. They have a range in the detector of $\sim$ 1650 μm for a 975.1 keV k-conversion electron. FIGURE(3.5) indicates that any electron that exits the detector with an energy of more than $\sim$700 keV, can be regarded as minimum-ionising. With dE/dX = 360 eV/μm at 1 Mev , the 1.063 MeV γ conversion electrons, travelling normal to the detector surface, can therefore be expected to lose an average of 180 keV within the detector thickness, exiting with an energy of $\sim$795 keV for the k-conversion electrons and $\sim$868 keV for l-conversion electrons. However, when scattering and non-normal incidence are considered, there is a high probability of these electrons depositing more than 180 keV, with some of them stopping. From EQUATION (3.7), a 975 keV electron has a mean scattering angle of 4^o. Therefore the 1.063 MeV conversion electrons will have a deposited energy distribution in the strip detector which mainly reflects the probability distribution of non-normal incident angles. The most probable incident angle is determined by source to detector geometry. The detector strip width limits the incident angle to a maximum of 14^o to the normal in the relevant plane. The detector strip length limits the incident angles in the relevant plane to 75 ^{o} at most. Another factor in the strip detector pulse height spectrum, is the possibility of the electrons back-scattering out of the detector. There is a 30 % probability of backscatter in this thickness of silicon at this energy. This is particularly apparent below 200 keV, where the pulse height decreases more slowly to zero than would be expected, if the sole contribution to the pulse height at this point was minimum-ionising electrons, which pass straight through the detector.

The features of the ^{207}Bi pulse height spectrum in the strip detector are observed in FIGURE (3.9) (solid line). This spectrum was recorded, via a shaping amplifier, in the peak-sensing ADC shown in FIGURE (3.8). The k and l conversion electron peaks of the 570 keV and 1.063 MeV transitions are clearly resolved. The 570 keV peaks ride on the energy distribution curve produced by the higher energy electrons which do not stop in the detector. The area under the k and l full energy peaks of the 1.063 MeV conversion electrons, relative to the area under the continuous distribution (even allowing for the contribution to the lower energy end from back-scattering) is indicative of how improbable large pathlengths in the detector are.

The calibration, which relates the channel number to the energy deposited in keV, is superimposed on the spectrum. This was obtained by plotting the known energies from the source listed in FIGURE (2.5), against the corresponding channels where the full energy peaks are observed. From the calibration, the most probable energy deposited by minimum-ionising electrons is 209 keV.

The FWHM (Full Width Half Maximum) of the peaks are listed in FIGURE (3.9). The width of these peaks are a good indication of the energy resolution of the detector and the associated signal electronics for electrons at this energy, since conversion electrons are intrinsically monoenergetic.

The dashed line in FIGURE (3.9) shows the noise spectrum, superimposed on the signal pulse height spectrum. This was recorded in a separate test, where the only difference from the set-up outlined in §3.6.1 was the removal of the source and lowering of the strip detector LED to $\sim$140 keV.

There is no well defined boundary between signals and noise in the pulse height spectrum. However, there is a valley between the noise and the signal

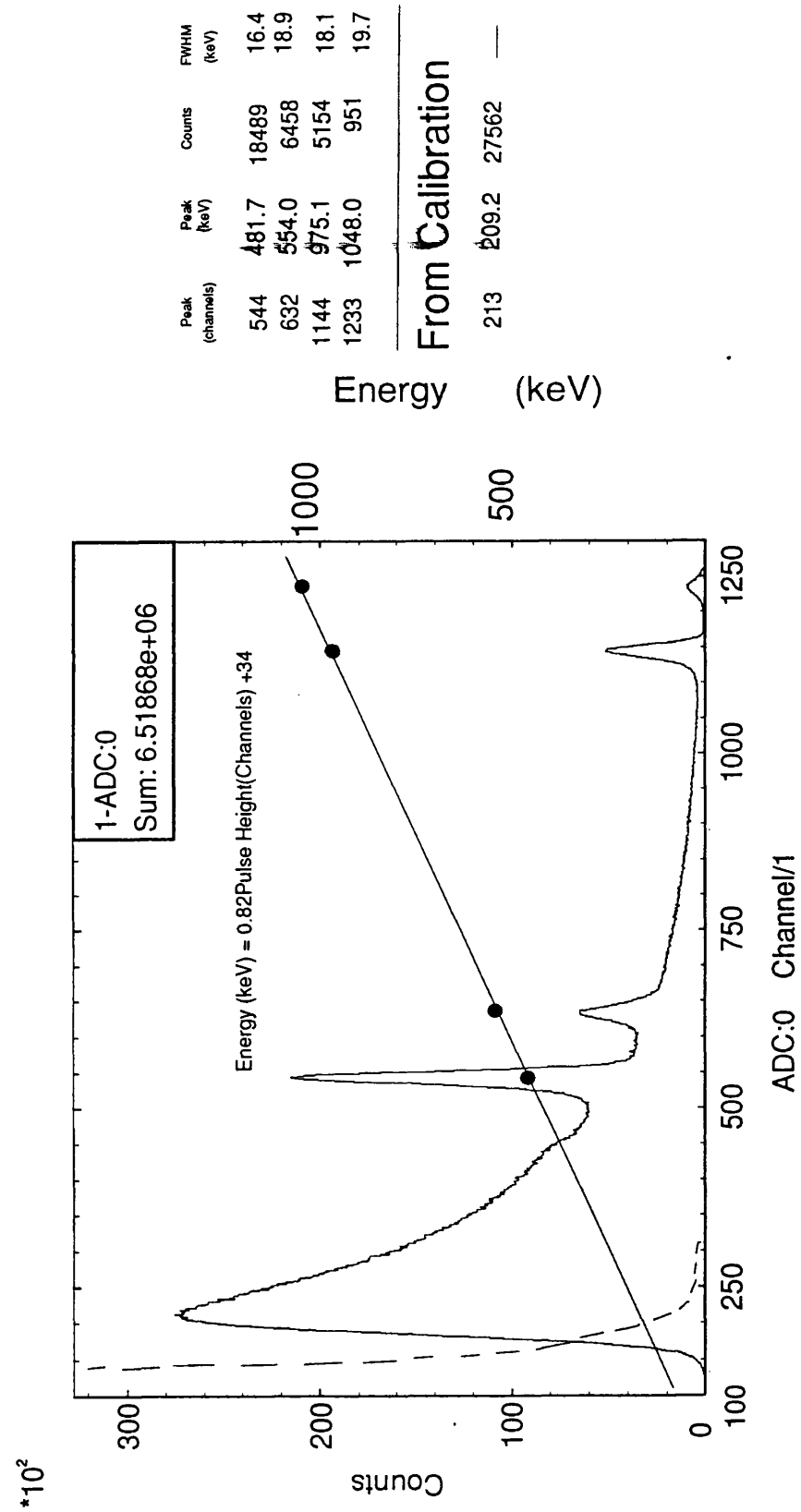

Figure 3.9: *The Strip Detector Pulse Height Spectrum; Recorded via the Shaping Amp.*

spectra. The energy at which this valley reaches its lowest point is ~180 keV, where the noise count rate equals the signal count rate. The signal:noise ratio observed in the TFA output, when fed into a charge sensitive ADC, was also examined, since the signal:noise ratio is degraded in a setup for good timing resolution. Very little difference was observed in the position of the valley, with a shift of ~10 keV, so any conclusions drawn for the shaping amplifier output could equally well apply to the TFA output. The discriminator was therefore set at ~180 keV, to cut out the largest amount of noise for the smallest loss of signals, so this valley is cut off in the signal pulse height spectrum. Below 180 keV, the noise spectrum, explored with an ORTEC 7450 Multichannel Analyzer, rises rapidly with decreasing energy, reaching a rate of $\leq$ 600 Hz at ~50 keV. In this test, the smallest and most frequent noise pulses were cut off with the multichannel analyzer's built-in discriminator, to reduce the analyzer dead time. Dead time was ~2% for this measurement. Above 180 keV, the noise spectrum decreases very quickly to near zero and does not contribute significantly to the observed pulse height spectra. The ^{207}Bi source count rate for this experiment was ~4 Hz. For a ^{207}Bi source, with a rate equal to the desired 1 MHz frequency/strip in the tagger focal-plane, the valley in the pulse height spectrum would occur below 50 keV. It can be shown, [19], that the energy deposited by a minimum ionising electron in a detector is Landau distributed, peaking at the most probable energy deposited by the electron in the detector. The integrated Landau distribution is shown in FIGURE (3.10) and can be used to predict the percentage of electrons which will deposit above a certain energy in the strip detector. The distribution is plotted in terms of probability P(ϕ), against ϕ;

$$\phi = \frac{E - E_{prob}}{W} \tag{3.8}$$

where E is the energy deposited in the strip detector (MeV),

W (= 8.71 x 10^{-3} MeV)is given in EQUATION (3.9)

and E_{prob} ($\sim$ 0.220 MeV) is the most probable energy deposited in the strip detector, given in EQUATION (3.10).

$$W = \frac{0.15Zz^2x}{\beta^2 A} \tag{3.9}$$

where z is the charge of the particle (units of e: = 1),

m_e is the particle mass (units of m_e: = 1),

Z is the Si atomic number (= 14),

A is the Si mass number (= 28.09 a.m.u.),

v is the particle velocity (units of c: $\sim$ 1),

β is electron velocity/the speed of light (= 0.9999871)

and x is the detector thickness (= 0.1165 gcm^{-2}).

$$E_{prob} = Wln(\frac{2m_e v^2 E_{max}}{I^2(1-\beta^2)}) \tag{3.10}$$

where E_{max} is the maximum energy deposited in the detector ($\sim$4W),

I is the Si ionisation potential (= 173 eV,[13])

and all other variables are as in EQUATION (3.9).

From FIGURE(3.10), $\ll$ 1% of electrons deposit an energy less than -3 W of the most probable energy. i.e. $\ll$ 1% deposit < 188 keV. It can be concluded that the signal:noise ratio is adequate to separate the $\sim$220 keV minimum-ionising peak, that would be obtained from a tagger electron of 100 MeV, from the noise. The shaped timing amplifier signal could therefore be operated simply with a discriminator to filter out noise, while still retaining negligible loss of genuine signals, provided that all extraneous noise in the vicinity of the focal-plane can be similarly quashed and background is negligible. The co-incidence

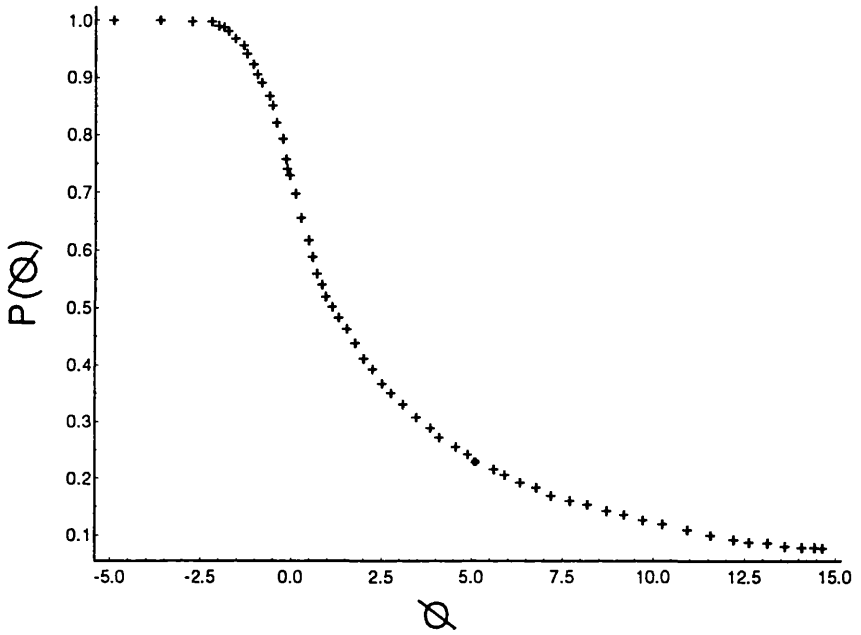

Figure 3.10: *Integrated Probability of Finding An Energy Fluctuation Greater Than A Given value (ϕ is in Units of W.)*

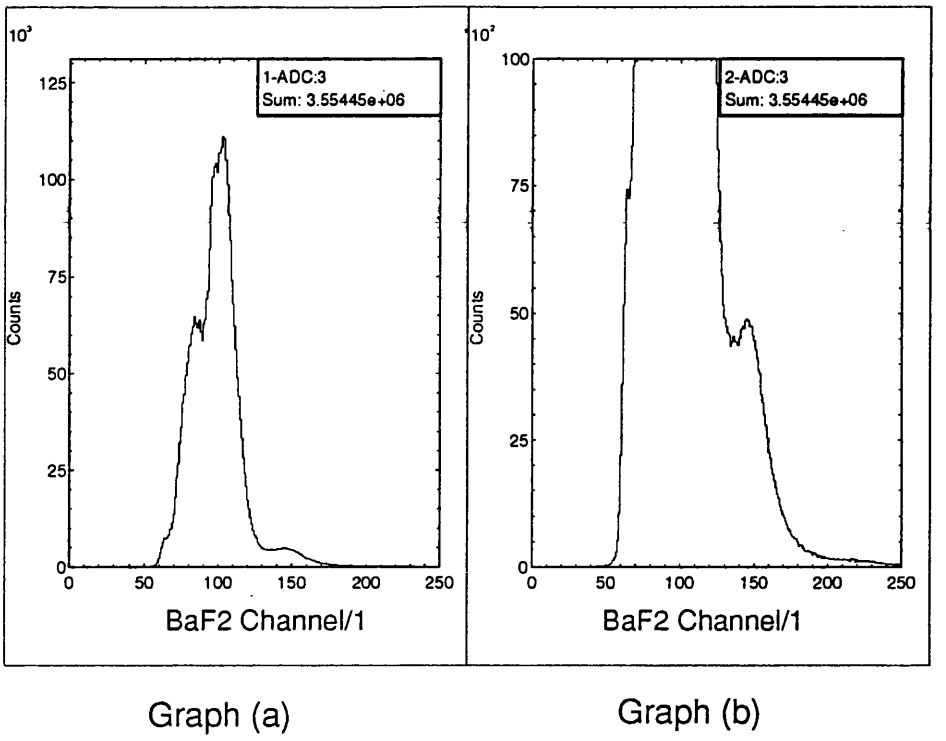

Figure 3.11: *Pulse Height Spectrum in BaF_2; Gated on Coincident Pulses.*

mode employed to enhance the performance of the present focal-plane system will therefore not be required.

FIGURE (3.11) displays the energy spectrum of BaF_2. The peaks from the two prominent γ emissions of the source are clearly observed. Graph (a) highlights the 570 keV γ peak observed at channel 103, while Graph (b) highlights the 1.063 MeV γ at channel 145. The ratio of these peaks is not consistent with the relative γ intensities listed in FIGURE (2.1). The 1.063 MeV γ is suppressed. There are two main reasons for the appearance of this spectrum. One is that the 1.063 MeV γ's have an attenuation length much larger than that of the BaF_2 scintillator thickness, so that the majority of 1.063 MeV γ's do not contribute to the full energy peak. The attenuation length is shorter for the 570 keV γ's, for which the full energy peak fraction is larger. This rides on

the Compton distribution from the 1.063 MeV γ's. The lower part of the pulse height distribution is cut off by the CFD.

The other reason for the appearance of the spectrum is that it is gated by the strip detector pulses, as described above. The decay scheme constrains a coincidence to be formed either when a 570 keV γ cascades with an internally converted electron from the 1.063 MeV γ, or when a 1.063 MeV γ cascades with an internally converted electron from a 570 keV γ. The ratio of the probabilities of these coincidences is therefore given by the ratio of their internal conversion coefficients. Thus a 570 keV γ in coincidence with a 1.063 MeV internal conversion is $\sim$6 times more likely than a 1.063 MeV γ in coincidence with a 570 keV internal conversion.

FIGURE(3.12) shows the pulse height in the BaF_2 against the pulse height in the strip detector. GRAPH (a) highlights the 1.063 MeV γ peak in the BaF_2 and Graph(b) highlights the 570 keV γ peak. These graphs are a direct reflection of the possible paths to co-incidence, in accordance with the decay scheme. Consequently, this indicates that most of the coincidences are concentrated around the 570 keV γ-peak of the BaF_2 and at the low energy end in the strip detector, below the 570 keV conversion electron peaks. In REGION (A), the coincidences are due to those γ's which have not been fully absorbed in BaF_2. In the BaF_2 spectrum (FIGURE (3.11)), counts in this region mainly arise from the 1.063MeV γ's. However in the 2D spectrum shown here, the higher probability of higher energy γ's depositing less than their full energy, is counterbalanced by the higher probability of co-incidence associated with the 1MeV electron/570 keV γ cascade. Therefore all features of the strip detector spectrum are present.

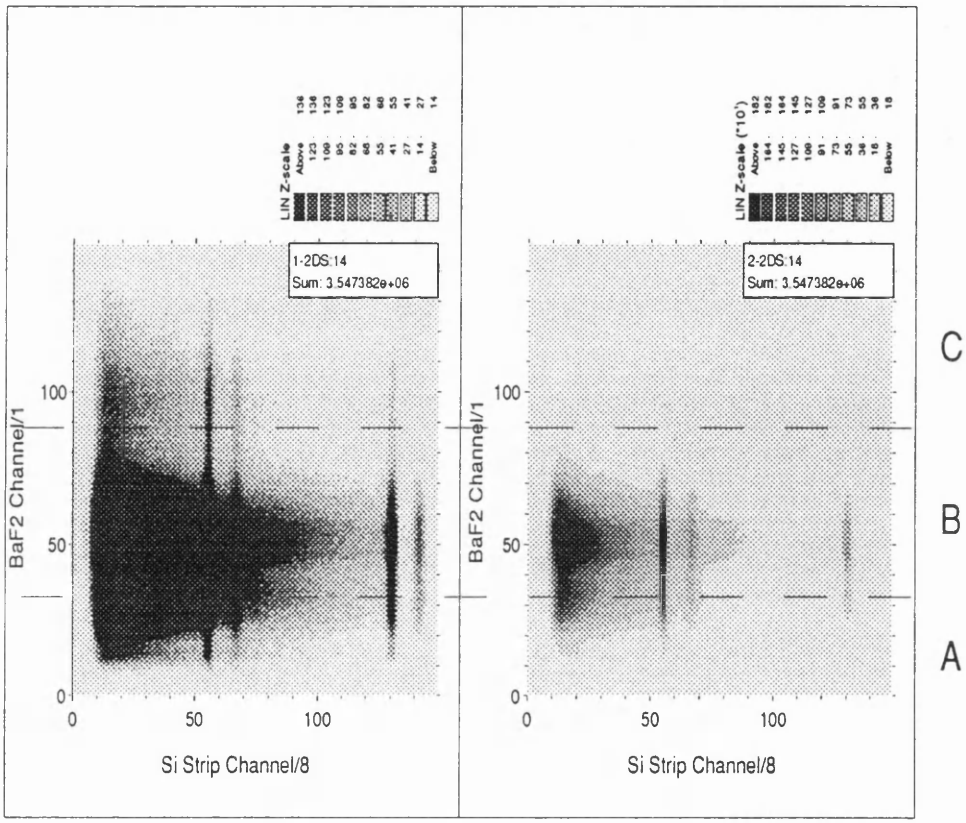

Figure 3.12: *Pulse Height in BaF_2 vs Pulse Height in the Strip Detector*

In REGION (B), all features of the strip detector spectrum are again evident. The 570keV conversion electron peak in the strip detector, although constrained to coincide with a 1.063 Mev γ, is seen within this ridge because the 570 keV γ rides on the energy distribution curve of the higher energy γ's.

In REGION (C) the strip detector spectrum shows almost no 1.063 MeV conversion electron peak. The small peak which is observed is due to random coincidences. This region also has relatively fewer low pulse height events, where the electrons have passed straight through the strip detector. The only contributions to the continuum under the peaks in the strip detector in this region, are those 570 keV conversion electrons which have not stopped in the detector, back-scattered electrons and background

Due to the 2 ns risetime of the BaF_2 output pulses and because a CFD is used, it is expected that walk with respect to the BaF_2 pulse height is small and that it contributes little to the overall timing resolution. To obtain a quantatitive measure of the extent of walk in the BaF_2 and how the system timing resolution varies with its pulse height, the TDC spectrum is examined first for the 570 keV region in the BaF_2 and then for the 1.063 MeV region in the BaF_2. In the lower pulse height region, the constraints to the possible paths to coincidence mean that the coincident electrons mostly have an energy of $\sim$ 1 MeV. It was observed in FIGURE (3.9) that the majority of 1.063 MeV conversion electrons in the strip detector are minimum-ionising and that the smaller pulses they induce are more affected by noise. Consequently, the TDC spectrum for this cut is rather broad. For the 1.063 MeV region in BaF_2, almost all of the coincident electrons have $\sim$500 keV energy and give a larger pulse in the silicon detector. Therefore the TDC spectrum is narrower.

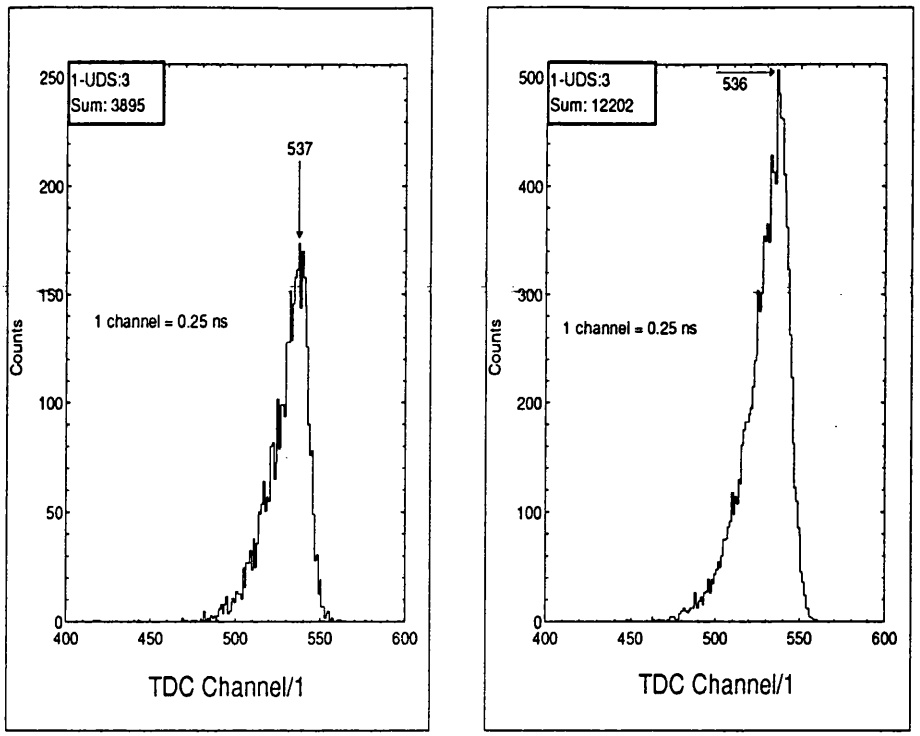

Graph (a): 1 MeV Peak

Graph (b): 570 keV Peak

Figure 3.13: *Si- BaF_2 Time Difference Spectra, for 500-570 keV in the Strip Detector.*

To avoid any dependence of the timing resolution on the constraints of the decay scheme, events were restricted to a narrow pulse height range in the strip detector. An interval of 500→570 keV was chosen in the strip detector pulse height spectrum since it contained a reasonable number of pulses due to 570 keV conversion electrons and 1.063 MeV conversion electrons. FIGURE (3.13) shows the results (GRAPH (a)), for the 1.063 MeV cut and GRAPH (b) for the 570 keV cut in the BaF_2 detector. Both peak at channel ~537, showing that there is little residual walk in the BaF_2 CFD and both have a FWHM of 20 ns, showing that the overall timing resolution is independent of the BaF_2 pulse height.

FIGURE (3.14) shows pulse height in the strip detector against BaF_2-Si time difference; GRAPH (a) highlights the 1.063 MeV conversion electron full

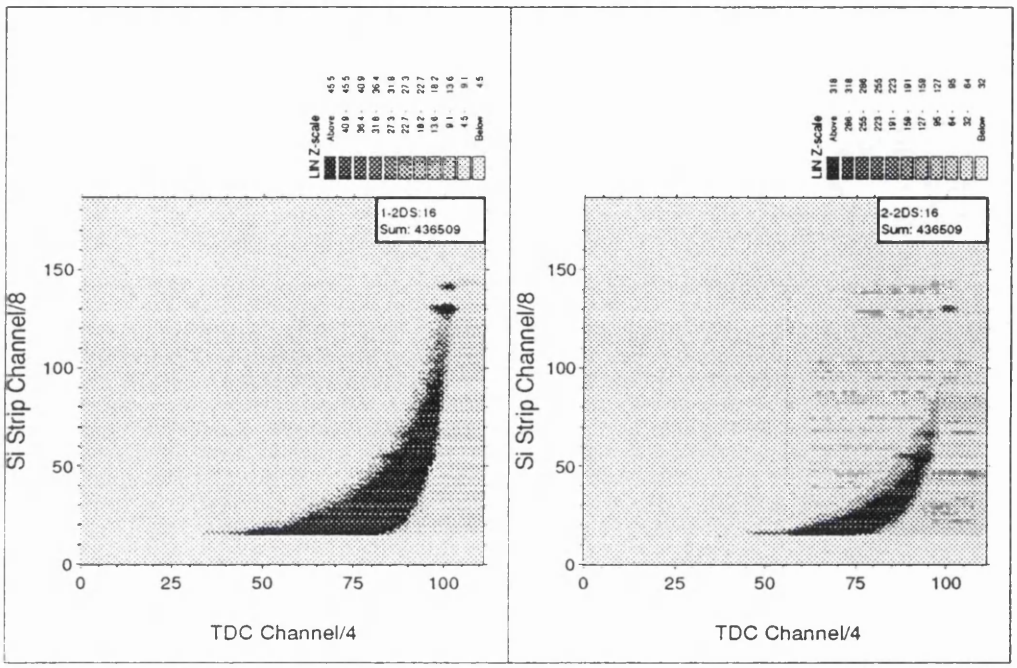

Figure 3.14: *Strip Detector Pulse Height vs Si-BaF_2 Time Difference; No Walk Corrections*

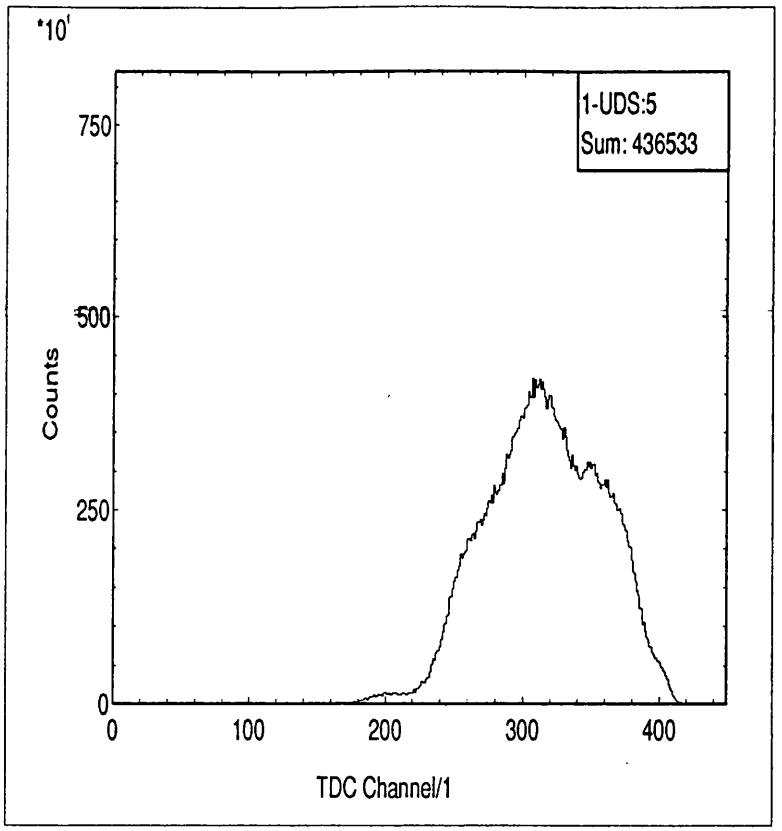

Figure 3.15: *Si-BaF_2 Time Difference: 1 channel= 0.25 ns*

energy peak, while GRAPH (b) highlights the lower energy electrons. No walk corrections have been applied to the strip detector LED output at this stage. The smallest strip detector pulses are most affected by walk, as expected.

FIGURE (3.15) shows the TDC spectrum, covering the whole range of possible coincidences. With a Si start, events in the higher TDC channels, without applying walk corrections, imply larger pulses from the strip detector, since these trigger the LED relatively early. The structure evident in FIGURE (3.14) arises because of walk with strip detector pulse height and the structure of the strip detector spectrum in coincidence with the BaF_2. See FIGURE (3.12). The timing resolution obtained with electrons which do not stop and are close to minimum-ionising in the strip detector, therefore dominate the Si-BaF_2 time difference spectrum. This is because, from FIGURE (3.12), coincidences involv-

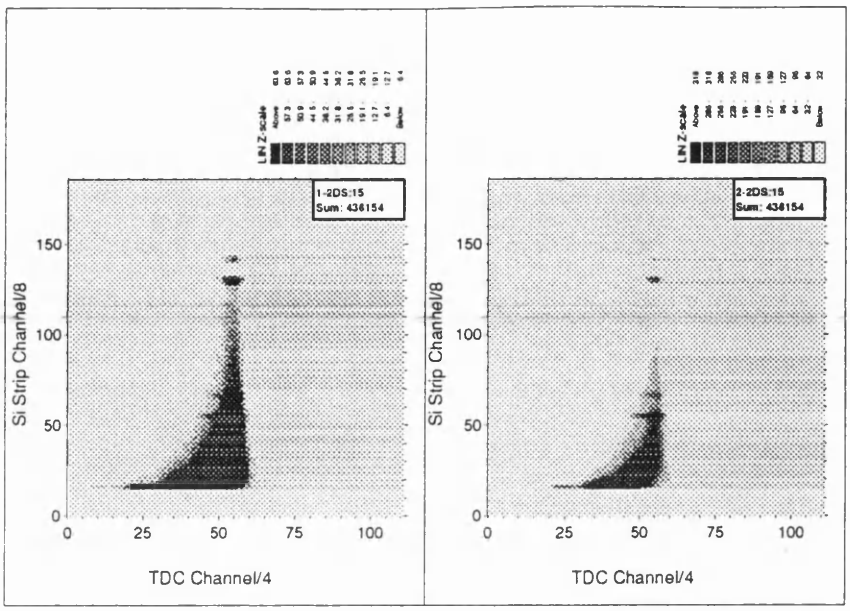

Graph (a) Graph (b)

Figure 3.16: *Strip Detector Pulse Height vs Si-BaF_2 Time Difference; Walk Corrections Employed.*

ing such electrons in the strip detector are the most probable.

FIGURE (3.16) shows the same spectrum as FIGURE (3.15), but with walk corrections applied to the LED using EQUATION (3.6). The walk correction has been applied with r = 250 and a_o = 80. These values were experimentally determined to show the best overall walk correction. However, although this is observed to be effective at higher energies, walk below ~400 keV is still evident. This is due to inadequacies in the simple walk correction of EQUATION (3.6). Attempts to improve the correction for small pulse heights, by adjusting r and a_o, always resulted in a poorer correction at higher pulse heights, which became overcompensated.

To obtain results for the walk independent timing resolution of the strip detector, walk corrected TDC spectra were made for a series of narrow cuts on

Graph	Cut (keV)	FWHM (ns)	Peak Shift (ns)
17a	223.1 → 224.7	13.8	0.0
17b	231.3 → 232.9	14.3	1.0
17c	239.5 → 241.1	12.0	5.3
17d	247.7 → 249.4	9.0	5.5
17e	258.4 → 260.1	7.5	7.3
18a	321.7 → 325.8	7.3	10.8
18b	403.9 → 408.0	5.5	13.0
18c	469.7 → 473.8	4.8	13.8
18d	551.9 → 556.0	4.0	14.0
18e	971.9→ 976.0	3.3	14.0
18f	1043 → 1052	3.0	13.8

Table 3.1: *Timing Resolution Obtained for a Series of Cuts in the Strip Detector Spectrum*

strip detector pulse height and are shown in FIGURES (3.17) and (3.18). The width of these cuts was taken to be 2 channels at low pulse heights. This was observed from FIGURE (3.16) to correspond to $\leq$0.2 ns walk contribution for pulse heights between 225 keV and 300 keV. Slightly wider cuts were used at higher energies, where the walk correction worked better, to improve statistics at pulse heights with lower count rates.

TABLE (3.1) lists the relative peak position and the peak width (FWHM), for each of the cuts shown in GRAPHS (3.17a) → (3.18f). The peak widths are an indication of the resolution expected, if a CFD were used.

By plotting the FWHM of the peak width in TABLE (3.1) against the average energy of the cuts, a graph relating the walk independent resolution of the strip detector and its amplifying system, to the energy deposited in the

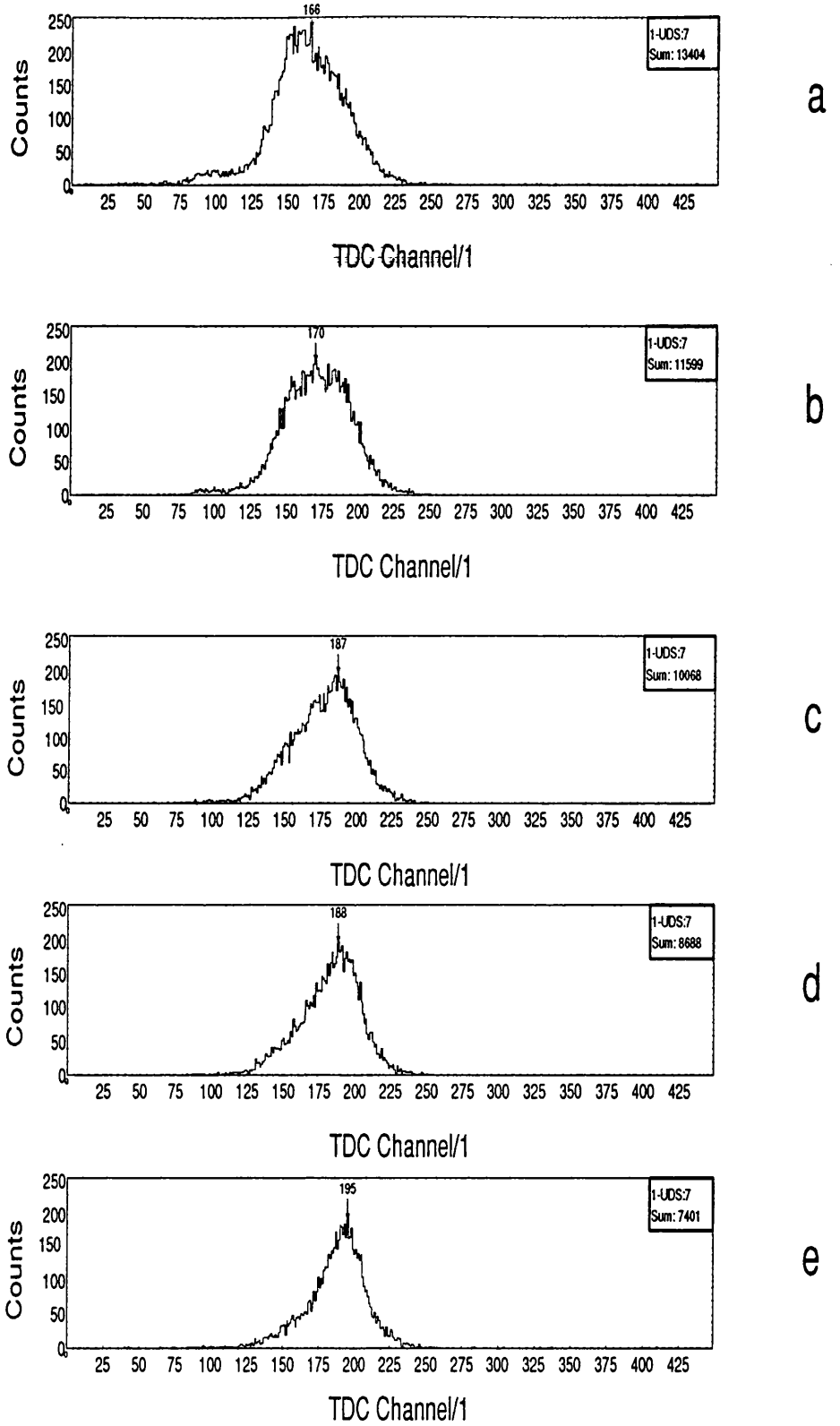

Figure 3.17: *Co-incidence Spectra, Cut At Various Points In The Strip Detector Spectrum: 1 Channel=0.25 ns.*

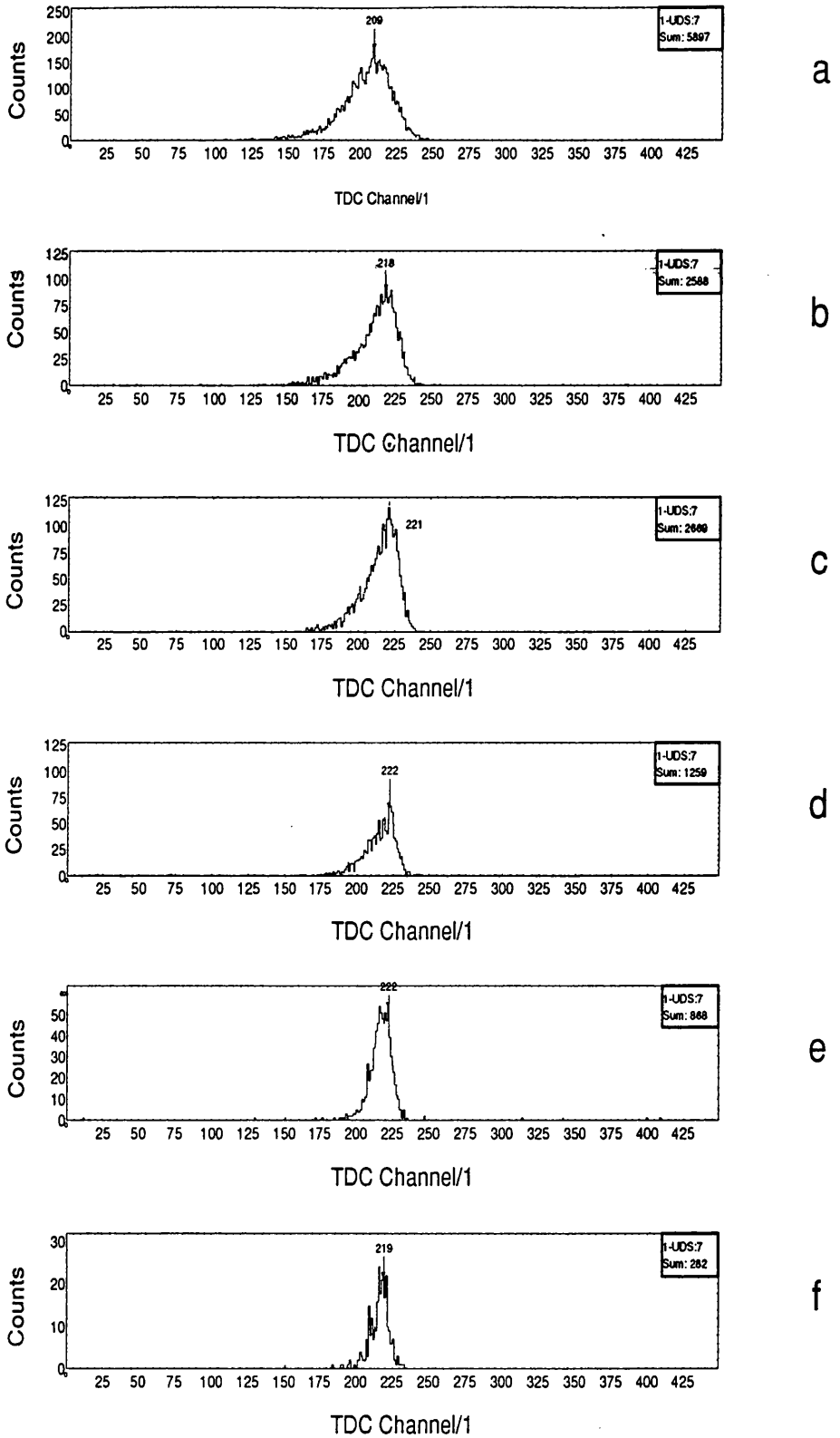

Figure 3.18: *Co-incidence Spectra, Cut At Various Points In The Strip Detector Spectrum: 1 Channel=0.25 ns.*

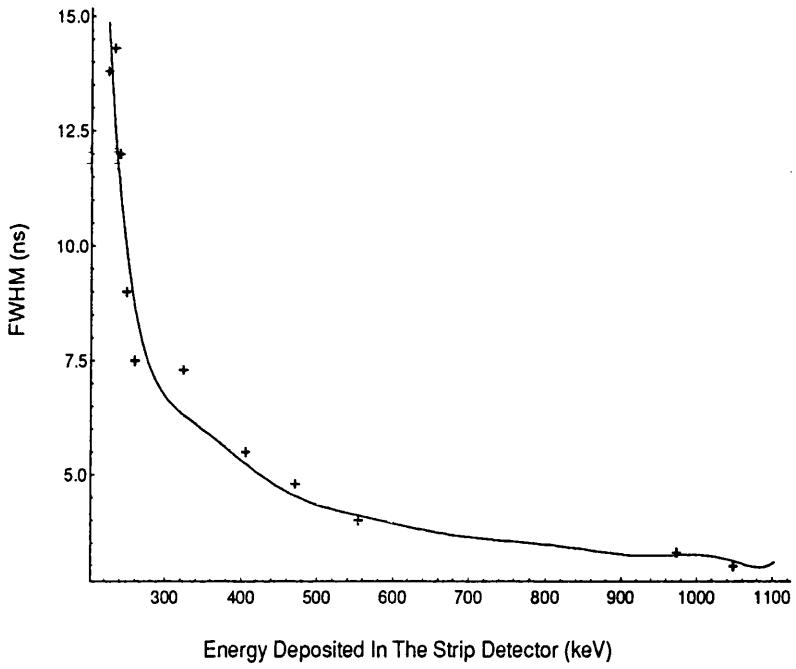

Figure 3.19: *Time Resolution vs Pulse Height in the Strip Detector.*

strip detector can be drawn. This is illustrated in FIGURE (3.19). The solid line is a polynomial fit to the data points.

3.7 Timing Resolution of the System with Improved Signal:Noise

The results obtained in the previous section for the timing resolution of the system could be reproduced relatively easily. However, it is useful to know quantatively how much of an improvement in timing resolution can be gained by reducing the noise as much as possible.

3.7.1 Procedure

The set-up used to record the pulse height spectrum from the strip detector is shown in FIGURE (3.20), while FIGURE (3.21) shows the timing circuit. This was largely similar to the set-up of §3.6. An ORTEC 7450 Multichannel Analyzer (MCA) was used instead of a CAMAC system and a transformer was placed between the output of the NIM system and the MCA, to reduce the noise introduced into the NIM system by the analyzer. The specifications for the transformer were 100 ns risetime, 8 μs fall time and a gain of 0.6. The TDC was replaced by a NIM Time To Amplitude Convertor (TAC). The start for the TAC was provided by a plastic scintillator, with dimensions 20 mm x 20 mm x 2mm thick, coupled to a small photomultiplier by a fish-tailed light-guide. The plastic scintillator was placed parallel to the strip detector surface and the scintillator surface centred on the middle of the detector surface. The dimensions of the scintillator were large enough to record any electron which passed through the strip detector with enough energy to trigger the scintillator discriminator. A scintillator of this thickness is an efficient electron detector, but has no significant contribution from the source γ's in its pulse height spectrum. The risetime of the scintillator pulses was $\sim$2 ns. This meant that using an LED did not contribute significantly to the overall timing resolution. The LED threshold was set just above the noise level, to minimise walk and retain most of the possible coincidences. The TAC stop came from the strip detector. The CFD was used on the strip detector, instead of an LED, to give walk free timing.

The source to detector perpendicular distance was 12 mm and the source was positioned at the centre of the strip. By sandwiching the strip detector between the source and the scintillator, the only coincidences which can be

recorded correspond to those electrons that exit the strip detector with enough energy to produce a signal in the scintillator above the LED threshold. The average energy deposited in the strip detector at each recorded coincidence is therefore similar to the 230 keV average energy that a minimum ionising 100 $\rightarrow$ 800 MeV tagger electron deposits in the strip detector.

3.7.2 Results

Optimising the signal:noise ratio was a trial and error process, involving replacement of each cable and terminator used in the experiment one at a time, to ensure that none were defective; systematic removal of each NIM unit from the NIM crate, to isolate the sources of the remaining noise and placing torroids between various other points not already containing one. Most significantly a 2.5 cm diameter toroid, placed between the pre-amp output and the TFA input, removed a large part of the radiative pick-up. To eliminate earth loops, all units were linked together with copper braid. The noise was reduced from the 180 keV observed in the previous section, to 100 keV. The noise spectrum was observed to decease very sharply in count rate towards this value. Above 100 keV, the noise spectrum slowly tailed off and was insignificant. The CFD threshold was therefore set just above 100 keV. There was no clear distinction between signals and noise, since the spectrum extended below 100 keV. A small fraction of detector output pulses, produced by the source, were therefore cut off. However, as explained in §3.6, an insignificant loss of signals would be observed with this threshold for electrons recorded in the tagger focal-plane.

The ^{207}Bi energy spectrum is shown for the strip detector gated on a coincidence pulse obtained from the two discriminator signals (FIGURE (3.22).

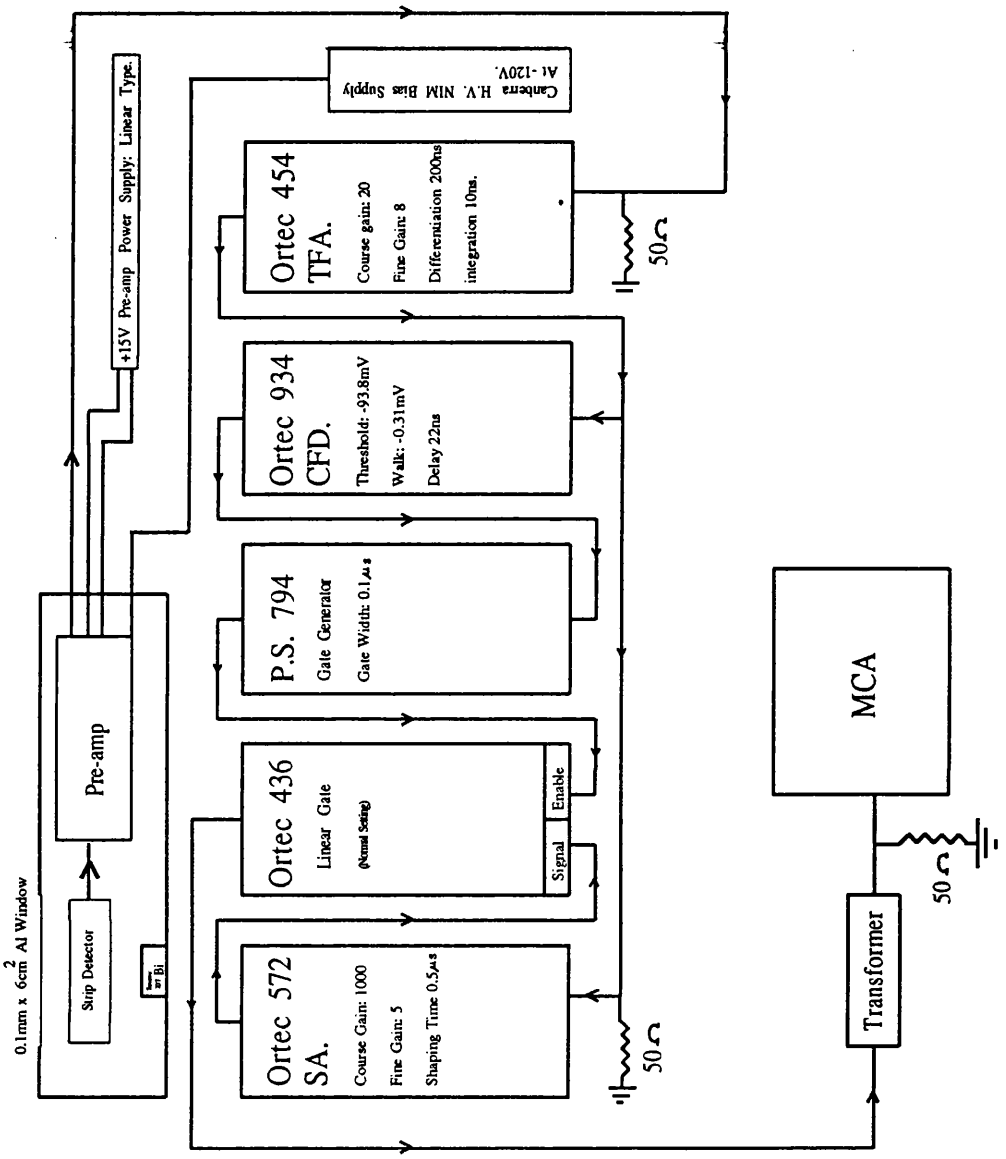

Figure 3.20: *Circuit Diagram Detailing Recording of the* ^{207} *Bi Energy Spectrum.*

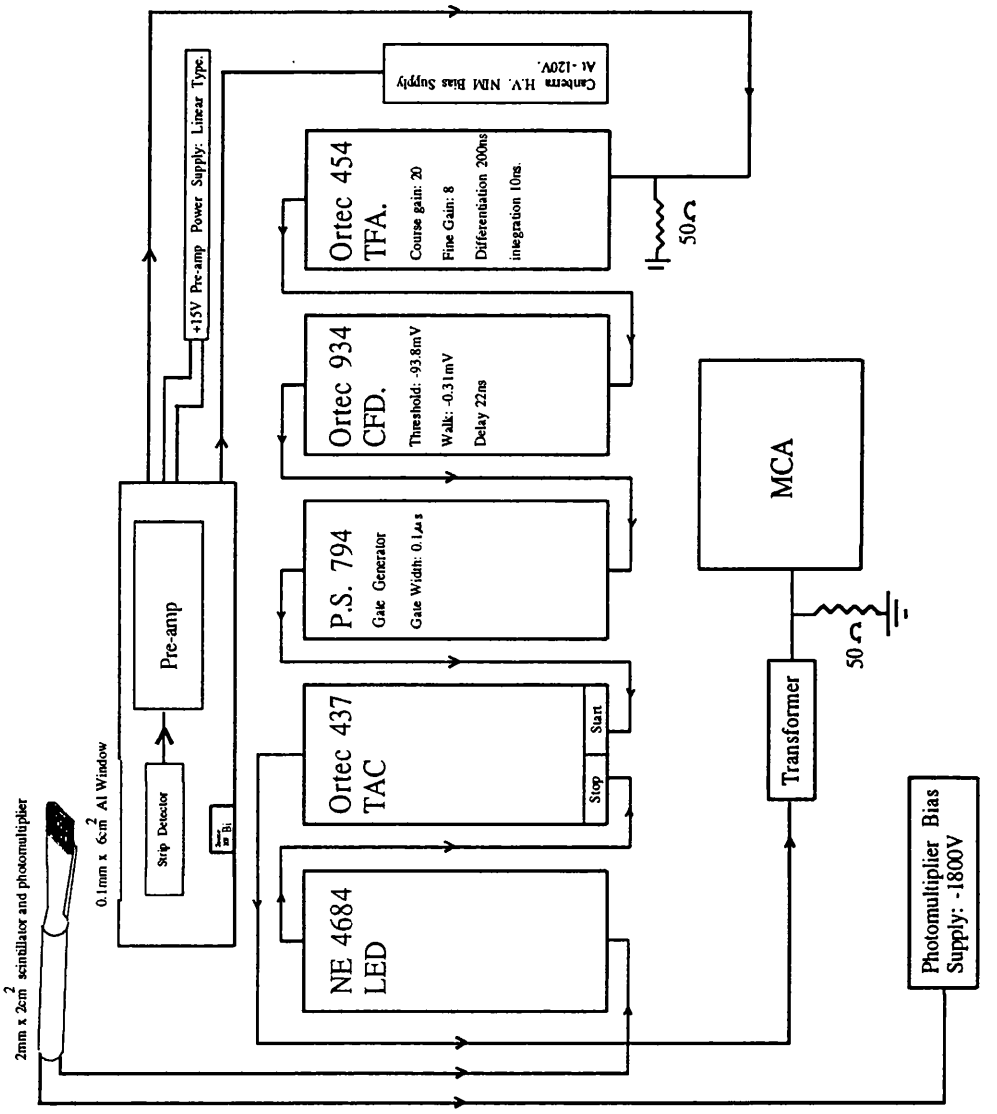

Figure 3.21: *Circuit Diagram Outlining Procedure for Logging a Co-incidence Spectrum.*

An energy calibration was obtained from the conversion electron peaks observed in the strip detector spectrum, when gated only on its CFD, in the same way as that of FIGURE (3.9). The spectrum in FIGURE (3.22) corresponds to the energy spectrum of the signal pulses contributing to the timing test and peaks at 200 keV. The small difference in the position of the minimum-ionising peak, compared to 209 keV peak seen in FIGURE (3.9), is probably due to the slightly different geometry.

In the timing test, conventional CFD timing was observed to produce ~7 ns timing, with a delay of 40 ns. The timing part of a CFD conventionally works by splitting the input pulse into two with a resistive divider. Conventionally, one pulse is -0.2 times the amplitude of the other. These pulses are then summed and fed into a comparator which is triggered when the sum of the signals is zero. If the large pulse is delayed by 80% of the pulse risetime, then the zero crossing point occurs when the fraction pulse reaches its peak. The zero trigger point will be independent of the input pulse amplitude, but not of risetime. If triggering occurs on average where the fraction pulse reaches its peak, then the amount of jitter can be dependent on either the gradient of the rising edge of the signal, or that of the falling edge of the signal. Since the gradient of the rising edge is large and the effect of jitter is minimised where the gradient is steepest, it is desirable that all pulses trigger before the fraction pulse reaches its peak. This is achieved by setting the delay on the large pulse to slightly less than that required for the fraction to reach its peak at the zero crossing point. Minimising CFD jitter in this way is known as ARC (Amplitude and Rise Compensated) timing. The optimum delay for ARC timing is however dependent on the signal:noise ratio. This is because the average point on its rising edge, which the fraction pulse reaches at the zero-crossing point, should

be well outwith the baseline noise. ARC timing is therefore only feasible with a good signal:noise ratio.

A delay of 27 ns was found to produce the best timing resolution in this test. After careful adjustment of the CFD walk control, the best timing resolution was found to be 4.6 ns.

FIGURE(3.23) shows the time spectrum obtained from the optimised system. For the 100 keV $\rightarrow$ 300 keV energy range it represents (see FIGURE (3.22)), this was more than a factor of two better than the $\sim$12 ns obtained for the walk independent timing resolution in this energy range in the previous section. TABLE (3.1) in the previous section indicated that 4.6 ns resolution could be attained by depositing $\sim$470 keV. Therefore, the signal:noise ratio in this test is approximately a factor of 2 better, as is also indicated by the lowest point in the valley between the signals and noise being at 100 keV, instead of 180 keV. Thus, careful noise reduction when the signals are so close to the noise level can result in more than a factor of two better timing resolution.

3.8 Conclusions

The indications from these initial tests are that although this strip detector can be used for improved tagged photon energy resolution, an increase in the beam intensity without degradation of the real:random ratio seems unlikely. If the strip detector is used for timing and the beam operated at the present specified current, then the increase in the real:random ratio due to smaller detector geometry is offset by the decrease due to poorer timing. Pile-up on the 200 ns long tail pulse of the TFA, as discussed in§3.6, also restricts the beam intensity to little more than its present value. Even if retaining the

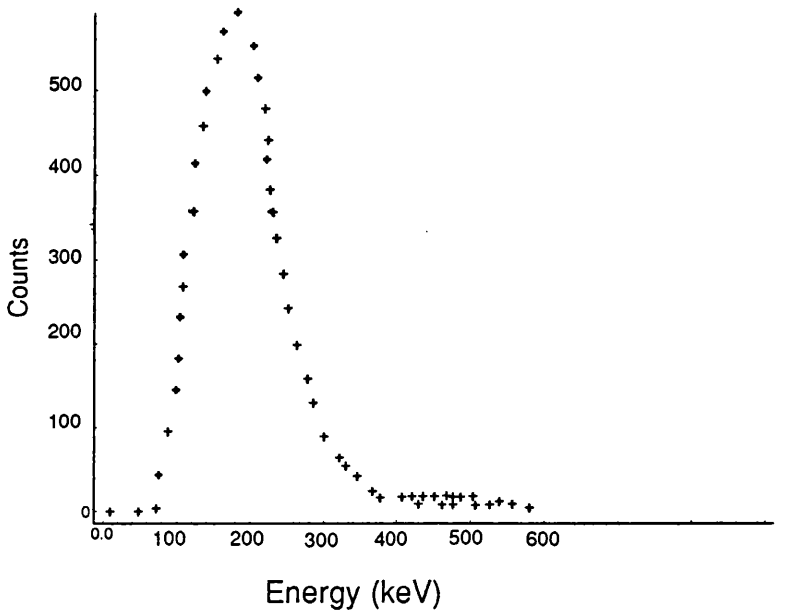

Figure 3.22: *Pulse Height Spectrum in the Strip Detector, Gated on Coincident Pulses.*

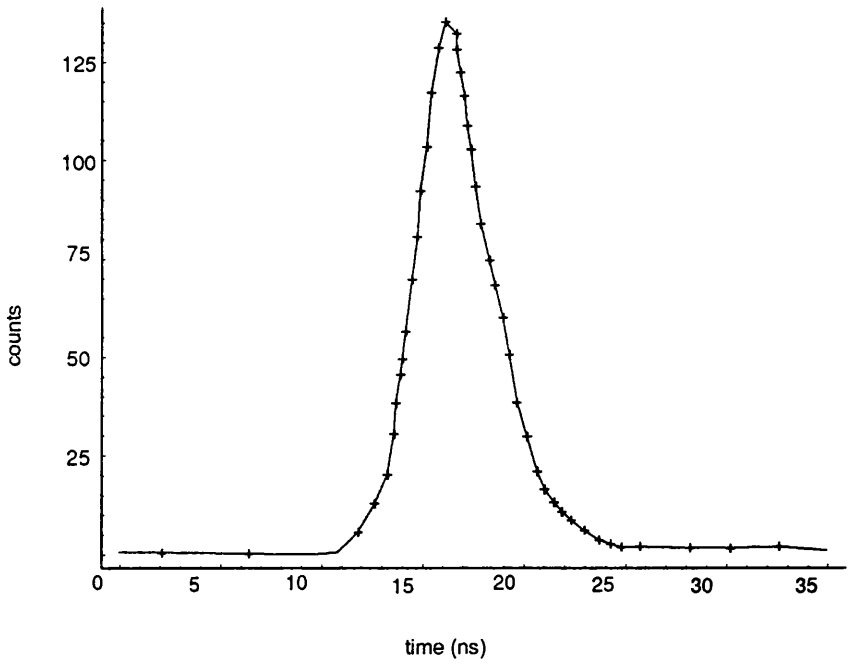

Figure 3.23: *TAC Spectrum.*

present beam intensity was considered acceptable, the maximum tolerance of 5 ns timing resolution in the tagger ladder means that it would undesirable to use a detector whose timing has been shown to be no better than 4.6 ns for the energy deposited by the tagger electrons and more realistically, as poor as 14 ns at this energy.

The problem of obtaining a fast timing prompt from the focal-plane detector array can be solved by operating a strip detector focal-plane detector array in coincidence with the current focal-plane detector scintillator array, so that the scintillators provide the timing and the strip detectors provide the energy resolution. Such a coincidence however, offers no solution to the problem of increasing the beam intensity. As well as pile-up in the strip detector, the phototubes of the present detector array will, for example, burn out in about half a year if the beam intensity was increased by a factor of 10. In high resolution experiments where photon bins, derived from the individual, high resolution, focal-plane detecting channels are needed, a factor of 6.5 less counts will therefore be recorded in each strip detecting element, compared to that recorded in the focal-plane scintillators. This means that such experiments would have to be run 6.5 times longer, if it was necessary to obtain the same statistics in each strip detector element, as was determined to be desirable in the scintillators. However, in many experiments, where high resolution is required in some derived quantity, such as missing energy, the data can be analysed in quite large photon bins. Provided this bin width is $\geq$ 2 MeV, the counting statistics would be no worse than for the existing focal-plane detector system. In these experiments, operating the strip detectors and scintillators together in coincidence would be an acceptable option. In that case, a 1000 μm thick strip detector would provide an even better signal:noise ratio than the 500 μm one

tested and give a clearer separation between the signals and the noise, compared to that which would expected from the results in §3.6, but the 500 μm detector should suffice unless the noise in the focal-plane is very much worse than in the environments tested.

If many experiments requiring photon bins, derived from the individual, high resolution, focal-plane detector channels, are envisaged, then a different silicon strip detector should be considered. This detector must have better timing resolution and allow use of a shorter differentiation time, while preserving enough of the unfiltered pulse amplitude to give a good signal:noise ratio. There are two aspects to achieving better timing by reducing jitter. One is to reduce the noise. If this can be achieved, then there is the added advantage that the discriminator can be set lower, where the pulse gradient is steepest. A comparison of the walk independent timing resolution obtained for minimum-ionising electrons in §3.6 and §3.7 clearly demonstrates how significant these effects are. i.e. 14 ns in §3.6, against 4.6 ns in §3.7. There are a number of ways the noise could be further reduced in the detector which haven't been fully investigated. The detector could be cooled, to reduce the leakage current, which varies exponentially with temperature. The detector and its electronics could all be mounted as close together as possible, possibly with the strip detector and pre-amp on one board, to minimise the effects of pick-up and stray capacitance and inductance. The feedback capacitance of the pre-amp could be reduced to 1 pF, to reduce the bandwidth and therefore the noise, as explained in §3.5. The NIM TFA and CFD could be replaced by a high density circuit board. However, in FIGURE (3.19), the timing resolution increases very slowly with the signal:noise ratio, when more than 450 keV is deposited in the strip detector. This indicates that timing resolution will not reach values much lower than 3 ns,

unless a very large improvement in the signal:noise ratio is obtained. The above suggestions for noise reduction would go some way to improving the signal:noise ratio, but it is highly unlikely that the desired 1 ns timing could be achieved for this detector with minimum-ionising electrons.

The other way of improving the timing is to increase the gradient of the signal pulse at the trigger point by having more ionisations in the detector and/or a faster charge collection time. More ionisations can be achieved by increasing the detector thickness. Faster charge collection can be obtained by using lower resistivity material, capable of withstanding larger potential differences. Lower resistivity detectors have the added attraction of being less sensitive to the effects of radiation damage, since radiation damage becomes important when the number of introduced damaged centres equals the number of dopant atoms, [20]. MICRON, [21], currently supply 500 μm detectors with resistivities of 47 $\rightarrow$ 71 Ω.m, capable of some degree of overbiasing. At full depletion, and at a temperature of 20 °C, MICRON indicate that these detectors should have a risetime of $\sim$1 ns/100 μm, 10% $\rightarrow$ 90%, corresponding to a saturated electron velocity over most of the detector. However, with approximately the same signal:noise ratio as that observed in §3.6, using the same detector thickness would mean that the detector was operating in the region where the signal:noise ratio has a very significant effect on the timing resolution obtained for the electrons detected in the tagger. Even if cooling were used to reduce detector leakage current, at least 50% of the noise comes from other sources and is difficult to eliminate. This can be deduced by comparing the signal:noise ratios seen in §3.6 and §3.7. The energy produced in a 500 μm strip detector will therefore always result in a borderline signal:noise ratio for 100 MeV electrons, unless substantial work is done to minimise the effect of the environment on the signal:noise ratio.

A thicker detector would make the timing less dependent on signal:noise for the 100 MeV electrons. It is not however desirable to make the detector too much thicker, as this can degrade the energy resolution of the the focal-plane detector array and introduce a very large difference in the high and low electric field ends of the detector. The reasons for these limitations were discussed in §1.2 and §3.3 respectively. If the thickness is increased to 1000 μm, then ~460 keV would be deposited in the detector. For noise of approximately the same amplitude as that of §3.6, the signal:noise ratio obtained from a 1000 μm detector would therefore be in the region of the curve of FIGURE (3.19) where timing resolution changes slowly with signal:noise ratio. If a lower resistivity is used to fabricate the 1000 μm detector, then the voltage that can be applied across it and indeed the voltage required to reach full depletion, is much larger. A decrease in charge collection times is also attained. Although it is not actually possible to attain a field capable of saturating the electron and hole drift velocities across the whole of the detector strip, it is possible to saturate their drift velocity across a large fraction of it. This fraction can be increased by cooling the detector, since as stated in §3.3, both electron and hole mobilities are temperature dependent. Cooling is also beneficial in increasing the saturation velocity of the holes, since it is highly temperature dependent. The saturation velocity of electrons does not change appreciably from the 10^5 ms^{-1} obtained at room temperature [22]. Further, the increase in leakage current observed in thicker detectors, [23], will be negligible in cooled detectors, since it will be the amplifier noise that dominates. L. Evensen et.al., [22], have constructed a 1000 μm strip detector for use with the Atlas Positron Experiment. The detector has a resistivity of 98 $\rightarrow$ 110 Ω.m and a corresponding depletion voltage of 370 $\pm$ 40 V. To achieve such high fields without breakdown, a special, segmented guard

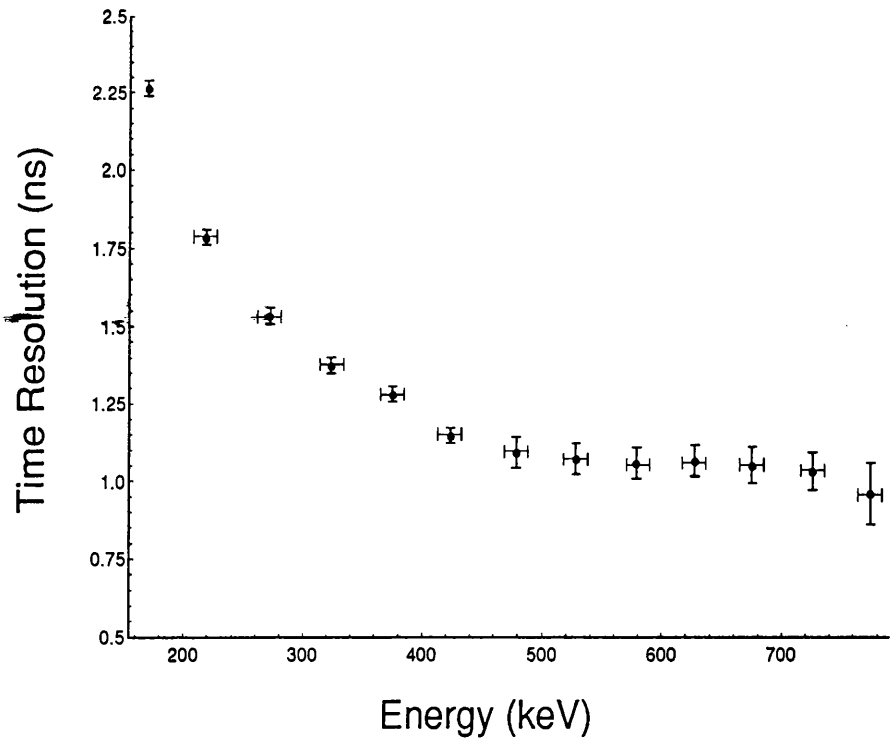

Figure 3.24: *Variation of Timing Resolution with Energy Deposited in a 1000 μm Detector.*

ring electrode was constructed, to reduce the leakage current [22]. FIGURE (3.24) shows how timing resolution varies with energy deposited for this detector at full depletion, when the detector was cooled to -130 °C. The detector has timing resolution of ~1 ns, for electrons which deposit ~ 450 keV in the detector. To show how time resolution varied with operating temperature, Evensen et. al. plotted time resolution against temperature, for electrons depositing 390 → 435 keV in the detector. See FIGURE (3.25). By cooling the detector from room temperature to -130 °C, there is approximately a factor of 2 improvement in the timing resolution.

It is necessary to preserve the faster rising edge of faster detectors, so further attention must now be paid to the pre-amp configuration. Given that the integration time of the pre-amp should therefore be $\leq$ 10 ns, it is necessary from EQUATION (3.5) to have a total input capacitance of ~ 27 pF to the

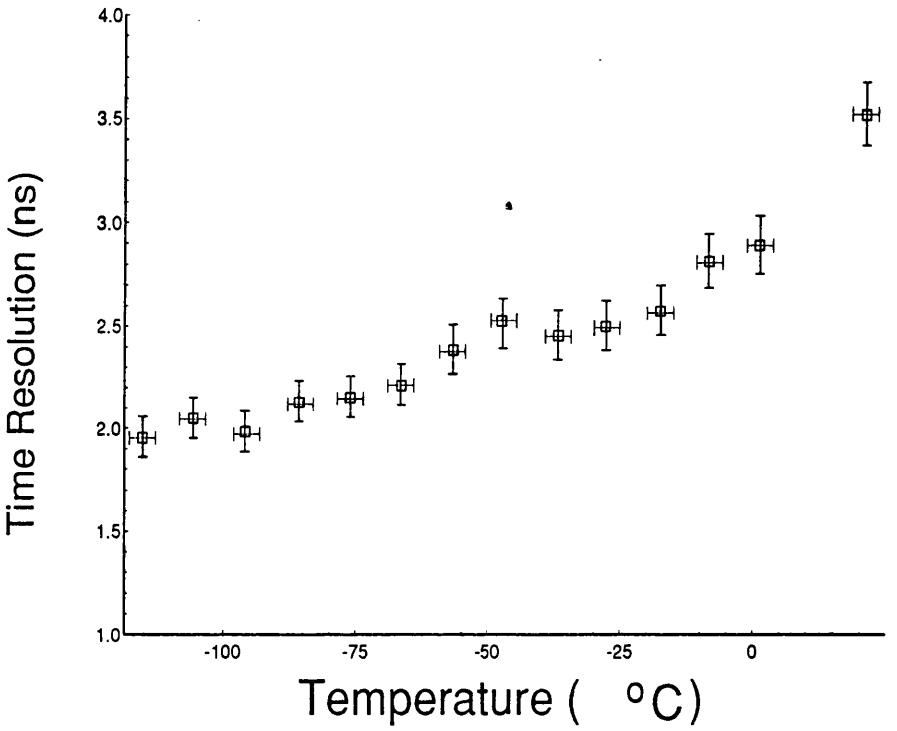

Figure 3.25: *Variation of Timing Resolution with Temperature in a 1000 μm Detector.*

pre-amp. The FET input capacitance of the pre-amp is 20 pF. Although it may be possible to further reduce the input capacitance of the pre-amp by using an FET with a smaller capacitance, the transconductance of the FET will decrease with decreasing capacitance and this will lower the open loop gain of the amplifier and increase the series noise contribution of the FET input, neither of which is desirable. The sum of all other input capacitances should therefore not exceed 7 pF. The detector to pre-amp connection must therefore be kept very short, to minimise this contribution to capacitance. The detector itself from EQUATION (3.3) has a capacitance which is proportional to surface area and inversely proportional to thickness. From §1.3, the surface area can be reduced most easily by minimising the detector height. The magnet should therefore be operated with the quadrupole at maximum strength, allowing a detector height of 12 mm, if 85% is considered an adequate counting efficiency for the focal-plane. This calculation must however be experimentally verified, before such a decision is made. Assuming this detector height is acceptable, a 1000 μm detector strip has a capacitance of $\sim$ 2.5 pF. Stray capacitance, edge effects and cabling must therefore be kept to $\sim$ 5 pF. For this pre-amp, minimising the input capacitance has the added advantage of decreasing the series noise, since this is proportional to input capacitance.

In summary, operating the 500 μm strip detector tested in coincidence with the current focal-plane detector array would be a straight forward and acceptable option, if operating at the current rate was acceptable. If a lower resistivity, $\sim$100 Ωm detector is used instead, then close to the desired 1 ns timing resolution should be possible. The count rate per MeV could then be increased by a factor of 6.5, without reducing the real:random ratio. All of the objectives outlined in Chapter 1 could therefore be met. A good signal:noise ratio is easily

attained from a 1000 μm detector. Indeed the decrease in capacitance observed in thicker detectors should be beneficial to the signal:noise ratio. If such a detector is used, however, it must be cooled to -130°, to attain high mobilities and a small leakage current, if 1 ns timing is to be realised. A good enough signal:noise might also be possible at room temperature, with a low resistivity 500 μm detector from MICRON, if the question of noise is more carefully addressed and is made less dependent on environment.

The RAL 108B pre-amp may be used, if the detector height is reduced to 12 mm. This is only possible with the quadrupole on. Otherwise, a voltage sensitive pre-amp must be used, since all FET's have a similar input capacitance. As previously explained, this is not desirable for a strip detector. With the shorter charge collection time of this 1000 μm detector, a shorter differentiation time is possible. A reduction to about 50 ns would suffice for the count rates suggested.

In summary, the strip detector and pre-amp, tested in §3.6 and §3.7, could be used to form the basis of a high resolution focal-plane detector array, if the timing was provided by existing focal-plane detector. In this case, experiments are limited to those in which high resolution is only required in some derived quantity, such as missing energy, since the rate of the beam could not be increased beyond its present maximum limit.

If both good timing and a higher rate are required, then lower resistivity strip detectors, with a much shorter charge collection time, should be tested. In this case, all methods of improving the timing and/or signal:noise ratio should be investigated, since 1 ns timing will not be easily achieved with any suitable strip detector.

Chapter 4

Design of An Integrated Timing Circuit

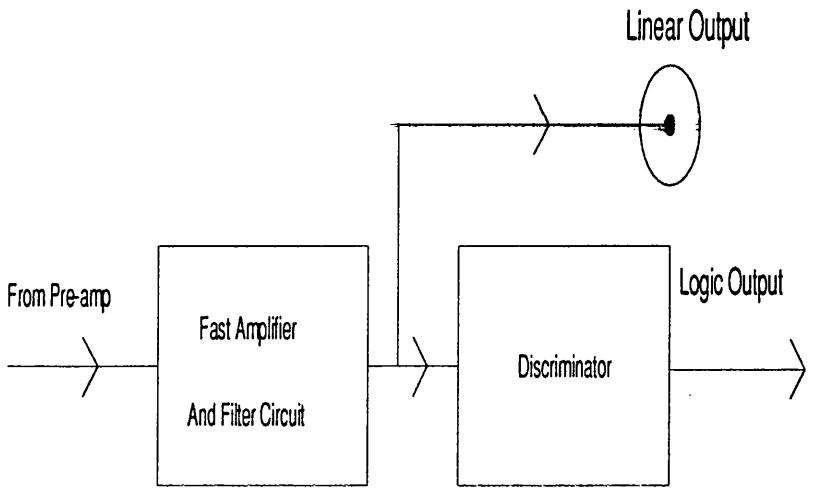

Figure 4.1: *Outline of PCB Components.*

4.1 Design of an Integrated Circuit for Production of a Reliable Timing Signal

The limited space in the focal-plane, means that the NIM electronics used for shaping, amplification and discrimination in §3.6, would have to be housed remotely from the detector and pre-amp. It would be more convenient to have all the electronics near the detector. This would also reduce pick-up and stray capacitance and inductance. A component circuit board (pcb) will therefore be designed, to replace the NIM modules. The optimised parameters for the shaping of the pre-amp output pulse, from the tests in §3.6, served as a guide in this design. An outline of what must be included in one channel on this board is shown in FIGURE (4.1).

4.2 Amplifier Design :

The op-amp chip chosen was an OPA620KP from BURR-BROWN, [24], primarily because it features;

(1) A wide unity gain bandwidth of 300 MHz; the bandwidth of an amplifier is dependent on the gain, decreasing as gain increases. The upper limit on bandwidth is the value obtained when the gain is one. The unity gain bandwidth must therefore be large enough to facilitate processing of the wide range of composite frequencies in the pre-amp output pulse at the required gain, without distortion of the highest frequencies. Otherwise, the risetime, which depends on the high frequency components, will be degraded.

(2) A high slew rate of 250 mV/ns. Slew rate gives the limitations on the maximum gradient at which a voltage pulse changing with respect to time can rise. For a typical output pulse from the pre-amp of 2 mV/50ns, there is ample scope for a high gain, without distortion of the leading edge.

Other Specifications:

SUPPLY VOLTAGE: ± 5 V.
INPUT OFFSET VOLTAGE: $\pm 200\mu$V.
COMMON MODE REJECTION: 75 dB.
INPUT NOISE (frequency = 1 to 100 MHz): 2.3 nV/$\sqrt{(Hz)}$.

This op-amp will first be utilised in the construction of an amplifier filter circuit, to integrate out the high frequency noise and apply enough differentiation to clip the long decay of the signal pulse, as in §3.6. The layout for the circuit is illustrated in FIGURE (4.2). The resistive and capacitive values

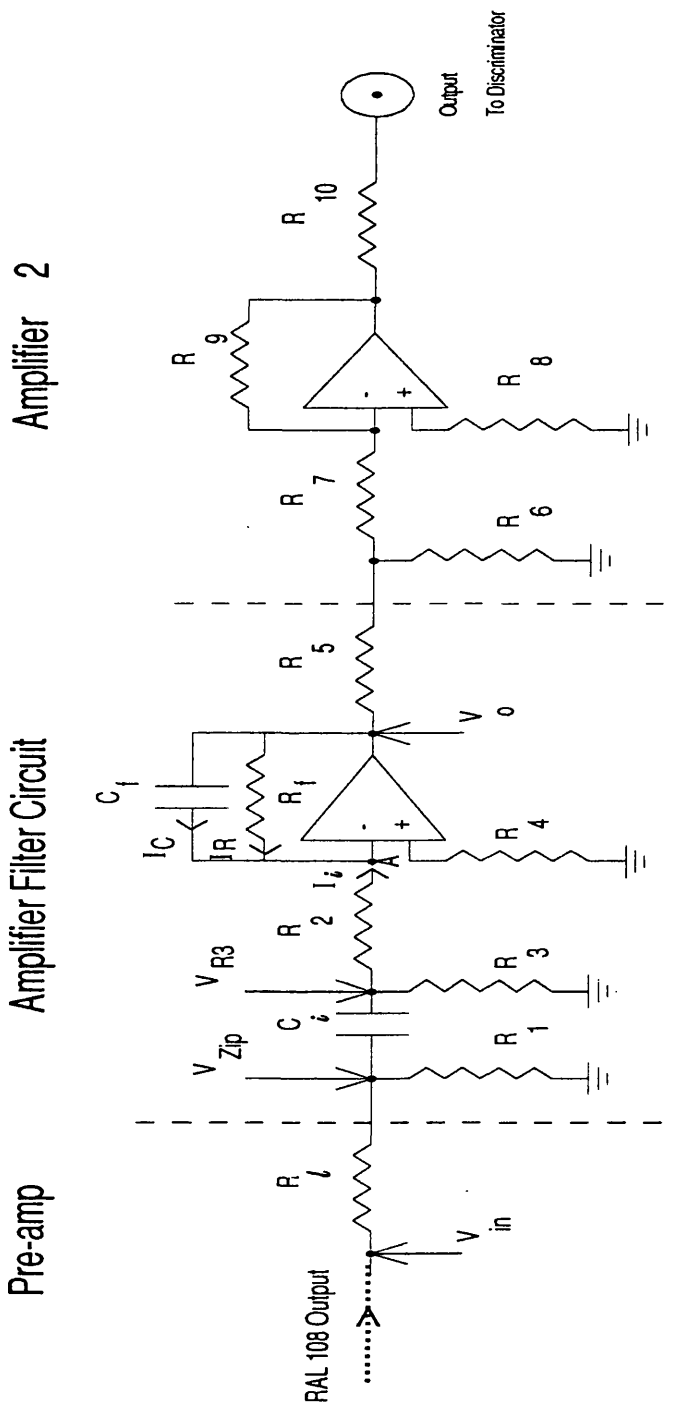

Figure 4.2: *Layout of the Filter Circuit*

chosen for this circuit are listed in TABLE (4.1) The choice of components in the amplifier filter circuit shown in FIGURE (4.2) can be justified as follows:

(1) The input resistance of the filter circuit must be impedance matched to the 100 Ω load on the pre-amp and to the cable connecting the pre-amp to the filter circuit, to exclude any reflections. As in the NIM tests in §3.6, 3.7, a 50 Ω termination was used instead of 100 Ω at the amplifier input, to match the cable impedance. R_1 is therefore a 50 Ω resistor.

(2) The differentiation time should be of the order of 200 ns. A shorter time constant would reduce the amplitude of the fastest frequency components of the rising edge, while a longer time constant would result in a tail so long that the pile-up would be observed at the rate at which it is proposed that the detecting system operate. It is desirable that C_i be as large as possible. (The reason for this will be explained below.) Therefore, the resistance which forms the differentiation time constant with C_i must be as small as possible. If R_3 is much smaller than R_f, then the differentiation time constant will be determined by R_3C_i, not R_fC_i. The gain of the circuit can therefore be altered, independent of the required differentiation time, by adjusting R_f. R_3 is set at 220 Ω. This is the smallest R_3 can be without appreciably affecting the input impedance of the filter circuit seen by the pre-amp. Although the differentiation could also be done by placing C_i in front of R_1, this would make the input impedance to the filter circuit frequency dependent and could cause undesirable reflections.

(3) R_4 is necessary to provide the correct DC levels for the op-amp. For this circuit, $R_4 \simeq R_2$.

(4) The output from the op-amp is driven into 50 Ω, as suggested in the specifications.

Circuit Component	Value Assigned
R_1	50 Ω
R_2	220 Ω
R_3	220 Ω
R_4	220 Ω
R_f	1 KΩ
R_5	50 Ω
R_6	50 Ω
R_7	50 Ω
R_8	50 Ω
R_9	1 KΩ
R_{10}	50 Ω
C_i	1000 pF
C_f	10 pF

Table 4.1: *Values Assigned to Components in FIGURE (4.2)*

(5) Integrating out the high frequency noise should be executed with the smallest time constant possible, to retain the fast rising edge of the pulse. This need be no larger than the optimum 10 ns integration time experimentally determined for the NIM TFA in §3.6.

(6) Gain should be controlled by the resistor ratio of R_f:R_2, for two basic reasons: at the input, the impedance of C_i will add to that from the input resistances R_1, R_2, R_3, to give a total impedance at the amplifier input, which increases as the signal frequency decreases. Since a larger impedance at the amplifier input reduces gain, the capacitive impedance obtained for the leading edge frequency components, should be small relative to those of the input resistances. In the feedback loop, analogous to the above, the impedance of C_f rises with decreasing frequency. Gain therefore increases for the lower frequency components, partially cancelling the effects of differentiation. The impedance of C_f , $Z(C_f)$, again calculated at the frequency component of the leading edge, should therefore be much larger than R_f .

(7) Gain is limited by the maximum, recommended value of $R_f = 1$ KΩ and by the gain bandwidth product.

The gain, V_o/V_{Zip}, of any amplifier filter circuit of this type, can be calculated for the general case shown in FIGURE (4.2a), where R_1, R_2 R_3 and C_i, have been replaced by the effective, equivalent impedance Z_i, chosen so that the current, I_i, is the same as that in FIGURE (4.2). Applying Kirchoff's current rule to the virtual ground at point A, formed because the input impedance to the pre-amp is so large that virtually no current flows into it, gives

$$I_i \simeq -(I_C + I_R) \tag{4.1}$$

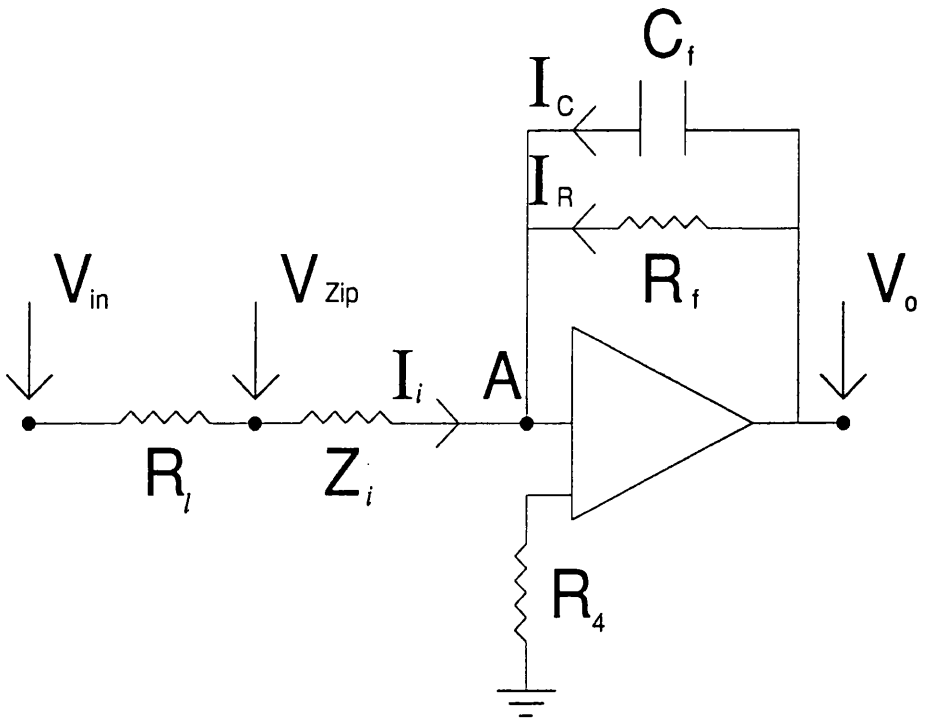

Figure 4.2a: *General Equivalent Amplifier Filter Circuit*

where I_R and I_C are the feedback currents in the resistor and capacitor branches respectively. Hence

$$\frac{V_{Zip}}{Z_i} \simeq \frac{-V_o}{Z(C_f)} - \frac{V_0}{R_f} \tag{4.2}$$

and

$$GAIN = \frac{V_0}{V_{Zip}} = \frac{-Z(C_f)R_f}{Z_i(R_f + Z(C_F))} \tag{4.3}$$

Also,

$$Z(C_f) = \frac{T}{(2\pi j C_f)} \tag{4.4}$$

where T is the period of the frequency component. Substituting EQUATION (4.4) into (4.3);

$$GAIN = \frac{-TR_f}{Z_i(2\pi j C_f R_f + T)} \tag{4.5}$$

R_f must be large for a high gain, yet the product $2\pi C_f R_f$ should remain comparatively smaller than the period of the highest frequency component which contributes to the rising edge of the filter circuit, enabling the resistive characteristics to dominate the gain at all frequencies contained in the signal pulse. The highest frequency component of the rising edge is estimated to have a period, T_{max}, equal about four times the 10-90% pulse risetime. Therefore for a 50 ns risetime, T_{max} = 200 ns. The variation of the gain of the circuit with frequency in EQUATION (4.5), can be calculated for some value of the product $2\pi C_f R_f$. C_f was set to 10 pF and R_2 to 220 Ω. This still allows for a suitable integration time constant of $Z_i C_f$ ~2.2 ns. R_f = 1 KΩ. Therefore $2\pi R_f C_f = 6.28 \times 10^{-8}$ s. The fraction by which the purely resistive gain is reduced due to the capacitor, C_f is thus given by;

$$FRACTION = \frac{T}{6.28j \times 10^{-8} + T} \tag{4.6}$$

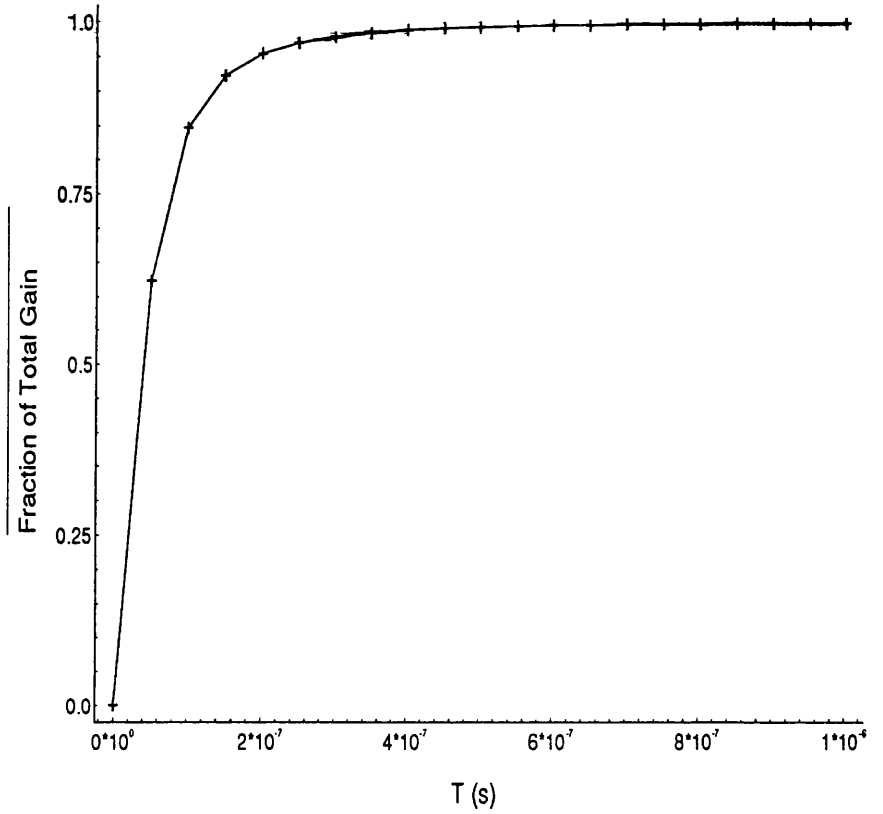

Figure 4.3: *Variation of the Capacitive Contribution to Gain with Frequency*

and the mean value of the fraction, $\overline{FRACTION}$ is;

$$\overline{|FRACTION|} = \frac{T}{((6.28 \times 10^{-8})^2 + T^2)^{\frac{1}{2}}} \tag{4.7}$$

FIGURE (4.3) shows the how effect of the capacitor on the mean gain, varies with frequency. The gain at T = T_{max} is 95.2% of the gain in the limit of T $\rightarrow$ ∞, where gain is purely resistive. This value for the product $R_f C_f$ is therefore considered to be acceptable, with the rising edge having a gain which is 95.2% of the gain of a DC component.

In the calculation of the gain, the variation of Z_i with frequency was neglected, since the singular concern here was the determination of acceptable values for C_f and R_f . Using the same notation as above, the effect of Z_i on the gain of the amplifier filter circuit in FIGURE (4.2), will now be assessed.

Taking V_{in} to be the voltage indicated in FIGURE (4.2), the voltage seen at the input of the amplifier filter circuit, V_{Zip}, is first calculated. This is then used to assess the effect of Z_i on gain. R_2 is neglected in the calculation of V_{Zip}, because its effect is obscured by the fact that it is in series with the amplifier input, which has an internal resistance of 15 KΩ.

From FIGURE (4.2) the sum of the filter circuit input impedances, Z_{ip}, is given by;

$$\frac{1}{Z_{ip}} = \frac{1}{R_1} + \frac{2\pi jC_i}{2R_3\pi jC_i + T} \tag{4.8}$$

$$Z_{ip} = \frac{R_1(T + 2\pi jC_iR_3)}{T + 2\pi jC_i(R_3 + R_1)} \tag{4.9}$$

Also

$$V_{Zip} = \frac{V_{in}Z_{ip}}{Z_{ip} + R_l} \tag{4.10}$$

where R_l is the pre-amp load resistance and equals 100 Ω. The pre-amp output capacitance has been omitted here because it is too large to be of consequence.

Substituting the expression for Z_{ip}, deduced in EQUATION (4.9), into EQUATION (4.10);

$$V_{Zip} = R_1V_{in}\frac{T + 2\pi jC_iR_3}{(R_l + R_1)T + 2\pi jC_i(R_lR_3 + R_1R_l + R_1R_3)} \tag{4.11}$$

V_{Zip} has a mean value of

$$\overline{V_{Zip}} = R_1 V_{in}\left(\frac{T^2 + (2\pi C_i R_3)^2}{T^2(R_l + R_1)^2 + (2\pi C_i(R_l R_3 + R_1 R_l + R_1 R_3))^2}\right)^{1/2} \qquad (4.12)$$

The ratio of the input voltage, $\overline{V_{Zip}}$, of the filter amplifier, to that seen across the pre-amp feedback loop, V_{in}, illustrates the drop in gain observed when the pre-amp and filter amplifier circuit are housed on separate pcb's, which have to be properly terminated for impedance matching. Substituting the values chosen for the variables in this circuit, $\overline{V_{Zip}}/V_{in} \simeq 0.3$. This is a very poor ratio. It could be improved by putting the filter circuit and pre-amp on one board, but this is not practical, because of both the limited space in the focal-plane and since it is desirable to mount different parts of the detecting system on different boards, for easy substitution of faulty constituent elements. One way of improving this ratio however, would be to use a 100 Ω cable with R_1 also equal to 100 Ω, so that the voltage drop observed across the pre-amp load resistor is smaller. This would require R_3 to be doubled, so that it did not appreciably affect the input impedance to the filter circuit. To retain the same differentiating time constant, C_i would therefore have to be halved.

To estimate the effect of C_i on gain, the voltage, V_{R3}, which will be seen across R_3 and hence R_2, when V_{Zip} is the input voltage to the amplifier, is first calculated:

$$V_{Zip} = V_{Ci} + V_{R3} \qquad (4.13)$$

where V_{Ci} is the voltage seen across C_i and since the current through R_3 is approximately the same as that through C_i, V_{Ci} is given by:

$$V_{Ci} = \frac{TV_{R3}}{2\pi j R_3 C_i} \qquad (4.14)$$

Rearranging EQUATION (4.13) in terms of V_{R3} and substituting for V_{Ci}, from EQUATION (4.14):

$$V_{R3} = \frac{2\pi j C_i R_3 V_{Zip}}{2\pi j C_i R_3 + T} \tag{4.15}$$

In terms of $\overline{V_{R3}}$;

$$\overline{V_{R3}} = \frac{\overline{V_{Zip}}}{((\frac{T}{2R_3\pi C_i})^2 + 1)^{1/2}} \tag{4.16}$$

V_{eff} is the effective input voltage to the amplifier when C_i is short-circuited and is given by;

$$V_{eff} = \frac{R_1 R_3 V_{in}}{R_1 R_3 + R_l(R_3 + R_1)} \tag{4.17}$$

Again, R_2 is neglected in this calculation. By dividing EQUATION (4.16) by (4.17) and substituting (4.12), the resultant ratio $\frac{\overline{V_{R3}}}{V_{eff}}$ estimates the effect of the capacitor on the gain of the amplifier filter circuit.

$$\frac{\overline{V_{R3}}}{V_{eff}} = \frac{2\pi C_i(R_1 R_3 + R_l(R_3 + R_1))}{(T^2(R_l + R_1)^2 + (2\pi C_i(R_l R_3 + R_1 R_l + R_1 R_3))^2)^{1/2}} \tag{4.18}$$

Taking C_i to equal 1 nF, so that the differentiation time constant, R_3C_i, equals 220 ns, $\overline{V_{R3}/V_{eff}}$ can be plotted against T to see how the fraction of the total input voltage seen across R_2 varies with frequency, due to the insertion of C_i. FIGURE (4.4) illustrates this. Therefore with C_i = 1nF, at T = 200 ns, 99% of the input voltage to the filter circuit is observed across R_3. This decreases to 85 % for frequency components with a period of 1μs.

The gain of the amplifier filter circuit, defined in terms of the ratio, V_0/V_{Zip}, is given in EQUATION (4.5). From the definition of Z_i,

$$I_i = \frac{V_{R3}}{R_2} = V_{Zip} Z_i \tag{4.19}$$

and

$$GAIN = \frac{V_0}{V_{Zip}} = \frac{-T R_f V_{R3}}{R_2 V_{Zip}(2\pi j C_f R_f + T)} \tag{4.20}$$

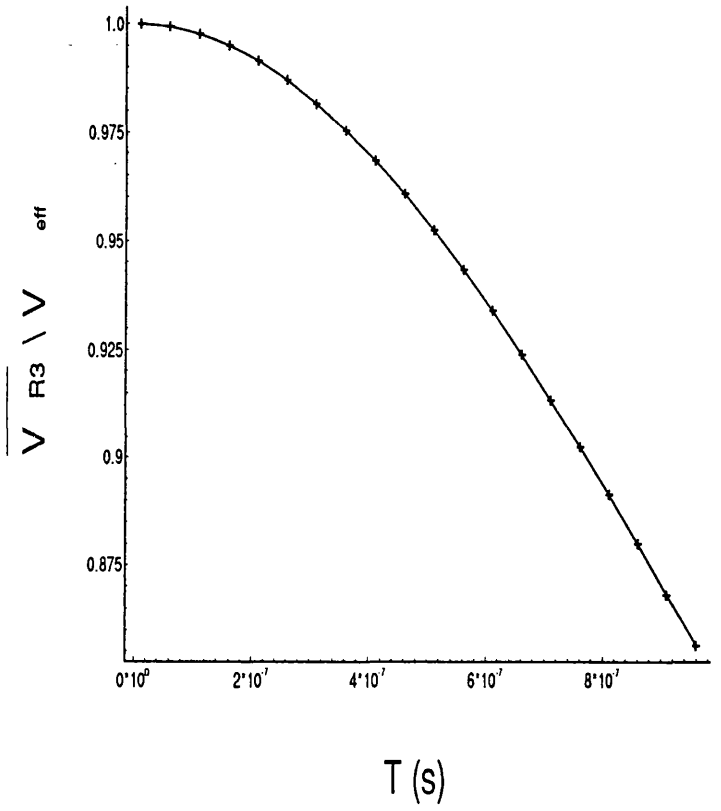

Figure 4.4: *Effect of C_i on Gain.*

However, this definition of gain neglects the dependence of V_{Zip} (for a specific energy deposited in the detector) on C_i and a more useful quantity is

$$\overline{|GAINB|} = \frac{\overline{V_o}}{V_{eff}} = \frac{(a^2+b^2)^{1/2}}{R_3^2R_2^2((c-4\pi^2(d+e))^2+4\pi^2(f+g)^2)^{1/2}} \tag{4.21}$$

where

$$a = 2\pi T^2 R_f C_i R_3 (R_1 R_3 + R_l(R_3+R_1)) \tag{4.22}$$

$$b = (2\pi C_i R_3)^2 T R_f (R_1 R_3 + R_l(R_3+R_1)) \tag{4.23}$$

$$c = T(R_l+R_1)(T^2 - 4\pi^2 C_i R_3 C_f R_f) \tag{4.24}$$

$$d = T R_3 C_i^2 (R_l R_3 + R_1 R_l + R_1 R_3) \tag{4.25}$$

$$e = T R_f C_f C_i (R_l R_3 + R_1 R_l + R_1 R_3) \tag{4.26}$$

$$f = T^2 C_i (R_l R_3 + R_1 R_l + R_1 R_3) - 4\pi^2 C_i^2 R_3 C_f R_f (R_l R_3 + R_1 R_l + R_1 R_3) \tag{4.27}$$

$$g = C_i R_3 T^2 (R_l + R_1) + C_f R_f T^2 (R_l + R_1) \tag{4.28}$$

EQUATION (4.21) was derived by substituting V_{eff} for V_{Zip} in EQUATION (4.20), taking V_{eff} from EQUATION (4.17) and V_{R3} from EQUATIONS (4.15) and (4.11). FIGURE (4.5) shows $\overline{|GAINB|}$ against T for the values listed for the components in this circuit.

The function peaks at 310 ns, with a gain of 4.37. This is quite close to the gain of 4.8 that would be obtained when both C_i and C_f are short-circuited. The integration time constant of the feedback loop dominates the gain at higher frequencies, on the rising edge of the peak, while the differentiation time constant dominates the falling edge. Ideally gain should peak at T_{max} = 200 ns, so that the leading edge is preserved, while the higher frequency noise components are not unnecessarily amplified. However, reduction of the peak position to 200

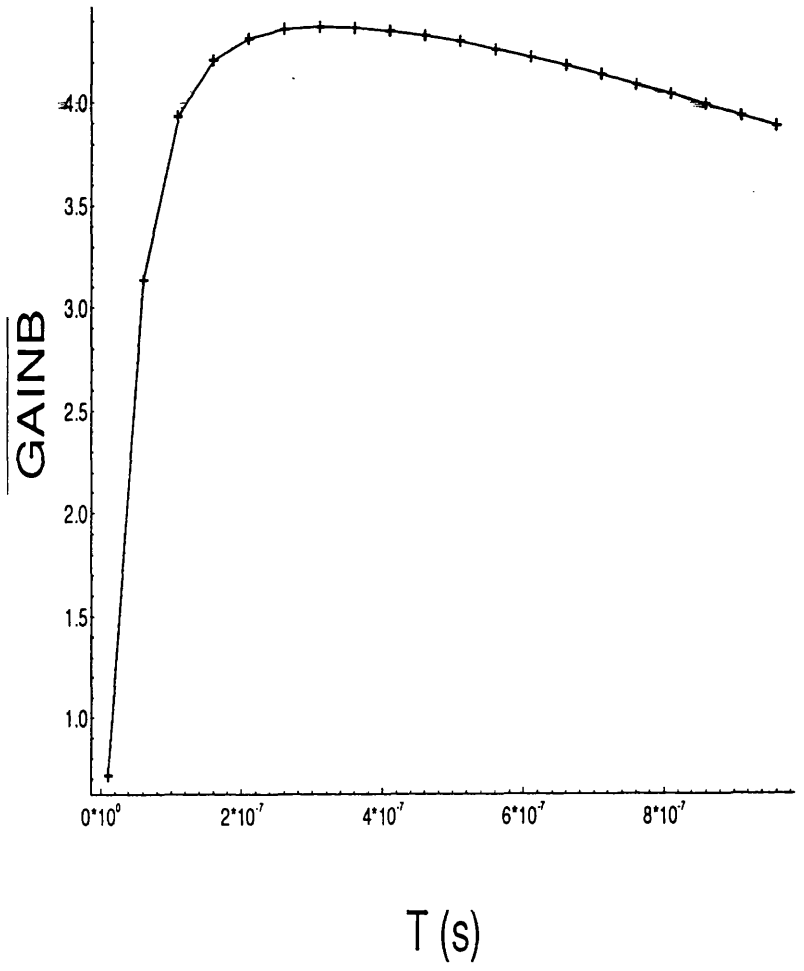

Figure 4.5: *Variation of* $\overline{GAINB}$ *of the Amplifier with Frequency.*

ns would enhance high frequency noise by a larger factor than it would increase the gain at 200 ns. Therefore, it can be concluded that the circuit is adequately optimised.

In summary, the circuit has an integration time of ~2.2 ns, a differentiation time of ~ 220 ns and a gain of between 2 and 4 over the composite frequencies of the pre-amp output pulse. These values are largely similar to those of the NIM test modules in §3.6. Although the integration time is shorter, the high frequency noise on the leading edge is smaller than that obtained with the NIM circuitry and a smaller degree of smoothing will therefore suffice. No pole zero cancellation was found to be necessary after differentiation, since the 150 μs tail of the pre-amp output pulse is so large compared with the differentiation time, that overshoot is negligible. The gain of the filter circuit is a factor of 25 less than that used on the NIM TFA. However the discriminator to be used (see §4.3) has a threshold of only 10 mV, compared to the 30 mV threshold in the NIM discriminator, so a factor of ~8 increase in gain is necessary. A second amplifier was inserted to cascade from the first to provide the extra gain required. See FIGURE (4.2). The second amplifier was again based on the OPA620KP chip. With a feedback resistance of 1 KΩ in the second amplifier, the total gain is about fifty.

The second amplifier may not be required once all the pcb electronics are mounted on the same board and put within the same box as the detector and the pre-amp. It has been shown that a factor of ~ 1.7 increase in gain can be achieved by changing R_1 in FIGURE (4.2) to 100 Ω. If the signal:noise ratio is improved by having all the pcb electronics mounted in this way and a smaller integration time can be used, then R_2 can be reduced to 100 Ω and the resultant

gain of the circuit would be $\sim$ 15, which would be large enough to trigger the discriminator.

4.3 An Onboard Discriminator

Detailed in FIGURE(4.6) is a development board incorporating a "RAL 10" constant fraction discriminator chip. The board design was adapted from that suggested by the maker [25]. The discriminator was configured to operate in constant fraction mode, but again was set for ARC timing, with a delay of 27 ns. The resistive divider network was set to give a fraction pulse of $\sim$0.2 times the height of the input, which is comparable to that on the NIM module. The walk adjust on the discriminator, primarily for correcting the constant shift incurred in the zero crossing trigger point due to the input switching charge, was set at 3.5 mV. The amplitude threshold was set where the noise count rate equalled the signal count rate, as in §3.6. The threshold was therefore set at $\sim$ 150 keV. This is a 20% improvement on the signal:noise ratio obtained with the NIM circuitry in §3.6.

4.4 Test of Onboard Timing Electronics

A multiparameter test, using the BaF_2 detector in a manner similar to that of §3.7, was conducted to compare the performance of the chosen, onboard electronics with that of the optimised NIM settings, for both timing and energy resolution. A circuit diagram of the set-up is illustrated in FIGURE(4.7).

There are however two differences from the TFA circuit suggested in §4.2 and §4.3. For versatility, the two parts of the amplifying system and the discrimina-

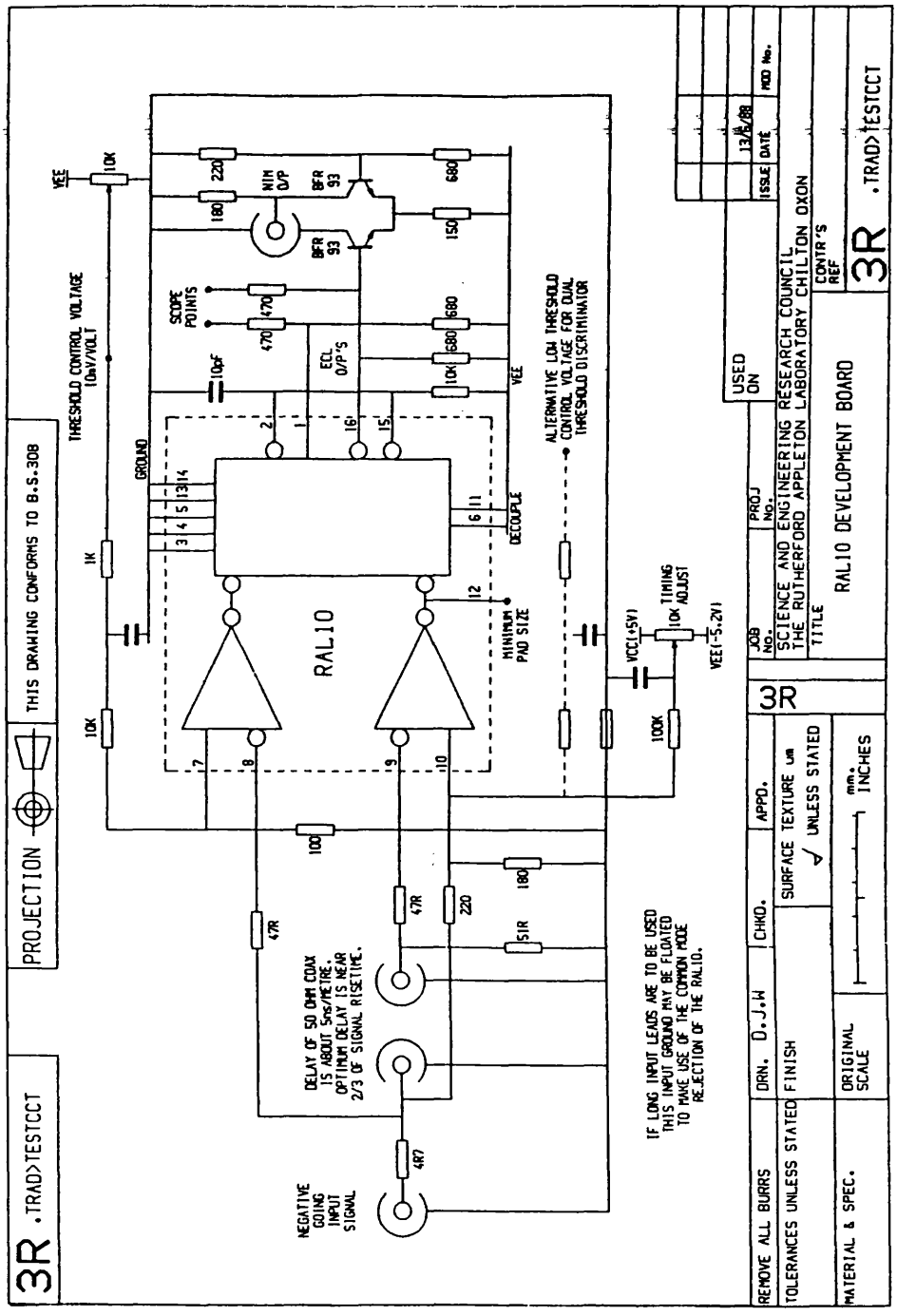

Figure 4.6: *The RAL10 Discriminator*

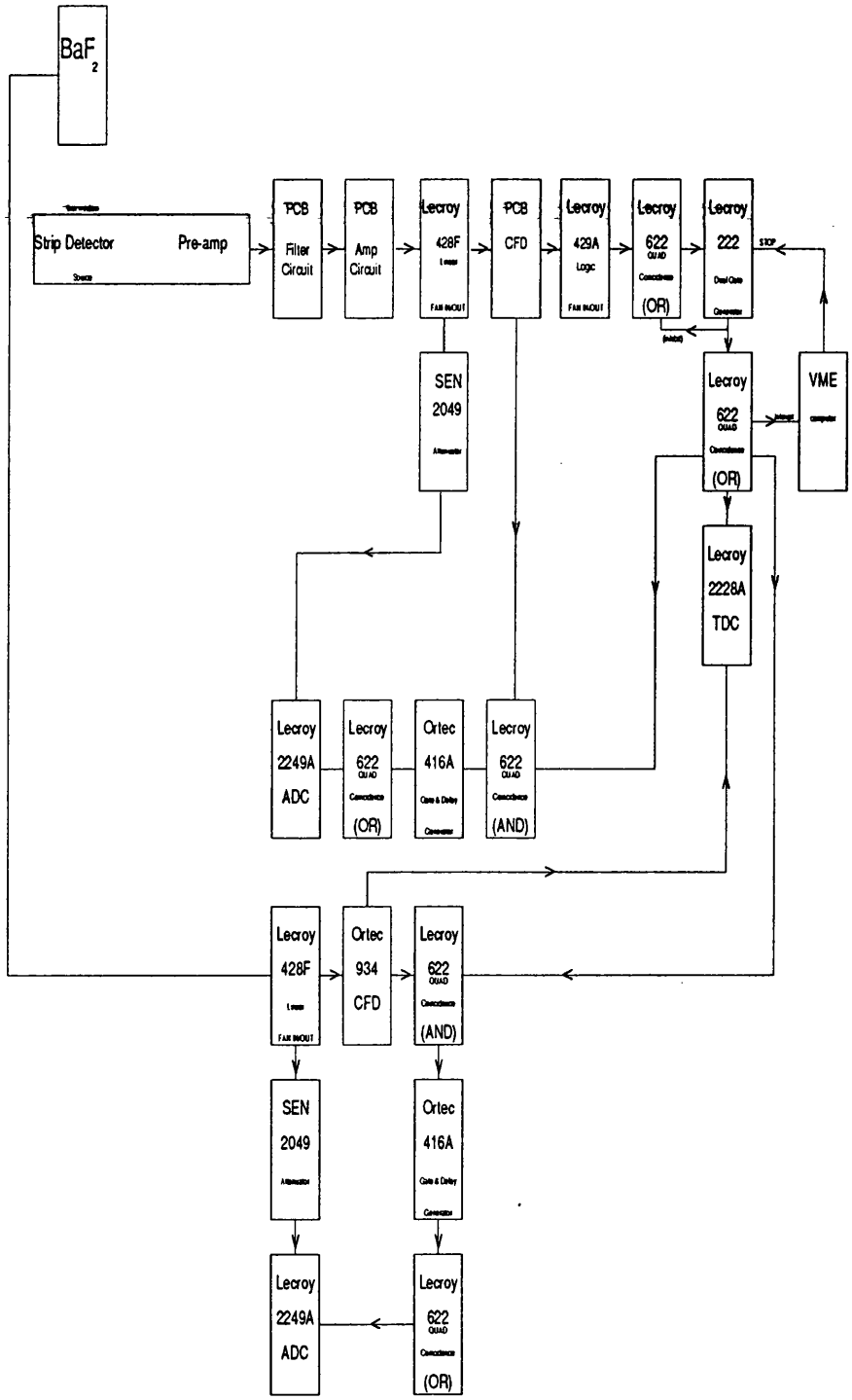

Figure 4.7: *Diagram of Experimental Set-up*

tor are all housed on separate pcb's. The output load of the filter circuit must therefore be impedance matched to the input of the second amplifier and the second amplifier output to the discriminator input. If these were all mounted on a single pcb, the gain would be larger by a factor of 4. To simulate this, a fast amplifier module was inserted between the amplifier output and the discriminator. See FIGURE (4.7). The ^{207}Bi pulse height spectrum was this time only recorded in a charge sensitive ADC. This does not provide the same energy resolution as a peak sensing ADC, but this is inconsequential, since the pcb circuitry does not have a spectroscopy amplifier and optimal energy resolution from the individual detecting elements is not required.

4.4.1 Results

FIGURE (4.8) shows a plot of the BaF_2 pulse height against strip detector pulse height. GRAPH (a) highlights the 1063 keV γ ridge in BaF_2, while GRAPH (b) highlights the 570 keV γ ridge in BaF_2. As expected, the strip detector spectrum shows poorer energy resolution than obtained in FIGURE (3.9). It does show the conversion electron peaks of both the 570 keV γ and the 1063 keV γ, but the individual k and l lines are not resolved. As in §3.6, the bulk of the coincidences are seen to be concentrated in the 570 keV γ, 1063 keV conversion electron cascade, where the electron is minimum-ionising in the silicon.

FIGURE (4.9) illustrates the TDC spectrum. As in §3.6, the spectrum is dominated by the 1.063 MeV conversion electron, 570 keV γ coincidences, where the electron is minimum-ionising. The walk contribution to the peak width in this figure, is much reduced in comparison to FIGURE (3.15). This is due to the use of a CFD discriminator, instead of the LED on the strip detector.

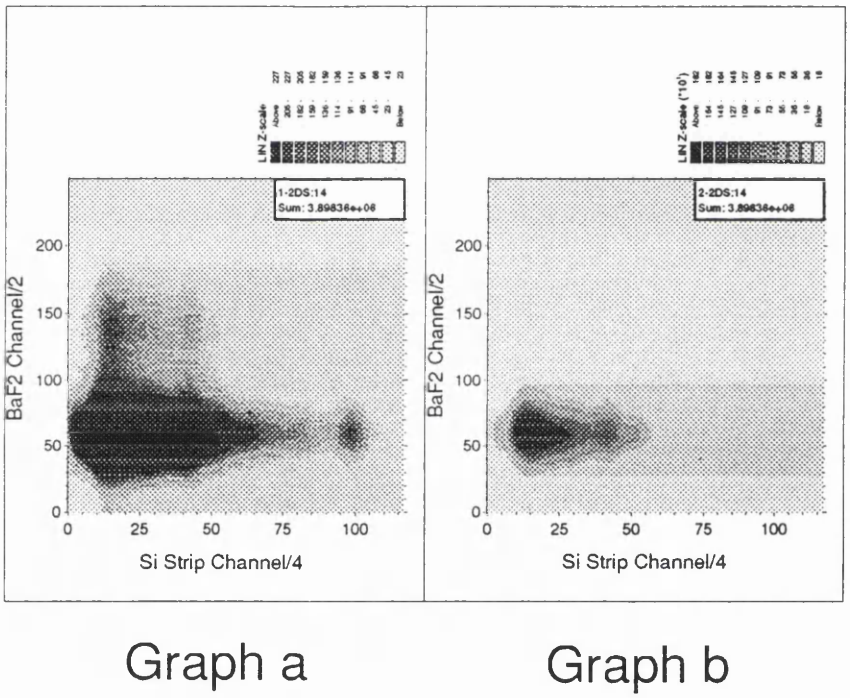

Figure 4.8: *BaF_2 Pulse Height vs Strip Detector Pulse Height*

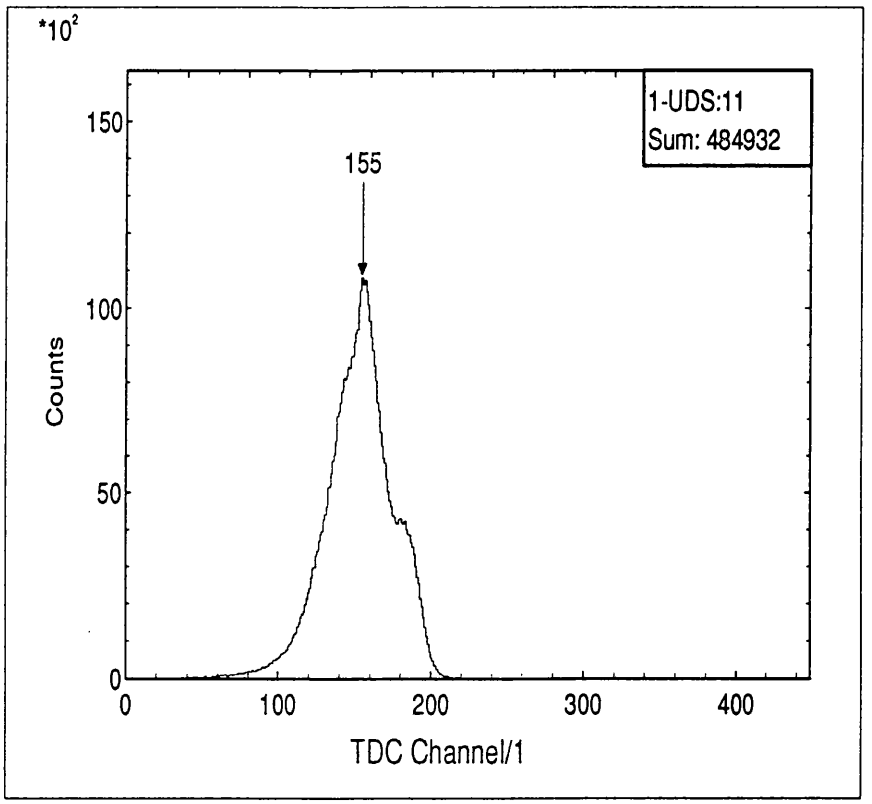

Figure 4.9: *The TDC Spectrum: 1 Channel=0.25 ns.*

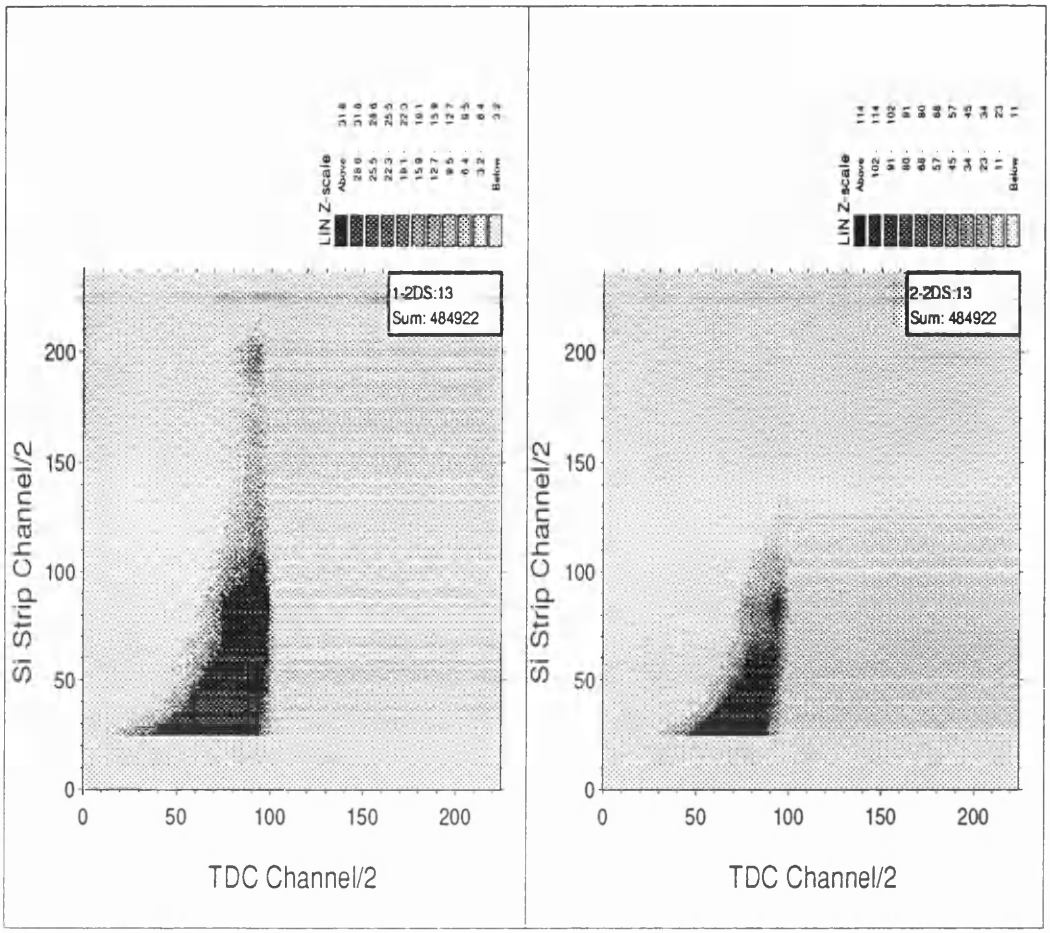

Figure 4.10: *Strip Detector Pulse Height vs BaF_2-Si Time Difference.*

FIGURE (4.10), which shows the strip detector pulse height plotted against the Si-BaF_2 time difference, illustrates the reduced walk. However, the CFD does not eliminate walk completely. This is particularly apparent at lower pulse heights. These effects are best seen by examining the TDC spectrum while cutting at various energies in the strip detector pulse height spectrum.

FIGURE (4.11) therefore shows these cuts. For each graph, TABLE (4.2) lists the cut made in keV and the FWHM of the TDC spectrum. The energy calibration for the cuts was done from the strip detector pulse height spectrum in the same manner as §3.6. The cuts were made narrow enough to make the walk

contribution to the FWHM of the peak negligible, as in §3.6. Conclusions can therefore be drawn about the walk independent timing resolution of the system. In comparison to the results listed in TABLE (3.1) for the walk independent timing resolution of the NIM system, TABLE (4.2) shows that the system timing resolution for the pcb amplifying system is better at lower pulse heights, but unchanged at larger pulse heights. From FIGURE (3.19), the timing resolution varies significantly with the signal:noise ratio, at energies $\leq$ 450 keV in the strip detector. The 20% change in the signal:noise ratio (see §4.3) represents a significant change in timing resolution at these energies. Specifically, from table (4.2), for the energy range of 207 $\rightarrow$ 211 keV, 9 ns timing resolution was attained. The same signal:noise ratio in §3.6 corresponds to an energy of $\sim$250 keV. From FIGURE (3.19), the expected timing resolution is $\sim$ 9ns, in accordance with these results. At larger pulse heights, where the timing resolution changes very slowly with signal:noise ratio, a 20% change does not have a significant effect and would not be seen within the errors of the experiment.

TABLE (4.2) also lists the peak position in ns, relative to the position of the peak recorded for the 207 $\rightarrow$ 211 keV cut. There is a steady rise in the channel in which the TDC spectrum peaks, as the pulse height of the strip detector output rises, with a peak shift of 9.5 ns between the lowest and highest energy cuts. Further as seen in FIGURE (4.10), the bulk of the total peak shift occurs between the lower energy cuts.

This is indicative of a poor walk correction. The CFD timing adjust requires a more refined adjustment than the rough values investigated. However, since thin cuts were made, the walk does not affect the conclusions of the experiment. The trend in the shift of the TDC peak with strip detector energy indicates that

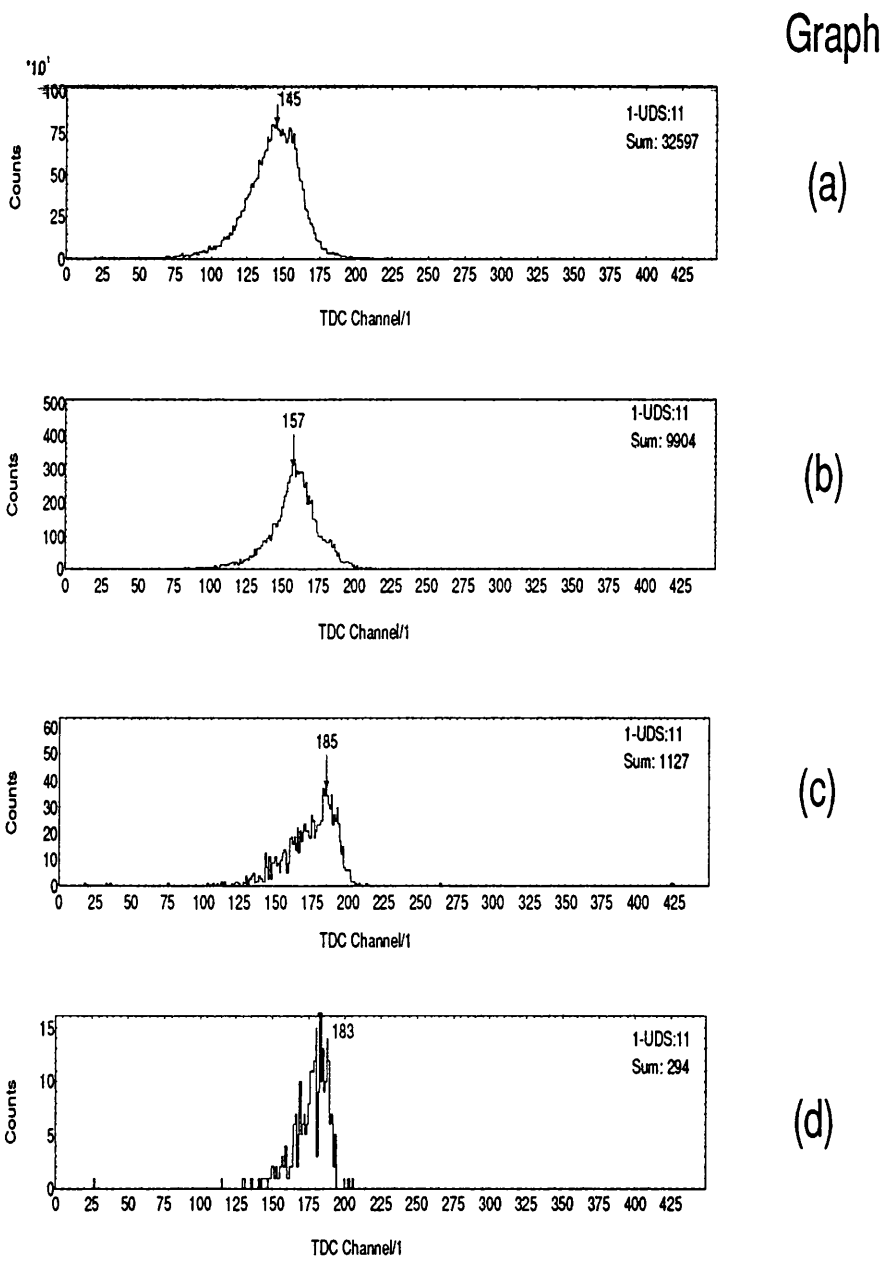

Figure 4.11: *The TDC Spectrum, Cut at Various Points in the Strip Detector Spectrum: 1 Channel=0.25 ns.*

Graph	Range of Cut (keV)	Relative Peak Shift (ns)	FWHM (ns)
a	207 → 211	0.0	9.0
b	290 → 294	3.0	5.5
c	547 → 551	10.0	4.5
d	980 → 984	9.5	3.5

Table 4.2: *Energy Range of Cuts in Strip Detector Spectrum and TDC Peak Position*

the 3.5 mV DC offset of the timing adjust is too high and the amplitude of the fraction pulse is therefore boosted too much at smaller pulse heights, relative to larger pulse heights. This means that the full-sized pulse catches up with the fraction pulse more slowly for smaller pulse heights, than for the larger ones. Thus, smaller pulse heights trigger later. The CFD DC timing adjust should therefore be set a little below 3.5 mV, if a good walk correction is required in the CFD, as will be the case in the tagger focal-plane, if offline walk corrections are to be avoided.

4.5 Conclusions

The TFA and CFD circuits tested in §4.4 were constructed to optimise the timing performance of the strip detector and pre-amp tested in chapter 3. The signal:noise ratio observed in §4.4, in a noise environment identical to that of §3.6 clearly indicates that high density circuitry is successful in improving the signal:noise ratio and consequently, the timing resolution of the strip detector system. As in §3.6, it can therefore be concluded that the strip detector tested can be used with the RAL 108B pre-amp, the TFA circuit of FIGURE (4.2)

and the RAL110 CFD circuit of FIGURE (4.6) to form a focal-plane detecting system capable of higher resolution, but not the required timing. Such a system should therefore be operated in coincidence with the current focal-plane detector array, so that 1 ns timing can be achieved, as explained in §3.8. In a system incorporating the TFA and CFD circuits investigated in§4.4, multichannel pcb's should be built, with 12 or 13 TFA/CFD circuits per board. Each multichannel timing pcb should be no wider than the pre-amp pcb and components should be staggered along the board length to allow this. In this way, all timing electronics can be mounted in one box, if the timing pcb's are mounted one above the other within the box (from §1.2, there is no limitation on the gap 20 cm up/down from the bend plane, so the box can be thicker where the timing electronics are mounted). It is not proposed that the TFA circuit of FIGURE (4.2) be altered outwith the changes suggested in §4.2, if a 1000 μm detector were used instead, to obtain better energy resolution, since in this case, such a detector would be chosen so as to have similar timing properties to the detector tested.

If it is decided that further work should be done to obtain a high resolution detector capable of 1 ns timing, then EQUATIONS (4.7), (4.18) and (4.21) can be applied equally well for other values of the components listed in TABLE (4.1), to predict the effect of integration and differentiation on the gain of a circuit more suited to detectors with faster charge collection. However, for very small signal rise times, the limitations on the gain bandwidth product must be carefully adhered to in the TFA. In a situation where 1 ns timing is required, then every method that can be applied in advance to optimise the signal:noise ratio must be employed. Ideally, the detector and all timing electronics would be mounted on one pcb, but this is not possible unless a way can be found to produce much higher density components for the TFA and discriminator

circuits. One way to do this would perhaps be to use as many surface mounted components as possible. However, surface mount components are more difficult to replace than conventional components and indeed, can only be replaced a few times, so such circuit boards would have to be treated with extreme caution.

To summarise, this thesis demonstrates that a strip detector array is the most suitable choice for a high resolution focal-plane detector. The strip detector, pre-amp and on-board timing electronics investigated can be used to form a high density detector array for better energy resolution in the focal-plane. In this case, the timing prompt must come from the existing focal-plane detectors. The conclusion from the tests undertaken is that it is possible to build a high resolution focal-plane detector array which can also provide a 1 ns timing prompt. However, as indicated in §3.8, 1 ns does represent the best performance which can be expected from a suitable strip detector. This means that further work must be done, as outlined at the end of Chapter 3 and in the above conclusions, to achieve the best timing.

Bibliography

[1] H.HERMINGHAUS *et.al.* : *Nucl.Inst.Meth.* **138** (1976) 1

[2] H.HERMINGHAUS *et.al.* : *Nucl.Inst.Meth.* **187** (1981) 103

[3] I.ANTHONY *et.al.* : *Nucl.Inst.Meth.* **A301** (1991) 230

[4] P.D.HARTY: *Private Communication*, **Glasgow University** (1994)

[5] I.ANTHONY: *TAGQD Internal Report*, **Glasgow University** (1986)

[6] S.KOWALSKI:*RAYTRACE; A Spectrometer Ray Tracing Program.* (**MIT**, Cambridge, USA 1975)

[7] J.D.KELLIE *et.al.* : *Nucl.Inst.Meth.* **A241** (1985) 154

[8] BICRON CORPORATION: *Information Sheet*,**BCF-12**, An Alphen A/D Rijn, Holland (1991)

[9] S.J. HALL *et.al.* : *Tagger Manual Internal Report*, **Glasgow University** (1991)

[10] J.R.M.ANNAND *et.al.* : *ACQU Manual Internal Report*, **Glasgow University** (1993)

[11] MULLARD: *Development Data Sheet* **XP4722**, Mullard (1989)

[12] H. SPIELER: IEEE Trans. Nuc. Sci. **29(3)** (1982) 1142

[13] W.R. LEO: *Techniques for Nuclear and Particle Physics Experiments* **Springer-Verlag**, Berlin-Heidelberg (1987)

[14] S.L. THOMAS *et.al.* : *Nucl.Inst.Meth.* **A228** (1990) 212

[15] S.L. THOMAS: *Private Communication*, **RAL**, Oxon (1993)

[16] W.BRAUNSCHWEIG *et.al.* : *Nucl.Inst.Meth.* **134** (1976) 261

[17] J.C. MCGEORGE: *Internal Report*, **JCM004**, Glasgow University (1994)

[18] M. AGUILAR-BENITEZ *et.al.* : *Phys.Rev. D* **50** (1994) 1173

[19] D.M. RITSON: *Techniques of High Energy Physics* **Interscience Publishers Ltd.**, London (1961)

[20] E.H.M. HEIJNE *et.al.* : *Nucl.Inst.Meth.* **178** (1980) 331

[21] C.D WILBURN *Private Communication*, **MICRON Ltd., Sussex** (1994)

[22] L. EVENSEN *et.al.* : *Nucl.Inst.Meth.* **A326** (1993) 136

[23] F.S. GOULDING *et.al.* : *Nucl.Inst.Meth.* **12** (1961) 249

[24] BURR-BROWN: *Data Sheet* **OPA620KP**, FARNELL Technical Data Service, Leeds (1989)

[25] D.J. WHITE: *The RAL 10 Discriminator*, **RAL-90-088** (1990)